

Effect of Lightning Strikes on Wind Turbine Blade Life

A thesis
submitted by

Christopher Severino

In partial fulfillment of the requirements
for the degree of

Master of Science
in
Mechanical Engineering

TUFTS UNIVERSITY

Date
August 2012

© 2012, Christopher Severino

ADVISER:
Behrouz Abedian

Effect of Lightning Strikes on Wind Turbine Blade Life

Christopher Severino

Abstract

Understanding the effects of lightning strikes on wind turbines becomes increasingly important as the size and rated power of wind turbines increase and as they are placed in locations where repair is difficult and costly, especially for offshore applications. When the lightning strikes, it can locally increase material temperature at the strike zone, inducing high compressive localized strains. The severity of this thermally induced strain depends on the thermal conductivity of strike zone material and the surrounding material. The aim of this paper is to develop a methodology to predict blade residual life after a known number of lightning strikes and to understand the structural integrity threshold due to such damage. Such data will help the wind community to develop sensor specification and predictive methods for blade life after each lightning strike. Thermomechanical stresses and heat transfer cases are used to simulate the lightning strike blade model and it is analyzed through the use of a commercial finite element code. A combined thermal and stress analysis of a lightning strike model of typical wind turbine blade material (including E-glass composite layups) shows that the fiberglass material immediately surrounding the lightning attachment location becomes damaged due to plastic deformation. Depending on the magnitude and number of lightning strikes, the blade has the potential to fail under an extreme static gust load, under fatigue, or a combination of the two. It is therefore crucial to understand the reduced material property limits resulting from lightning strikes. It is hoped that this study will provide a useful guideline for designing lightning protection systems and predicting blade life, especially for offshore wind turbines where lightning strikes are statistically more commonplace.

Acknowledgments

I would like to express my gratitude to my research advisor, Shu Ching Quek, for his constant guidance throughout the entire research process. Without him, my thesis work would not have been possible. His knowledge of the wind turbine industry was incredibly helpful and insightful. I would also like to thank my academic advisor, Professor Behrouz Abedian, for all of his support with my work and for his invaluable expertise. Additionally, I'd like to thank Vincent Manno and Chandra Yerramalli for serving on my advisory committee, as well as for their crucial advice throughout the writing process. I am extremely grateful for the backing and support of General Electric Aviation and Tufts University for making this project possible.

I would also like to thank my colleagues at General Electric Aviation and at Tufts University, whose companionship and mentorship have gotten me to where I am today. I sincerely appreciate my family and friends for their infinite support and encouragement during my time working towards my degree.

Table of Contents

Abstract.....	1
Acknowledgments.....	2
Table of Contents.....	3
Nomenclature.....	5
List of Figures.....	6
List of Tables.....	9
1. Introduction.....	10
1.1. Background.....	10
1.2. Research Goals and Approach.....	12
1.3. Thesis Outline.....	13
2. Overview of Wind Turbine Blades and Lightning Protection Systems.....	14
2.1. Wind Turbines.....	14
2.2. Lightning Damage.....	16
2.3. Lightning Protection Systems.....	19
3. Lightning and Material Property Analysis.....	23
3.1. Lightning Assumptions.....	23
3.2. Lightning Heat Flux.....	25
3.3. Temperature-Dependent Material Properties.....	29
4. Extent of Damage Caused by Lightning Strike.....	40
4.1. Computational Method.....	40
4.2. Thermomechanical Damage Results.....	45
5. How Damage Affects Blade Frequency Responses.....	63
5.1. Blade Condition Monitoring.....	63
5.2. Wind Turbine Blade Design.....	66
5.3. Blade Damage Results.....	79
6. Conclusions and Future Work.....	86
Bibliography.....	90
Appendix A: Heat Transfer Calculations.....	96
A.1. 1-D MathCAD Heat Transfer Calculations.....	96
A.2. Excel Heat Flux Calculations.....	99
A.3. Abaqus-CAE Copper Ablation Input File.....	99
A.4. 1-D MathCAD Heat Transfer Calculations for Ablation Depth.....	102
Appendix B: Material Calculations.....	104
B.1. Excel Material Calculations for Copper.....	104

B.2.	Excel Material Calculations for T300-Epoxy Carbon Composite	104
B.3.	Determination of Stiffness Matrix Terms for T300-Epoxy and E-glass Elastic Material Properties	106
B.4.	DSC Test Results for Temperature-Dependent Thermal Conductivity and Specific Heat Properties of Fiberglass-epoxy Composite.....	110
B.5.	Calculation of Thermal Conductivity of Fiberglass-epoxy Composite in the Fiber-direction	113
B.6.	Volume Fraction Calculations for E-glass Composite Elastic Material Properties	113
B.7.	Directional Material Strength Using Normalized Test Data.....	115
Appendix C: Abaqus Thermomechanical Plate Model		118
C.1.	Thermomechanical Plate Segment – Direct Lightning Strike to E-glass Composite Material.....	118
C.2.	Thermomechanical Plate Segment – Lightning Strike to Copper Lightning Protection Receptor	122
C.3.	Example Material Strength Calculation.....	129
Appendix D: Wind Turbine Blade FEA Design and Modal Analysis.....		131
D.1.	Airfoil Node Calculations	131
D.2.	Abaqus Input Template for Airfoil Nodes	133
D.3.	Abaqus Composite Layup Definitions.....	135
D.4.	Mode Shape Images.....	137
D.5.	Blade Frequency Abaqus Input File Example	141
D.6.	Blade Frequency Excel Results	144

Nomenclature

Symbol	Definition	Unit
A	Area	m ²
c _p	Specific Heat Capacity	J/kg-K
E	Young's Modulus	Pa
G	Shear Modulus	Pa
h	Heat Transfer Coefficient	W/m ² -K
I	Current	Amps
k	Thermal Conductivity	W/m-K
L	Length	m
q	Heat Power	W
q"	Heat Flux	W/m ²
R	Resistance	Ω
r	Radius	m
T	Temperature	K
t	Time	s
V	Volume Fraction	--
α	Coefficient of Thermal Expansion	m ² /s
α _T	Thermal Diffusivity	K ⁻¹
ε	Strain	m/m
ν	Poisson's Ratio	--
ρ	Density	kg/m ³
σ	Stress	Pa
τ	Time Value	s

List of Figures

Figure 1-1: U.S. Annual and Cumulative Wind Power Capacity [1]	10
Figure 1-2: Lightning Strike vs. Tower Height [5].....	11
Figure 2-1: Size and rated power development of commercial wind turbines [8].....	14
Figure 2-2: Three bladed horizontal axis wind turbine.....	15
Figure 2-3: General wind turbine nacelle design	15
Figure 2-4: Example blade cross-section (single shear web).....	16
Figure 2-5: Percent of lightning faults in lightning seven year lightning strike study [15].....	18
Figure 2-6: Lightning puncture local to the tip of a wind turbine blade [2]	19
Figure 2-7: Lightning protection concepts for large modern composite material wind turbine blades [17].....	20
Figure 2-8: External lightning protection system with simulated lightning stroke [2].....	21
Figure 2-9: Application of the rolling sphere method to wind turbine [17]	22
Figure 3-1: Shape of stroke current over time [19].....	24
Figure 3-2: Temperature contour plot for a copper puck with a length of 1 mm	27
Figure 3-3: Temperature as a function of depth for copper	27
Figure 3-4: Temperature as a function of depth for E-glass composite.....	28
Figure 3-5: Specific heat of fiberglass-epoxy composite obtained from DSC experiments and transcribed to Excel [35].....	35
Figure 3-6: Thermal conductivity of fiberglass-epoxy composite material in the transverse-direction obtained from DSC experiments and transcribed to Excel [35].....	35
Figure 3-7: Normalized Fiberglass Composite Yield Strength from Material Test Data [39]	39
Figure 3-8: Directional E-glass Composite Yield Strength as a Function of Temperature	39
Figure 4-1: Directionality of copper receptor and biaxial E-glass sheets for first two composite layers of the model.....	41
Figure 4-2: Material assignment for full plate model without a copper receptor	42
Figure 4-3: Boundary conditions and heat flux load for plate model	43
Figure 4-4: Data points analyzed in fiber-direction and transverse-direction (naming convention based on surface composite ply).....	45
Figure 4-5: Thermal contour plot of direct lightning strike to composite material	46
Figure 4-6: Contour plot of strike to copper lightning receptor	47
Figure 4-7: S11 contour plot for direct lightning strike to composite material, 5 s after lightning strike.....	48

Figure 4-8: S22 contour plot for direct lightning strike to composite material, 5 s after lightning strike.....	48
Figure 4-9: Thermal gradient as a function of radius from the plate center in the fiber-direction.....	49
Figure 4-10: Thermal gradient as a function of radius from the plate center in the transverse-direction	50
Figure 4-11: Fiber-direction surface temperature, stress, and material strength at 0.269 s after lightning strike	50
Figure 4-12: Transverse-direction surface temperature, stress, and material strength at 0.269 s after lightning strike.....	51
Figure 4-13: Temperature, stress, and composite strength distributions at different depths within the plate at 0.269 s after the strike in the fiber-direction	52
Figure 4-14: Temperature, stress, and composite strength distributions at different depths at 0.269 s after the strike in the transverse-direction	53
Figure 4-15: Temperature, stress, and yield strength in the fiber-direction 5 s after lightning strike.....	54
Figure 4-16: Temperature, stress, and yield strength in the transverse-direction 5 s after lightning strike.....	55
Figure 4-17: Temperature distribution at the plate surface for multiple time steps in the fiber-direction for a lightning strike to a copper receptor.....	56
Figure 4-18: Temperature distribution at the plate surface for multiple time steps in the transverse-direction for a lightning strike to a copper receptor	56
Figure 4-19: Fiber-direction temperature, stress, and strength gradients at 0.005 s after lightning strike.....	57
Figure 4-20: Transverse-direction temperature, stress, and strength gradients at 0.005 s after lightning strike	57
Figure 4-21: Fiber-direction temperature, stress, and strength plots at various depths within the plate.....	58
Figure 4-22: Transverse-direction temperature, stress, and strength plots at various depths within the plate.....	59
Figure 4-23: Fiber-direction temperature, stress, and strength 0.027 s after strike	60
Figure 4-24: Transverse-direction temperature, stress, and strength 0.027 s after strike	61
Figure 5-1: Sketch of a wind turbine blade segment illustrating some of the common damage types [42]	65
Figure 5-2: Damage type 2 (adhesive joint failure between skins) at the leading edge [42].....	65
Figure 5-3: Damage type 1 (main spar flange/adhesive layer debonding) and type 4 (delamination by buckling load) [42]	65
Figure 5-4: NACA 64(3)-618 Standard Airfoil, viewed from blade root in Abaqus-CAE	67

Figure 5-5: Uploaded airfoil nodes at a blade radius of 4.75 m	69
Figure 5-6: Wire outline of the blade airfoil at the 4.75 m plane	69
Figure 5-7: Lofted turbine blade	70
Figure 5-8: Lofted turbine blade viewed from the blade root.....	71
Figure 5-9: Blade breakdown between tapered and constant segments	72
Figure 5-10: Material orientation definition for blade shell	73
Figure 5-11: Boundary condition prevents rotation and displacement at the root.....	74
Figure 5-12: Crack propagation along the trailing edge at the blade tip	77
Figure 5-13: Crack propagation along the trailing edge at the middle of the blade	78
Figure 5-14: Crack propagation along the trailing edge at the widest chord near the root of the blade.....	78
Figure 5-15: Crack propagation across the shear web near the tip of the blade	79
Figure 5-16: Natural frequency difference for first 10 modes at trailing edge of blade tip.....	80
Figure 5-17: Natural frequency difference for first 10 modes at trailing edge of blade mid-length	81
Figure 5-18: Natural frequency difference for first 10 modes at trailing edge of blade at the widest chord.....	82
Figure 5-19: Natural frequency difference for first 10 modes at shear web/spar cap interface near blade tip.....	83
Figure 5-20: Natural frequency difference for first 10 modes at shear web/spar cap interface near blade mid-length	83
Figure 5-21: Natural frequency differences for first 10 modes at shear web/spar cap interface at largest chord.....	84
Figure 6-1: Stitching pattern a blade material pattern, generated in a laboratory [2].....	88

List of Tables

Table 1-1: Protection levels and maximum values of lightning parameters [7]	12
Table 3-1: Typical Stockpile-to-Target Sequence Requirements and Known Lightning Parameters [20]	24
Table 3-2: Copper Material Properties [24], [26]	31
Table 3-3: Rigid PVC Foam Material Properties for Turbine Blade Core [24], [27], [28]	32
Table 3-4: Density, Specific Heat, and Thermal Conductivity of Carbon Composite [21], [30], [31]	33
Table 3-5: Elastic and Thermal Expansion Properties Based on Temperature-Dependent Material Test Data [32]	33
Table 3-6: Stiffness Matrix Terms for T300-Epoxy Elastic Property Inputs into Abaqus	34
Table 3-7: Density and Coefficient of Thermal Expansion of Fiberglass-Epoxy Composite [34]	34
Table 3-8: Fiber and Matrix Elastic Properties Used to Calculate E-glass Composite Elastic Properties [37], [38]	37
Table 3-9: Calculated Elastic Properties for E-glass Composite	37
Table 3-10: Stiffness Matrix Terms for E-glass Composite Elastic Property Inputs into Abaqus	38
Table 3-11: E-glass Composite Directional Material Strengths at Room Temperature [34]	38
Table 5-1: Typical damage of wind turbine blades [42]	64
Table 5-2: Blade Geometry [43]	68
Table 5-3: Natural Frequencies for First Ten Modes of Baseline Turbine Blade	75
Table 5-4: Variation in Crack Length Assigned to Blade	76

1.Introduction

1.1. Background

Installed wind energy capacity has grown rapidly both domestically and worldwide in recent years. Figure 1-1 shows that the cumulative installed wind capacity in the U.S. grew between 2010 and 2011, totaling 47 GW at the end of the fourth quarter of 2011. The dark blue in the graph represents the cumulative installed wind capacity in GW, the light blue data is the total installed wind capacity for a specific year, and the remaining orange, green, yellow, and royal blue data represent installed wind capacity for the first, second, third, and fourth quarters for a specific year, respectively.

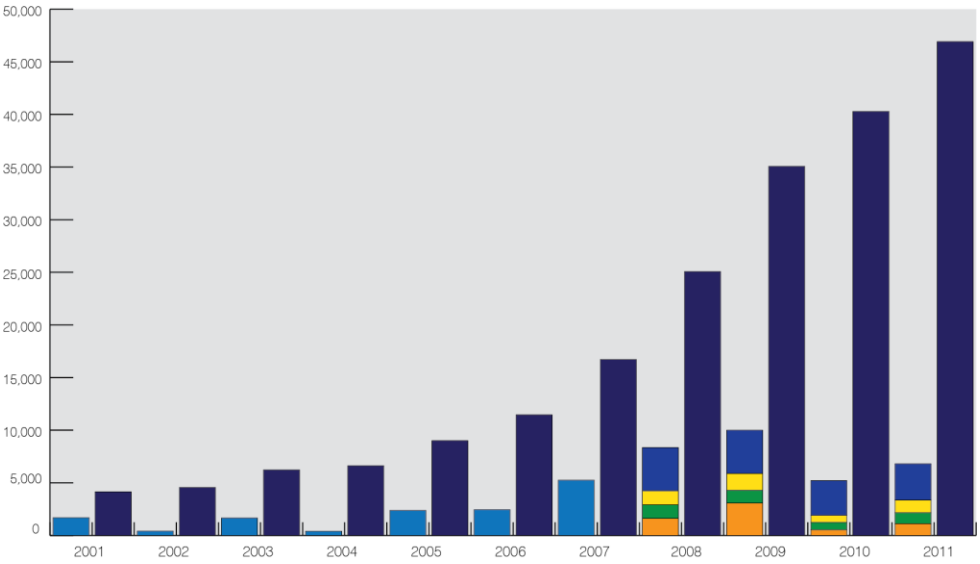


Figure 1-1: U.S. Annual and Cumulative Wind Power Capacity [1]

The U.S. wind industry installed 6.8 GW in 2011, a 31% increase from total 2010 installations [1]. As technology and manufacturing capabilities improve, wind turbines become larger and provide more power.

Understanding the effects of lightning strikes on wind turbines becomes increasingly important as the size and rated power of wind turbines increase and as they are placed in remote locations, such as offshore sites, where repairs are difficult and costly. Up to 1994, there have been several studies suggesting that there are no records of lightning striking wind turbines.

Since then, however, lightning strikes have been thoroughly documented and lightning is currently one of the main sources of wind turbine insurance claims [2]. Statistics available in 2008 show that between 4% and 8% of the European wind turbines are damaged by lightning every year [3], and a 1995 German study estimated that 80% of insurance claims paid for damage compensation were caused by lightning strikes [4]. As taller wind turbines become more prevalent, the statistical likelihood of lightning strike increases, as shown in Figure 1-2.

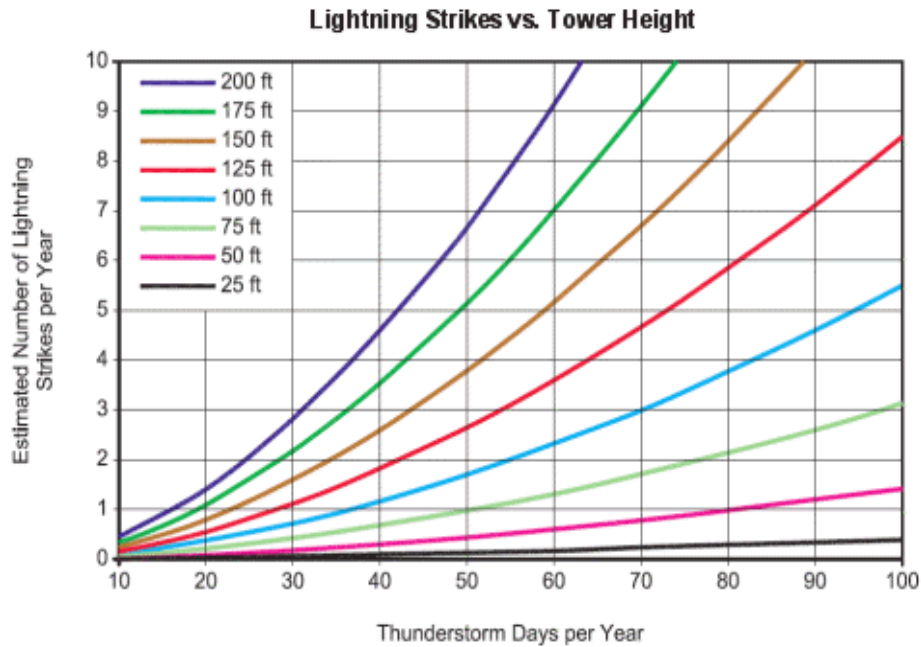


Figure 1-2: Lightning Strike vs. Tower Height [5]

Wind turbine blades are now being produced with lengths of over 50 meters and longer and include conductive materials, requiring the presence of some form of blade lightning protection system. Current blade lightning protection systems vary in type, but typically include a conductive puck near the blade tip attached to a conductive wire within the blade back to the hub. With or without protection, lightning can lead to air temperature increases approaching 30,000 K and can result in an explosive development of air within the blade [6]. The thermal effects due to lightning strikes have not been extensively researched in the past. There is concern that the high thermal gradient in the blade material can result in negative performance effects, including high thermal stresses, which can ultimately lead to blade failure.

1.2. Research Goals and Approach

The goal of this research is to identify the extent of thermal gradients in wind turbine blade material resulting from lightning strikes and to determine the corresponding effects on blade material performance, including thermal stresses and temperature-dependent material properties. The intent of thermomechanical modeling and testing is to identify the amount of irreversible plastic strain per lightning strike in order to determine the number of lightning strikes required to reach the blade's fatigue life and structural integrity threshold.

The one of the aims of the research is to study the effects of thermal gradients due to lightning strike impulse load. The exact heat flux due to lightning strike varies widely and is not definitively known, but minimum lightning protection requirements provide a starting point for heat transfer modeling. The fact that both direct and indirect lightning strikes are possible is accounted for in the thermal model simulation. Determining appropriate heat fluxes, pulse durations, and how to correctly model both direct and indirect lightning strikes is accomplished by exploring the physics of lightning strikes. A heat flux impulse load is introduced to the system and analyzed for different protection levels provided by Krämer et al., shown in Table 1-1.

Table 1-1: Protection levels and maximum values of lightning parameters [7]

Protection level	Peak current [kA]	Specific energy [kJ/ Ω]	Average rate of current rise [kA/ μ s]	Total charge transfer [C]
I	200	10000	200	300
II	150	5600	150	225
III	100	2500	100	150
IV				

A typical type of blade material is used in order to focus on the phenomenon of the material. Later studies can be performed to extrapolate the effects to additional blade materials, but for the sake of this study, two specific materials (E-glass composite and T300 Carbon composite facesheets sandwiching PVC foam, typical blade skin constructs explained in detail in later chapters) are selected for model simulation, as they are common to the wind community.

A finite element model of typical wind turbine blade material is designed for thermal stress analysis. The design of the model replicates the thermal effects of direct and indirect lightning impulses. In conjunction with thermal stresses, a full blade model is used to determine the extent of potential damage due to internal pressure build-up and damage detection limits.

1.3. Thesis Outline

This thesis consists of six chapters. Background, motivation, and objectives of the research effort highlighted in Chapter 1. Chapter 2 provides an overview of wind power generation, wind turbine blade design, potential damage caused by lightning strikes, and lightning protection systems currently in place. Lightning flux analyses and assumptions are covered in Chapter 3, along with temperature-dependent material properties and the associated finite element model inputs. These are grouped together because they both present the information necessary for heat transfer analysis. Chapter 4 encompasses the heat transfer analysis for a small segment of turbine blade material for both direct lightning strikes to the material as well as strikes involving a lightning protection system. A model of an entire turbine blade is presented in Chapter 5 to determine how potential damage affects blade frequency response. Finally, Chapter 6 provides conclusions and a summary of the research effort as well as recommendations for future research opportunities.

2. Overview of Wind Turbine Blades and Lightning Protection Systems

2.1. Wind Turbines

Windmills have been used for pumping water and grinding grain for centuries, and more recently, wind turbines have been used for generating electricity since the early days of electrical power. Competition with cheaper and easier alternatives, such as fossil fuel-based electrical generation, led to near abandonment after World War II; however, the oil crises in the 1970s prompted many nations to invest in alternative energy options. Since then, the size and power rating for commercial wind turbines has increased 100-fold in power, as shown in Figure 2-1.

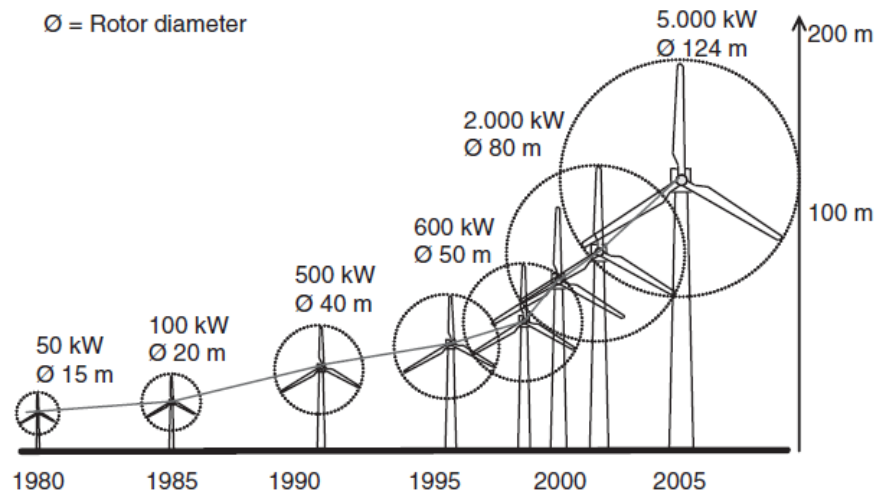


Figure 2-1: Size and rated power development of commercial wind turbines [8]

A majority of wind turbines have been installed on land, but large offshore wind projects have been installed in recent years and many are currently in development.

There are many variations amongst wind turbine designs, including the number of blades, presence of a gearbox, and even orientation of the nacelle (horizontal versus vertical axis). Figure 2-2 and Figure 2-3 show some of the common components of a traditional 3-blade horizontal axis wind turbine.

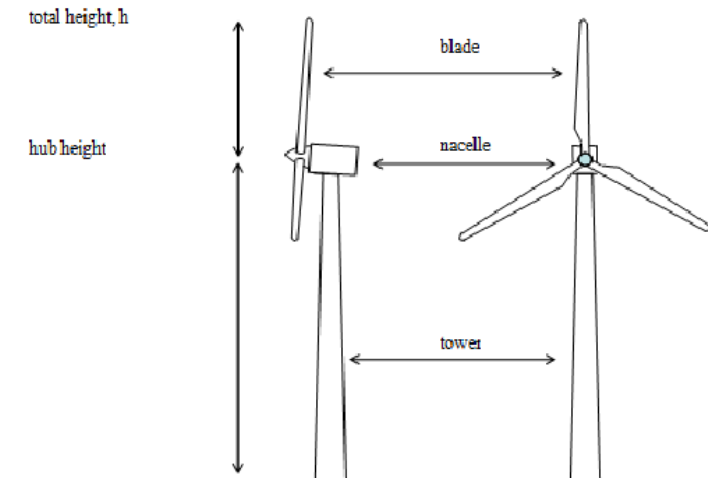


Figure 2-2: Three bladed horizontal axis wind turbine

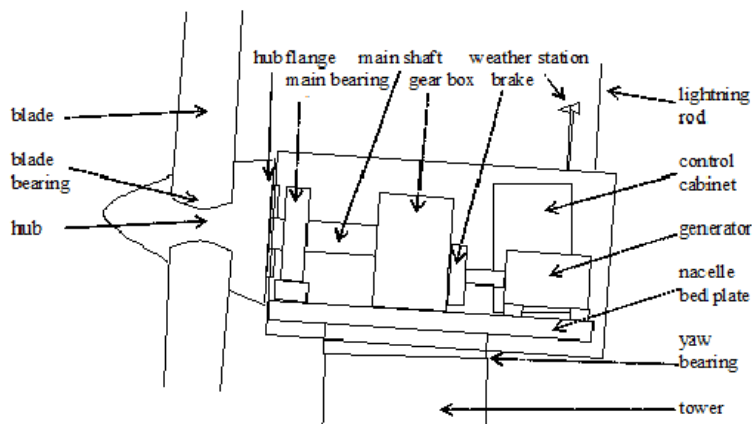


Figure 2-3: General wind turbine nacelle design

Since the goal of this thesis is for the results to be representative of a common, highly prevalent type of turbine, most of the analysis is conducted for a three bladed horizontal axis turbine rated at 1.5 MW, which is a common type of wind turbine blade in operation today.

Almost all turbine blades exhibit an airfoil shape in order to optimize performance. Figure 2-4 is an example of a blade design with a single shear web, reinforced with spar caps.

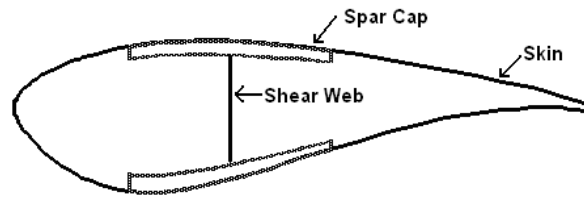


Figure 2-4: Example blade cross-section (single shear web)

Another common type of blade design includes two rigid shear webs at either end of the spar caps. The blade design used for analysis in this thesis is similar to that of Figure 2-4, in which a single shear web, located at the shear center of the airfoil, runs from the high-pressure side to the low-pressure side of the airfoil and attaches to the reinforced spar caps.

There are a multitude of material options for different blade components. Blade skins are comprised of multiaxial fiber-reinforced composite materials, typically sandwiching either a wood or foam core. The construction of typical 1.5 MW turbine blades includes fiberglass epoxy resin with an interior spar-reinforced shear web. Further interior strength is attained with sandwich fiberglass sheets encasing a material with strong tensile properties. The tensile properties of carbon fibers make it an ideal material for parts of the blade that undergo high tensile stresses, such as the spar caps [9].

Material properties for this thesis are chosen to represent typical wind turbine blades currently in production. Biaxial E-glass sheets are a common skin option, chosen for cost effectiveness. A 5-ply ($\pm 45,0$) layup is selected for analysis for the blade skin material. This skin layup sandwiches rigid polyvinyl chloride (PVC) foam for extra structural support. The shear web is made of the same combination of materials, with several sets of biaxial E-glass sheets encasing the foam core for rigidity. T300 carbon composite material properties are selected for the spar caps.

2.2. Lightning Damage

In order to maximize profits, wind turbines are placed at sites with high wind capacity, which tend to coincide with considerable lightning occurrence. Maps prepared by NASA have shown that in most areas of high wind density, there are 30 or more thunderstorm days per year

[10]. With increasing wind turbine size and complexity, a single lightning strike can result in significant physical damage and even catastrophic failure, causing substantial loss of revenue through down-time. Lightning damage can be attributed to inadequate direct-strike protection, incorrect or insufficient bonding, or over-current and over-voltage transients induced by direct and indirect lightning strikes [11]. There are a number of risks associated with lightning strikes: punctures due to plasma heat at the lightning strike point, failure of internal electrical systems, mechanical damage (both internal and external), damage triggered by melted conductors, and explosive expansion of air within the blade.

Height, shape, and isolation are all leading factors in determining lightning strike location. Wind turbines sustain a high probability of being struck by lightning compared to nearby structures given their height, exposed position, and the fact that they are placed in windy and sometimes tempestuous weather [6]. Turbines with internal-type lightning protection systems can be expected to suffer several lightning strikes over the course of its lifetime, sometimes one per year or more, depending on yearly lightning activity data in that location [2]. A 2002 study conducted by the National Renewable Energy Association showed that up to eight out of 100 wind turbines could be expected to receive one direct lightning strike every year [10]. The blades of the wind turbine are a likely location of direct lightning attachment, as they are the highest point of the wind turbine and most exposed. Turbine blades are the focus of this thesis for that reason.

The financial implications resulting from service down-time (while repairing or replacing a component that has failed during service), coupled with the costs of maintenance and materials prove to be substantial over the 20-year life of an average wind turbine. The average frequency of wind turbine outages in Europe due to lightning damage was between 4-8% per year between 1991 and 1998; in Japan it was between 10-12% per year between 2002 and 2006 [12]. A case study in south central Texas found that 5% of wind turbine blades had experienced blade lightning damage over a three-year period [13]. Increasing turbine reliability and decreasing service down-time are the biggest motivations for new technology and research in today's wind energy community. Due to the remote location and extreme operating environment, offshore maintenance costs are even higher than those for land-based installations. Repairs require specialized access and servicing equipment, adding to the already high maintenance cost. For large offshore wind turbines in the Sea of Japan, blade damages account for 75% of the total

repair costs [12]. The magnitude of these repair costs is enough financial incentive to strive toward reliability improvements. For example, among the top ten contributors of non-availability (a combination of frequency of occurrence and down-time), rotor blade repair is ranked number four [14]. Figure 2-5 shows the results of a seven year study of 739 wind turbines, determining that of 1032 total lightning faults, 205 were found in the rotor blades.

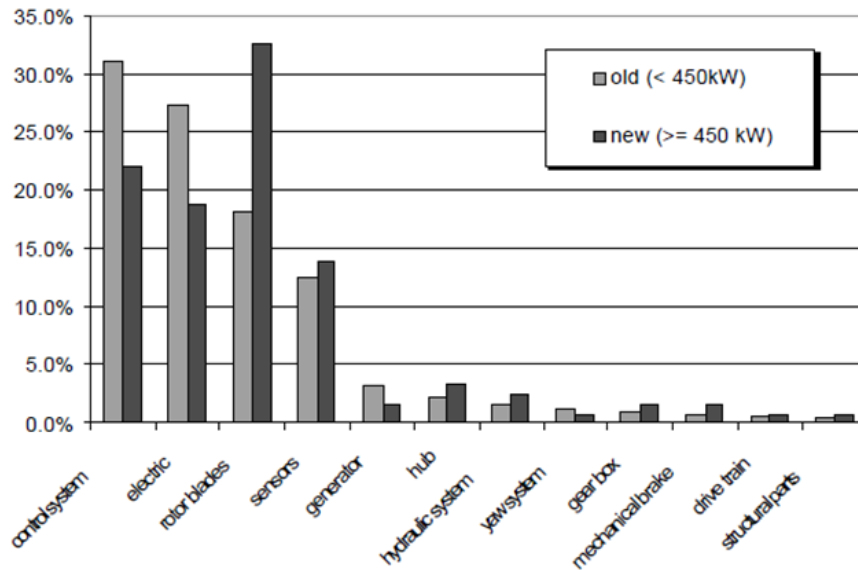


Figure 2-5: Percent of lightning faults in lightning seven year lightning strike study [15]

For all turbines in the study, rotor blades come third for most number of lightning faults compared to all other components. However, when only looking at the newer turbines rated greater than 450 kW, they are the most numerous, accounting for 32.5% of the lightning faults.

Damage due to lightning strikes to wind turbine blades can manifest itself in many ways. Shockwaves due to the rapid expansion of air during a strike can produce damage through excessive hydrodynamic pressure, but the type of damage explored in this thesis is the damage caused due to heat transfer within the blade material during lightning strike, resulting in thermal stresses and potential blade damage due to plastic deformation of the blade material. The immediate temperature increase at the point of lightning attachment is sufficiently high that some surface material can be ablated away. Thermal gradients and resulting thermal stresses brought on by lightning strike are investigated in Chapter 4.

In some instances, a direct lightning strike can completely puncture through the blade material. Punctures, or stitching, are attributed to localized material damage due to extremely

high temperatures, resulting in resin decomposition, delamination, and even carbon sublimation or glass fiber ablation, discussed in Chapter 3. Figure 2-6 shows an example of a puncture through the blade skin localized at the blade tip.

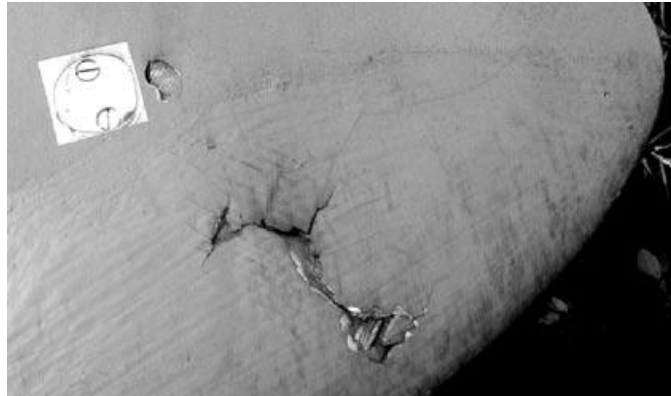


Figure 2-6: Lightning puncture local to the tip of a wind turbine blade [2]

This can result in a high-pressure shock wave inside the blade, creating a large internal force. Damage can range from splitting at lamination locations to complete destruction of the blade [2]. Two specific areas of interest include the splits in the trailing edges as well as between the spar cap and shear web. These are generally the weakest parts of the blade construction due to the fact that lamination material makes up a large portion of the connection. Damage at these regions will be explored in Chapter 5.

2.3. Lightning Protection Systems

Lightning protection was not a major concern prior to the 1980s. Most wind farms were located in California and northern Europe, where lightning occurrence was scarce [8]. Wind turbines were relatively low in height, therefore protecting them from lightning strikes was not deemed as important compared to more immediate problems such as preventing breakdowns brought on by high winds [8]. It was originally thought that lightning protection systems actually did more harm than good considering turbine blades were often made of non-conductive materials and would therefore not require protection. Experience has since shown that blades not fitted with lightning protection can be destroyed, and it is now rare to find a modern wind turbine without some type of blade lightning protection system. It was thought that lightning protection systems would attract lightning attachments, whereas non-conductive material blades would

remain safe. Contrary to this, experiments have shown that the turbine blade is a preferential path for lightning current compared to air [2]. As wind turbines grew larger in size and moved offshore, lightning damage grew more prevalent. In the mid-1990s, lightning damage to wind turbine blades had reached unacceptable levels, and the resulting pressure from insurance companies forced the wind turbine industry to develop lightning protection systems for blades [16].

The main functions of lightning protection systems in a wind turbine are to successfully attach the lightning channel to a preferred attachment location, facilitate the electric current passage through the turbine without damaging any turbine component, and to minimize the voltage levels in and around the turbine. Two basic types of protection systems are widely used in most existing wind turbine blades. The first type includes an external lightning receptor in the form of a metal disc, flush with the surface of the blade near the tip. This receptor penetrates to the internal surface of the blade where an internal conductor runs down the blade, through the root, and is grounded via a low-speed shaft. An example of this type of design is shown in concepts A and B in Figure 2-7.

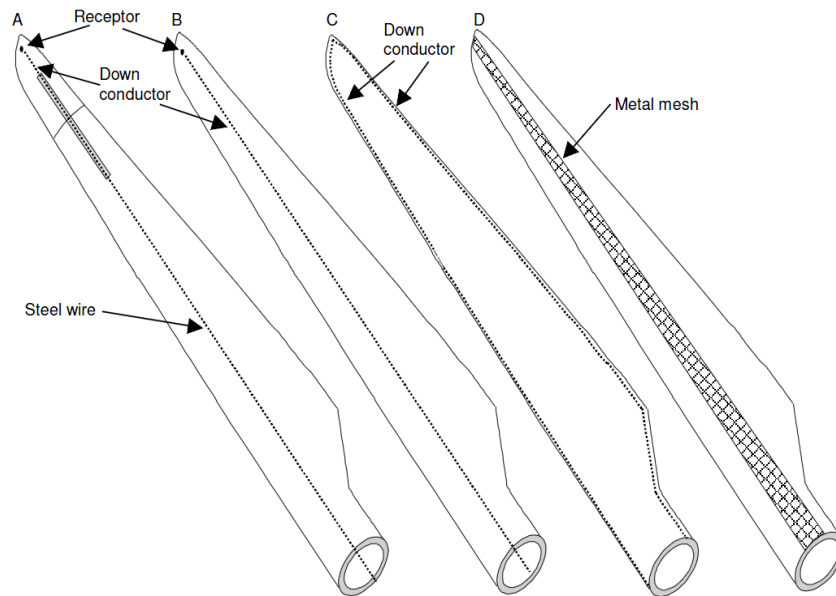


Figure 2-7: Lightning protection concepts for large modern composite material wind turbine blades [17]

The second type of system involves a conductor running the full length of the blade either on or in close proximity to the blade surface. Two examples are shown in illustrations C and D in

Figure 2-7. Figure 2-8 is an example of this type of system in which the conductor is allowing a stroke current to pass to the blade root.



Figure 2-8: External lightning protection system with simulated lightning stroke [2]

However, many manufacturers opt against this second type of protection system because it is more difficult to manufacture [2]. In order to simulate a common type of lightning protection system for analysis, an external lightning receptor with a copper cylindrical puck 2 cm in diameter is used (see Chapter 4).

The standard for protecting wind turbines against lightning damage is IEC 61400-24; it addresses most major issues related to lightning protection for wind turbines [10]. However, no lightning protection system is completely effective. A system in compliance with protection standards reduces the statistical risk to an acceptable threshold, but it does not guarantee immunity from lightning damage [11]. Even with a protection system in place, direct lightning strikes are possible. The disadvantage of having a lightning protection system with an external receptor is that the receptor area is relatively small and therefore the system interception efficiency, or the efficiency of the system in attracting lightning strokes to the required attachment point, can be significantly less than 100% [2]. Longer turbine blades in the field equipped with this type of system still suffer lightning damage due to direct strikes.

The rolling sphere method, shown in Figure 2-9, is used in IEC 61400-24 in an attempt to produce a more accurate determination of lightning attachment locations.

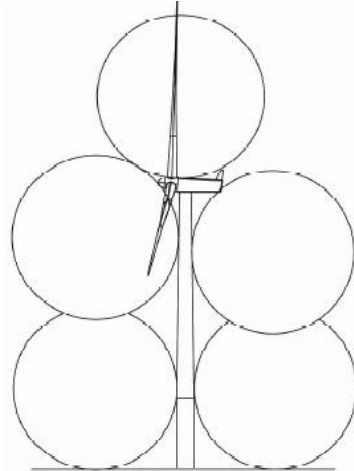


Figure 2-9: Application of the rolling sphere method to wind turbine [17]

Lightning protection zoning is a convenient way to evaluate the parts of a wind turbine that may be influenced by lightning in order to ensure that all parts have adequate protection. Lightning protection zones are established by rolling an imaginary sphere along the outside of a structure, and any point of the structure that the sphere can touch is assumed to be vulnerable to direct lightning strike. The rolling sphere model suggests that lightning attaches to tall structures below the highest point [17]. Therefore, lightning does not necessarily always attach at lightning receptors positioned at the blade tip, and long turbine blades are vulnerable elsewhere along the blade. For these reasons, both indirect (protected) and direct lightning strikes are modeled.

3. Lightning and Material Property Analysis

3.1. Lightning Assumptions

The physics of a lightning discharge are an extremely complex phenomenon and is in no way consistent for all lightning strikes. Lightning discharges can transfer either positive or negative charge to the ground, but approximately 90% of all lightning strokes are negative. The most common type of lightning is cloud-to-ground lightning, in which currents as great as 300,000 A have been recorded [10]. As downward propagating discharges, or leaders, approach the ground, the electric field increases at grounded objects because of the charge in the downward leader. An upward stroke from the grounded object begins to make the final connection once the electric field exceeds a certain level. At this phase, return stroke current flows through the struck object, which is known as the return stroke phase. Some channels include multiple strokes occurring within several microseconds of each other in the same lightning channel. Due to the complex nature and unpredictability of lightning strikes, several assumptions must be made in order to continue with heat transfer analysis.

The most frequent expression used for channel-based lightning current over time is

$$i(t) = (I_0/\eta)[e^{(-t/\tau_1)} - e^{(-t/\tau_2)}] \quad 3-1$$

where I_0 is the maximum value of the current, η is a correction factor of the current peak, and τ_1 and τ_2 are time constants determining current rise and decay time and maximum current steepness [18]. Figure 3-1 shows a typical shape of lightning stroke current as a function of time, where T_1 is the current rise time and T_2 is the decay time.

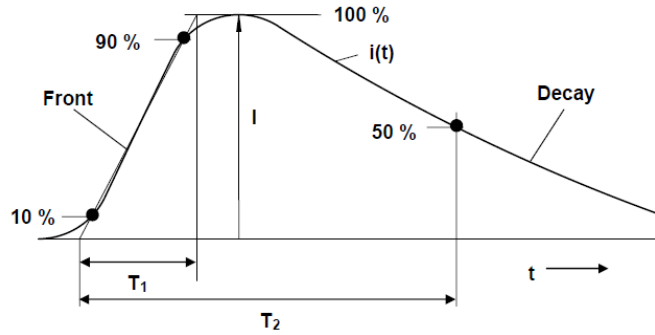


Figure 3-1: Shape of stroke current over time [19]

Rakov and Uman provide basic parameters to describe the shape of the current function, as shown in Table 3-1.

Table 3-1: Typical Stockpile-to-Target Sequence Requirements and Known Lightning Parameters [20]

Lightning parameters	STS requirements		Known parameters	
	Most severe	50% level	2% level	50% level
Peak current ¹	200 kA	20 kA	140 kA	20 kA
Time to peak current	0.2 μ s	2.0 μ s	12 μ s	1.8 μ s
Current rate of rise	100 kA/ μ s	20 kA/ μ s	100 kA/ μ s	22 kA/ μ s
Pulse width (full width half maximum)	200 μ s	50 μ s	170 μ s	45 μ s
Continuing current amplitude	700 A	140 A	520 A	140 A
Continuing current duration	500 ms	160 ms	400 ms	160 ms
Number of strokes	1 - 12	2	10 - 11	2 - 3

In order to simplify this function for calculation purposes, the lightning is taken as a step function with a constant heat flux lasting 200 microseconds (the time at which the current drops to roughly half of the peak value [20]). This is deemed acceptable as the time delta of the lightning pulse is relatively short and that the total energy transfer is roughly equivalent.

Downward-propagating lightning leaders do not travel completely vertical from the sky to the ground, but traverse in various directions. Combining this with the fact that the interception efficiency of the lightning receptor on the blade is not 100%, it becomes evident that the lightning attachment location is difficult to assess and assumptions are necessary to carry on

with analysis. For strikes attaching to the external copper receptor of the protection system, it is assumed that the lightning leader attachment is entirely contained within the surface area of the copper puck. For direct lightning strikes to the blade material, it is assumed that the attachment point is sufficiently far from any lightning receptor. Lightning bolt radii range in size, but it is assumed that the entire bolt is contained within the radius of a copper lightning receptor (or an equivalent radius if directly striking composite blade material). Despite the fact that luminosity, and therefore temperature, varies within the radius of the lightning bolt, it is assumed that the lightning temperature is kept at a constant value across the strike area.

It is important to note a few basic assumptions inherently made when simulating a lightning strike within a finite element model. Peak temperatures of radiating plasma in the lightning channel were measured at 30,000 Kelvin. However, these values were obtained assuming the radiating gas was optically thin and in local thermodynamic equilibrium, which may be invalid for some spectral lines [20]. For the sake of heat transfer analysis, it is assumed that this peak value is accurate. It is possible for the extremely powerful electric fields to alter material properties of the blade surface. This complex phenomenon requires future research to understand the exact effects of the electric field on the blade material. This effect is neglected for present research, but should be considered when the material effects are understood.

3.2. Lightning Heat Flux

The lightning strike is modeled as a surface heat flux rather than an electrical current to simplify calculations. Initially, simplified one-dimensional heat transfer calculations were carried out using an analytical approach. Radiated heat flux is a function of source temperature and destination temperature, as shown in the expression:

$$q'' = \sigma \cdot (T^4 - T_s^4) \tag{3-2}$$

where q'' is the heat flux due to radiation, σ is the Stefan-Boltzmann constant, T^4 is the source temperature (in this case, 30,000 K), and T_s^4 is the surface temperature of the lightning strike zone of the turbine blade. Appendix A.1 shows that the electron cloud next to the wind turbine blade induces a radiation flux equal to $4.6 \times 10^{10} \text{ W/m}^2$. As the strike zone surface temperature increases over time, the radiation heat flux decreases as shown in Appendix A.2. However, the

reasonable range of potential material temperatures remains within a region of relatively constant heat flux. Therefore, it is assumed that the heat flux value remains constant for the duration of the lightning pulse.

The heat flux from the 30,000 K air surrounding the lightning plasma is so high that a portion of the copper lightning protection receptor is ablated away. The copper surface temperature is therefore limited to the vaporization temperature of the material, assuming that any material exceeding this temperature would be ablated away. Similarly, modeling a direct lightning strike to the composite blade material assumes a certain amount of energy goes into damaging the material. The physical process of damaging carbon composite material via Joule heating is not entirely understood, but a combination of phenomena is expected: matrix resin decomposition resulting in delamination and carbon fiber melting [21]. Using a carbon sublimation model, Ogasawara et al. estimate the carbon mass loss rate due to sublimation as a function of temperature [21]. For that study, the maximum composite temperature is limited to 3273 K. Above this temperature, the sublimation rate of carbon increases significantly: carbon fibers break, resulting in no Joule heat generation [21]. E-glass is expected to behave in a similar way, with a temperature limit based on its fiber melting temperature of 1500 K. Glass fibers begin to soften around temperatures of 943 K and melt at temperatures near 1500 K [22]. Therefore, it is logical to assume that the maximum temperature of the E-glass composite is governed by this fiber melting temperature of 1500 K. Similar to Ogasawara's study, composite surface temperature is limited to the fiber melting temperature during E-glass melting in the heat transfer model. However, different glass composites have different melting temperatures, depending on glass fiber diameter, volume fraction of the laminate, and resin matrix properties. In addition, the difference between resin thermosets and thermoplastics results in a wide range of potential laminate melting temperatures. To simplify analyses, heat transfer for E-glass composite material is designated to have a material temperature limit of 1500 K, understanding that if a specific composite has a lower melting temperature, more material will be ablated away.

A simple study was done to determine the amount of copper ablated and the amount of E-glass composite sublimated for a 200 microsecond lightning pulse. Abaqus-CAE, a finite element modeling tool, was used to model the one-dimensional heat transfer due to lightning heat flux for both copper and E-glass composite. The analysis was done for a 1 mm length of material with a constant surface heat flux of $4.6 \times 10^{10} \text{ W/m}^2$ for the entire 200 microsecond

lightning impulse. The latent heat of copper is included in the material properties in Abaqus. The study was done to represent a lightning strike to a small copper puck, representing an external lightning receptor, to determine the amount of ablation that occurs during a lightning strike. The geometry, loads, and boundary conditions are described in the finite element input file, shown in Appendix A.3 and a temperature contour plot for copper is shown in Figure 3-2.

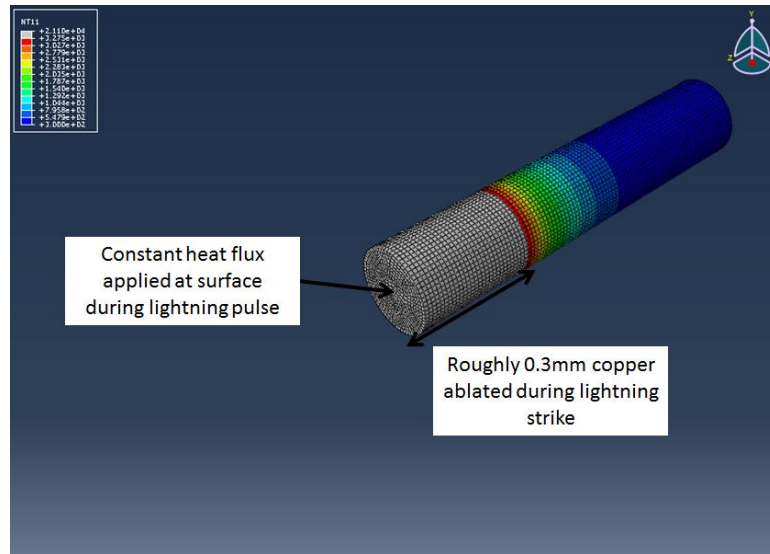


Figure 3-2: Temperature contour plot for a copper puck with a length of 1 mm

The gray portion of the contour is the amount of material greater than 2868 K, the vaporization temperature of copper. Roughly 0.3 mm of material is assumed to be ablated away. A similar analysis is done for E-glass composite material. Temperature vs. material depth plots for copper and E-glass composite are shown in Figure 3-3 and Figure 3-4, respectively.

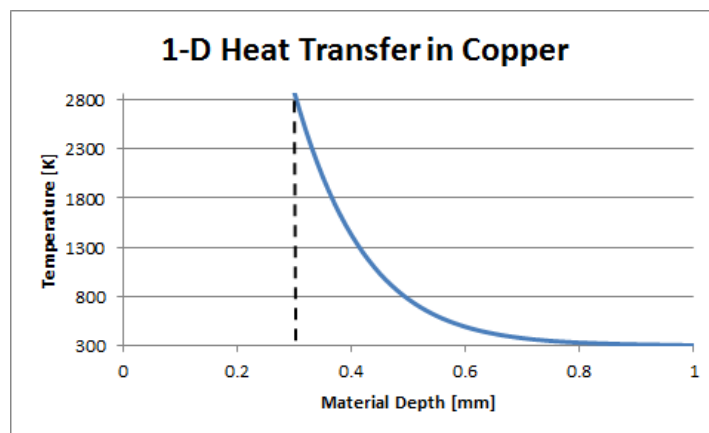


Figure 3-3: Temperature as a function of depth for copper

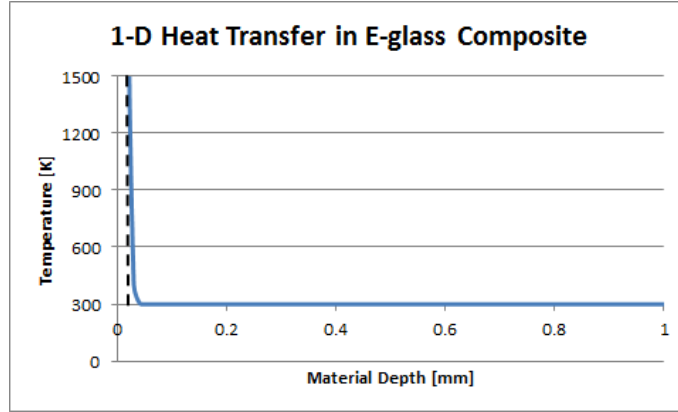


Figure 3-4: Temperature as a function of depth for E-glass composite

Note that roughly 0.3 mm of the copper in Figure 3-3 is expected to ablate as it is above the vaporization temperature of the material. Similarly, E-glass melts at 1500 K, which occurs up to a depth of roughly 0.025 mm into the material. The smaller depth of penetration in E-glass composite is attributed to its lower thermal conductivity.

In addition for finite element analysis, an analytical approach was taken to check the validity of the Abaqus model. Using the value for lightning flux calculated earlier, 4.6×10^{10} W/m², and known material properties, it is possible to calculate the one-dimensional temperature due to transient conduction for a constant surface heat flux [23]. The temperature, as a function of material depth and time, is

$$T(x, t) = \frac{2q'' \cdot (\alpha t / \pi)^{1/2}}{k} \cdot e^{-x^2 / 4\alpha t} - \frac{q'' \cdot x}{k} \cdot \operatorname{erfc}\left(\frac{x}{2\sqrt{\alpha t}}\right) \quad 3-3$$

where α is material thermal diffusivity and k is thermal conductivity. Calculations are shown in Appendix A.4. Solving for temperature at the end of the 200 microsecond lightning strike, it is determined that copper material is above the vaporization temperature of 2868 K down to a depth of 0.218 mm. This is very close to the depth calculated using the Abaqus model, 0.3 mm. In order to account for the amount of E-glass composite damage due to a direct lightning strike to the blade material, this analysis is repeated using E-glass composite material properties, shown in Appendix A.4. The material is found to be above the melting temperature of E-glass, 1500 K, down to a depth of 0.019 mm. This is of the same order as the Abaqus model results of roughly 0.025 mm. Any discrepancies between the results can be attributed to the robust nature of the Abaqus model, which accounts for temperature dependence of the material properties as

well as material directionality. Estimating that an E-glass composite material melts at about 950 K (the temperature at which the yield strength of the material is zero), the ablated material depth is calculated to be 0.0275 mm. It is important to note that the calculation does not include the latent heat energy that goes into melting the material from solid to liquid phase, but since the depth of heat penetration during lightning strike is so small, less than 3% of the thickness of the first composite sheet, it is deemed acceptable to continue with analysis. Including latent heat would decrease the thickness of heat penetration, so it is conservative to estimate an ablation thickness of between 0.025 mm and 0.0275 mm, depending on the particular fiberglass material properties and the associated melting temperature. For calculations, this is assumed to be 1500 K, the upper value of the range of fiberglass composite melting temperatures. If the lower value of the range were assumed, 950 K, then 0.0025 mm of additional material would be ablated away during lightning strike.

The calculated depth of material lost to ablation (for lightning striking the copper contact of a lightning protection system) or E-glass damage (due to sublimation and delamination from direct lightning strikes to the blade material) is relatively small and is a reasonable amount to see in field operation. Testing has shown that copper samples performed better than several other metallic samples when subjected to lightning current tests in terms of material erosion [2]. The results agree with these calculations, where the depth of surface melting penetrated to less than 1 mm. The study goes further to say that while some material became molten and then re-solidified, it can be assumed that the centrifugal forces of a rotating blade in the field would result in some small amount of material to be “lost,” during a real lightning strike [2]. For the remainder of the heat transfer analysis, finite element modeling continues under the assumption that a negligible amount of material is lost to ablation or sublimation and that the surface temperature of copper is limited to its vaporization temperature and the surface temperature of E-glass composite is limited to its fiber melting temperature.

3.3. Temperature-Dependent Material Properties

The best option for obtaining values for material properties, especially temperature-dependent material properties, would be to choose material testing for the particular temperature ranges and properties required for analysis. For the simulations, it was concluded that standard

material properties and literature research would generate acceptable values. Future research is needed to delve into a detailed analysis for specific material samples.

For the calculations, typical material properties are selected, and, when available, specific temperature-dependent strength and heat transfer properties are extracted from published sources. The following section highlights the material parameters used for calculations and any associated assumptions for the four materials used for analysis: copper external lightning receptor, rigid PVC foam core within the blade, carbon composite spar cap (assumed to have properties similar to T300 carbon composite), and fiberglass composite material (assumed to have properties similar to E-glass composite).

The external copper lightning receptor is defined as pure copper, which is assumed to be homogenous and isotropic. Copper has a melting temperature is 1356.6 K and a vaporization temperature of 2868 K, with a latent heat of fusion of 205 kJ/kg [24], [25]. It is assumed that any material above the vaporization temperature of copper is ablated away, but the latent heat of the solid-liquid phase change is input into Abaqus for analysis. Abaqus also allows for the input of temperature-dependent material properties, assuming a linear relationship between points. Table 3-2 includes the material properties for copper at various temperatures.

Table 3-2: Copper Material Properties [24], [26]

Temperature [K]	Thermal Conductivity [W/m-K]	Coeff. of Thermal Expansion [10^6 m/m-K]	Specific Heat [J/kg-K]	Density [kg/m ³]	Modulus of Elasticity [GPa]	Poisson's Ratio [-]
273	401	-	-	-	-	0.343
293	-	16.4	-	8930	129	
300	398	-	385	-	-	
373	-	16.4	-	-	125	
400	-	-	398	-	-	
523	-	18.5	-	-	-	
593	-	-	-	-	114	
600	-	-	417	-	-	
700	372	-	-	-	-	
723	-	20.2	-	-	-	
740	-	-	-	-	107	
800	-	-	432	-	-	
873	-	-	-	-	100	
1000	357	-	451	-	-	
1198	-	24.8	-	-	-	
1250	335.13	-	-	-	-	
1300	331.71	-	506	-	-	
1356.6	329.37*	26.3*	-	7940	-	
*Extrapolated value						

Appendix B.1 outlines the linear extrapolation calculations for thermal conductivity and the coefficient of thermal expansion. Both behave linearly for copper [26].

The rigid PVC foam blade core is not involved with heat transfer analysis, only in the blade condition monitoring analysis, so temperature-dependent properties are not required. It is

assumed to be homogenous and isotropic. Table 3-3 gives the room temperature properties input into Abaqus for analysis.

Table 3-3: Rigid PVC Foam Material Properties for Turbine Blade Core [24], [27], [28]

Thermal Conductivity [W/m-K]	Coeff. of Thermal Expansion [10 ⁶ m/m-K]	Specific Heat [J/kg-K]	Density [kg/m ³]	Modulus of Elasticity [GPa]	Poisson's Ratio [-]
0.032	35	1500	150	0.128	0.32

The carbon composite spar cap material properties are modeled closely to those of T300-epoxy carbon composite, a typical material used for wind turbine blade spar caps. In addition to being used in the blade condition monitoring analysis, the carbon composite is used in the heat transfer analysis. However, beneath five sheets of E-glass composite, it receives relatively small temperature increases, and therefore the material properties are assumed constant or linear where temperature-dependent properties are available. High temperature properties of carbon and glass composites have not yet been extensively studied and only limited experimental data have been reported in the literature regarding the material properties at elevated temperatures [29]. Carbon composite is transversely isotropic, having different material properties in the direction of the fiber axis from the transverse directions. The physical and thermal properties are symmetric about the fiber-axis, which is normal to the plane of isotropy. In Abaqus, the material directionality is defined as axes 1, 2, and 3 (in reality there are slight directional differences between the transverse and the thickness-directions with real prepreg materials because of the additional interlayer resin in the thickness-direction, but this additional resin is neglected in the model). The material properties are input with 1 being the fiber-direction, 2 being the transverse-direction, and 3 being the sheet thickness-direction, which is also transverse to the fiber-direction. The density, specific heat, and directional dependent thermal conductivities are given in Table 3-4.

Table 3-4: Density, Specific Heat, and Thermal Conductivity of Carbon Composite [21], [30], [31]

Density [kg/m ³]	Specific Heat [J/kg-K]	Thermal Coefficient [W/m-K]		
		<i>Fiber-Direction</i>	<i>Transverse-Direction</i>	<i>Thickness-Direction</i>
1500	1500	80.5	7.09	7.09

The temperature dependence of mechanical and thermal expansion properties were studied over a small temperature range for T300-epoxy carbon composite [32]. Material property data were fit to second and third order curves as functions of temperature over a range from about 100 – 400 K. However, from 300 – 400 K, the temperature range of interest, the data is nearly linear. Compared to E-glass composite, the carbon composite has relatively small temperature increases during lightning strike such that constant or linear material properties are assumed to be accurate. Hyer et al. provide second and third order equations and associated coefficients to accompany the least-squares fit curves for the material property test data [32]. Appendix B.2 shows how the equations are applied at 300 K and 400 K to obtain material property values at those temperatures. The results are shown in Table 3-5.

Table 3-5: Elastic and Thermal Expansion Properties Based on Temperature-Dependent Material Test Data [32]

	Coefficient of Thermal Expansion [10 ⁶ m/m-K]		Modulus of Elasticity [GPa]		Shear Modulus [GPa]	Poisson's Ratio [-]
	<i>Fiber-Direction</i>	<i>Transverse-Direction</i>	<i>Fiber-Direction</i>	<i>Transverse-Direction</i>		
300 K	-0.80	108	147	10.5	36.9	0.298
400 K	8.4	2770	156	11.4	58.9	0.204

For orthotropic materials, Abaqus requires the elastic material properties to be input as values of the stiffness matrix of the material [33]. Since the stiffness matrix for transversely isotropic materials is a simplified stiffness matrix for orthotropic materials, this requires the conversion of directional elastic material properties to stiffness matrix coefficients of the form:

$$\begin{pmatrix} \sigma_{11} \\ \sigma_{22} \\ \sigma_{33} \\ \sigma_{12} \\ \sigma_{13} \\ \sigma_{23} \end{pmatrix} = \begin{bmatrix} D_{1111} & D_{1122} & D_{1133} & 0 & 0 & 0 \\ D_{1122} & D_{2222} & D_{2233} & 0 & 0 & 0 \\ D_{1133} & D_{2233} & D_{3333} & 0 & 0 & 0 \\ 0 & 0 & 0 & D_{1212} & 0 & 0 \\ 0 & 0 & 0 & 0 & D_{1313} & 0 \\ 0 & 0 & 0 & 0 & 0 & D_{2323} \end{bmatrix} \begin{pmatrix} \epsilon_{11} \\ \epsilon_{22} \\ \epsilon_{33} \\ \gamma_{12} \\ \gamma_{13} \\ \gamma_{23} \end{pmatrix} \quad 3-4$$

The process of converting the elastic material properties into stiffness matrix coefficients is shown in Appendix B.3, in which the Abaqus Analysis User's Manual provides definitions for each stiffness matrix term [33]. The resulting stiffness coefficients are shown in Table 3-6.

Table 3-6: Stiffness Matrix Terms for T300-Epoxy Elastic Property Inputs into Abaqus

Stiffness Matrix Term [MPa]	D1111	D2222	D3333	D1122	D1133	D2233	D1212	D1313	D2323
300 K	150.2	12.69	12.69	5.328	5.328	5.189	36.87	36.87	3.750
400 K	157.7	13.67	13.67	3.916	3.916	5.526	58.87	58.87	4.071

The fiberglass-epoxy composite sheet properties input into Abaqus are representative of E-glass composite, a typical material used for turbine blade skins. Temperature-dependent elastic and heat transfer properties are required for analysis. The density and coefficient of thermal expansion are constant values, provided in Table 3-7.

Table 3-7: Density and Coefficient of Thermal Expansion of Fiberglass-Epoxy Composite [34]

Density [kg/m ³]	Coefficient of Thermal Expansion [10 ⁶ m/m-K]		
	<i>Fiber-Direction</i>	<i>Transverse-Direction</i>	<i>Thickness-Direction</i>
2100	7.0	21.0	21.0

Cecen et al. investigated the temperature dependence of thermal conductivity in the transverse-direction and the specific heat by means of heat-flux differential scanning calorimetry (DSC) [35]. The plots from the test data are provided in Appendix B.4, but in order to input the information into Abaqus, the plots had to be transcribed into Excel. The transcribed test results are shown in Figure 3-5 and Figure 3-6. The thermal conductivity test data had multiple

measurements taken at each measured temperature point, so the average conductivity was taken at each temperature measurement.

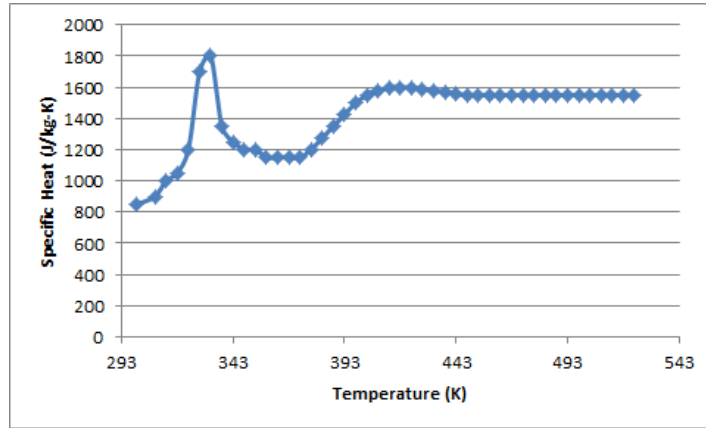


Figure 3-5: Specific heat of fiberglass-epoxy composite obtained from DSC experiments and transcribed to Excel [35]

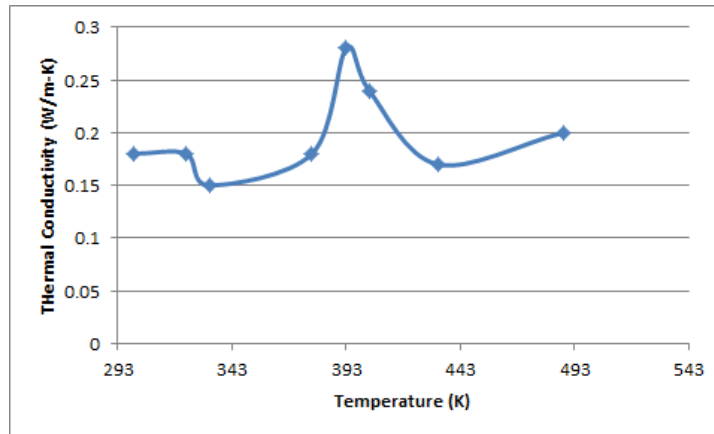


Figure 3-6: Thermal conductivity of fiberglass-epoxy composite material in the transverse-direction obtained from DSC experiments and transcribed to Excel [35]

Cecen et al. provide thermal conductivity values for glass fiber material, 1.03 W/m-K, and for epoxy matrix material, 0.049 W/m-K [35]. Using the volume fraction method of calculating composite material properties, the thermal conductivity of fiberglass-epoxy composite material in the fiber-direction is determined. The conductivity in the fiber-direction is

$$k_1 = k_f V_f + (1 - V_f) k_m \quad 3-5$$

where k_f is the thermal conductivity of the glass fibers, k_m is the thermal conductivity of the epoxy matrix, and V_f is the fiber volume fraction, 55%, which is a typical fraction for E-glass composites [34], [36]. Appendix B.5 shows the calculations, determining the thermal

conductivity in the fiber-direction to be 0.589 W/m-K, which is the same magnitude as the conductivity in the transverse and thickness-directions. Most of the temperature dependence in the thermal conductivity was found to be the result of phenomena in the epoxy rather than the glass fibers. It is therefore determined that the thermal conductivity in the fiber-direction can be assumed to be constant as the temperature of the composite increases. The values from the transcribed specific heat plot, Figure 3-5, are entered into the Abaqus material property list. The orthotropic, temperature-dependent thermal conductivity values are also input, with conduction in the fiber-direction remaining constant as a function of temperature, and conduction in the transverse and thickness-directions following the data points in Figure 3-6.

Knowing the elastic moduli and Poisson's ratios of E-glass fibers and epoxy resin at various temperatures, it is possible to calculate the transversely isotropic elastic properties of E-glass composite material by using the volume fraction method described above. Replacing the thermal conductivity with modulus of elasticity or Poisson's ratio:

$$E_1 = E_f V_f + (1 - V_f) E_m \quad 3-6$$

$$\nu_1 = \nu_f V_f + (1 - V_f) \nu_m \quad 3-7$$

Understanding the relationship between the fiber and transverse-directional properties, the modulus of elasticity in the transverse-direction can be determined:

$$E_2 = \frac{E_m}{[V_f(E_m/E_f - 1) + 1]} \quad 3-8$$

In addition, knowing the modulus of elasticity and Poisson's ratio of E-glass fiber, the shear modulus of E-glass fiber can be found with the expression:

$$G_f = \frac{E_f}{2(1+\nu_f)} \quad 3-9$$

the shear modulus of the epoxy matrix is found using the same equation. Knowing these values, it is possible to ascertain the shear modulus of the E-glass composite material with a modified form of the volume fraction equation:

$$G_{12} = \frac{1}{V_f/G_f + V_m/G_m} \quad 3-10$$

where V_m is related to V_f with the relationship:

$$V_m = 1 - V_f \quad 3-11$$

Table 3-8 provides values for E-glass fiber and epoxy matrix elastic properties to be used for calculating composite material properties.

Table 3-8: Fiber and Matrix Elastic Properties Used to Calculate E-glass Composite Elastic Properties [37], [38]

	Modulus of Elasticity – Fiber [GPa]	Poisson’s Ratio – Fiber [-]	Modulus of Elasticity – Matrix [GPa]	Poisson’s Ratio – Matrix [-]
300 K	72.3	0.22	4.6*	0.36*
811 K	81.3	0.20	4.6*	0.36*
*Matrix properties selected to match room temperature composite properties with known values				

Matrix properties are presented as a range of potential values, so the properties in Table 3-8 are selected such that the calculated room temperature E-glass composite properties agree with known values [34]. Appendix B.6 shows that utilizing the equations above, elastic properties for E-glass composite material can be found. The results are shown in Table 3-9.

Table 3-9: Calculated Elastic Properties for E-glass Composite

	Mod of Elasticity – Fiber-direction [GPa]	Mod of Elasticity – Transverse-direction [GPa]	Shear Modulus [GPa]	Poisson’s Ration [-]
300 K	41.84	9.485	3.513	0.283
811 K	46.79	9.561	3.542	0.272

Similar to the orthogonal carbon composite properties, the stiffness matrix coefficients for E-glass composite must be calculated for Abaqus. The process of converting the elastic material

properties of E-glass composite into stiffness matrix coefficients is shown in Appendix B.3. The resulting stiffness coefficients are provided in Table 3-10.

Table 3-10: Stiffness Matrix Terms for E-glass Composite Elastic Property Inputs into Abaqus

Stiffness Matrix Term [MPa]	D1111	D2222	D3333	D1122	D1133	D2233	D1212	D1313	D2323
300 K	44.09	10.80	10.80	4.047	4.047	3.50	3.51	3.51	3.65
811 K	48.91	10.81	10.81	3.882	3.882	3.46	3.54	3.54	3.677

It is important to know the directional material strength of E-glass composite because it is used to determine the presence and extent of material damage due to plastic deformation. Room temperature strength values for E-glass composite material have been researched extensively, and provided in Table 3-11.

Table 3-11: E-glass Composite Directional Material Strengths at Room Temperature [34]

Fiber-Direction Tensile [MPa]	Fiber-Direction Compressive [MPa]	Transverse-Direction Tensile [MPa]	Transverse-Direction Compressive [MPa]	Shear (Fiber-Transverse-direction) [MPa]
1080	620	39	128	89

Material tests at elevated temperature show that glass fiber reinforced polymer (GFRP) strength decreases as a function of temperature between room temperature and 943 K almost linearly [39]. While GFRP has different material strengths at room temperature than those found in Table 3-11, it is assumed that the rate of strength decrease in the fiberglass test data is the same rate of decrease for E-glass composite. Appendix B.7 reveals how the test data from two materials with different diameter fibers is averaged together at each temperature point, resulting in average yield strength as a function of temperature. This data is then divided by yield strength at room temperature to get a normalized plot which can be applied to E-glass composite material. Figure 3-7 shows the normalized fiberglass composite yield strength, in which the material

strength decreases linearly with temperature until 943 K, at which point the material has no strength and will therefore yield under any stress.

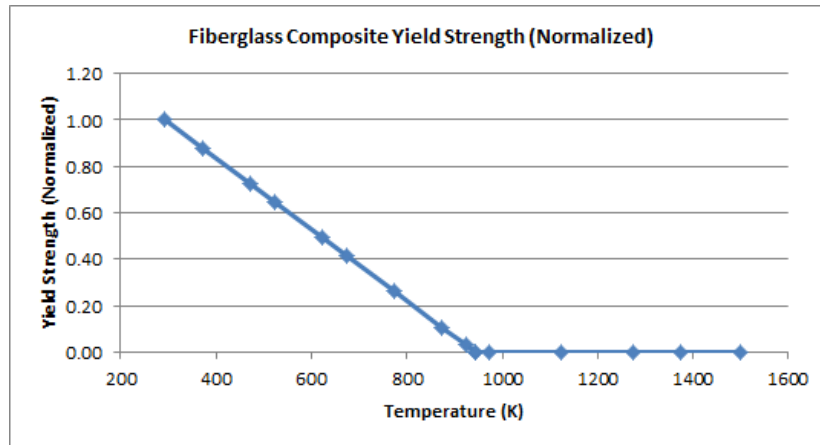


Figure 3-7: Normalized Fiberglass Composite Yield Strength from Material Test Data [39]

Using the directional room temperature strength values from Table 3-11, the temperature-dependent yield strengths are obtained for E-glass, shown in Figure 3-8.

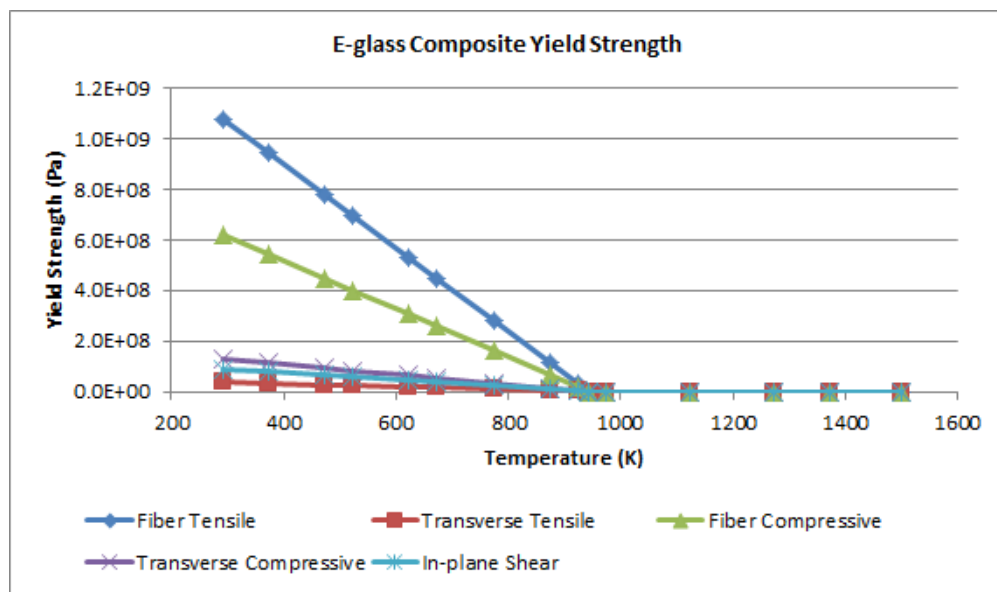


Figure 3-8: Directional E-glass Composite Yield Strength as a Function of Temperature

4. Extent of Damage Caused by Lightning Strike

4.1. Computational Method

The ultimate goal of this chapter is to determine the extent of thermal stress resulting from a lightning strike to a wind turbine blade in order to determine whether plastic strain is present. This requires combined heat transfer and stress analyses for a sample of representative turbine blade material. Analysis consists of direct lightning attachment to the fiberglass composite blade surface as well as attachment to an external lightning protection receptor. The high temperatures resulting from lightning strike necessitates a finite element thermomechanical model. In today's industry, finite element modeling is used extensively to predict the behavior of materials under severe conditions [31]. Abaqus-CAE Version 6.11-2, a finite element modeling tool, is used to model the turbine blade segment for heat transfer and stress analyses.

A square plate of blade material is used to represent the blade surface during lightning strike. This model is used to simulate a lightning strike for 200 microseconds, and then continues to run after the strike occurs in order to find the thermal gradient as time passes. The model is a square region of material 45 mm in length, measuring 20 mm thick, which is thinner than a full turbine blade airfoil skin, but the reduction in thickness is necessary to reduce computation time. For the model simulating an external copper lightning receptor, a 20 mm diameter is partitioned at the center of the plate. The same area is partitioned for models simulating a direct lightning strike to the composite blade material in order to keep the lightning strike area constant between models.

Simulating an accurate model of the surface of a turbine blade requires the input of appropriate material properties and directionality when necessary. The model represents the surface of a segment of turbine blade (located near the blade tip above the spar cap for this analysis as a worst-case scenario), which consists of biaxial E-glass composite sheets. The entire blade skin includes a 5-ply ($\pm 45,0$) layup of E-glass composite sandwiching a unidirectional carbon composite spar cap. Abaqus allows for material directionality to be assigned, so the model is partitioned into segments of differing composite sheet directions. Material properties and directionality discussed in Chapter 3 are input into Abaqus to represent the turbine blade

materials of interest. Figure 4-1 shows the three material segments for the first two E-glass layers of the model. This example includes a partitioned copper center, representing a copper lightning receptor. The copper receptor is assumed to be isotropic and is thus given an arbitrary directionality in picture A. The first layer of E-glass composite is oriented +45 degrees about the thickness axis, as shown in the red highlighted region in picture B, and the second layer is oriented -45 degrees about the thickness axis, shown in picture C. The example shown in Figure 4-1 continues past the first two E-glass layers, but in order to present a clear image, only the first two composite layers are shown, with each layer being 1 mm.

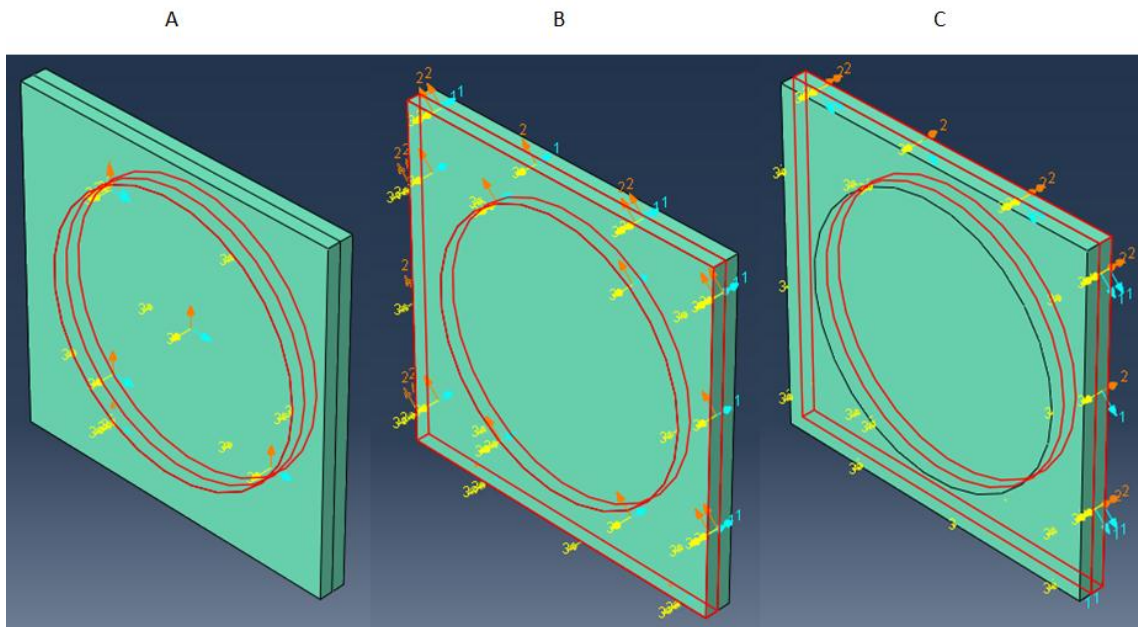


Figure 4-1: Directionality of copper receptor and biaxial E-glass sheets for first two composite layers of the model

In contrast, the full model is 20 mm thick, including all 5 sheets of surface E-glass composite material at the blade surface and 15 mm of the unidirectional carbon composite spar cap. The first and fifth sheet are assigned a +45 degree orientation, the second and fourth a -45 degree orientation, and the third sheet is assigned a zero degree rotation about the axis in the thickness-direction. The remaining volume of the plate is assigned unidirectional carbon composite material properties. Figure 4-2 illustrates the material and directionality assignments for the full thermomechanical model. Note that the circular partition at the front face of the plate has the same directionality as the first composite sheet. This is a model for a direct lightning strike to composite material; there is no copper lightning receptor and the material of each

composite sheet within the “lightning strike area” is therefore assigned the same material and directionality of its corresponding sheet outside of the partition.

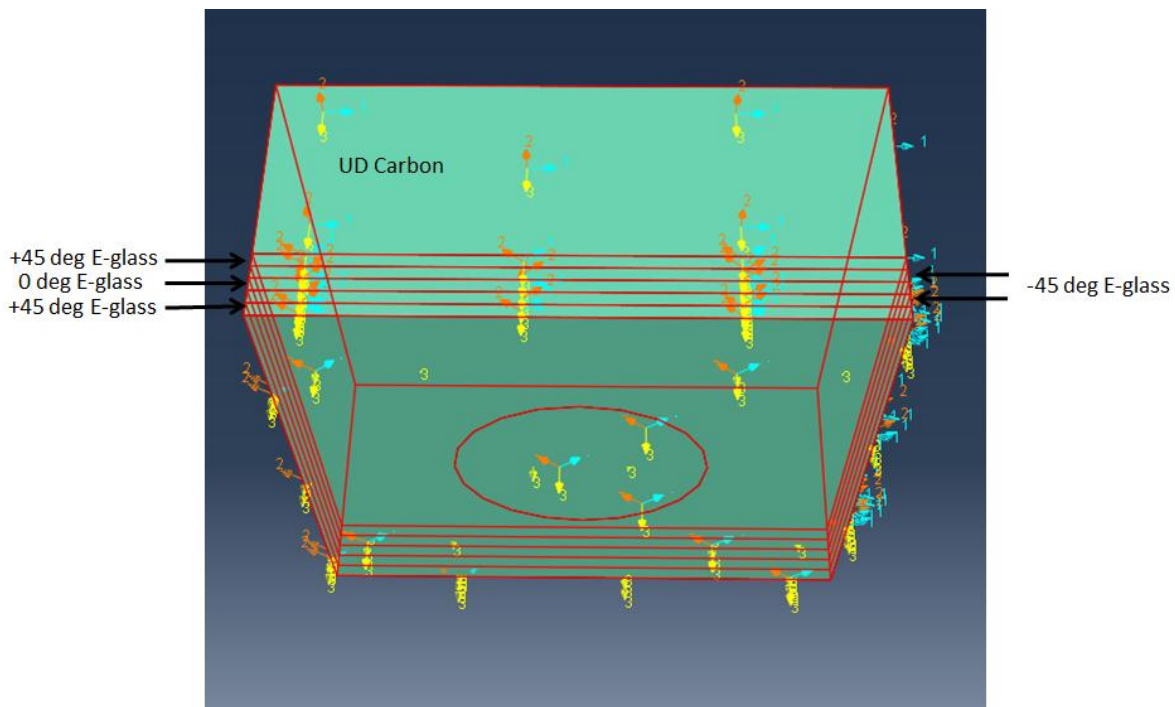


Figure 4-2: Material assignment for full plate model without a copper receptor

Absolute zero is set as -300 degrees for the entire model. Abaqus does not use unit systems, so the results depend on the user-input properties and constants. A measurement of zero degrees in the model is roughly equivalent to room temperature, or 300 K. The model is initially set at room temperature and allows heat to transfer out of the boundaries during analysis. Convection is the most accurate condition for heat transfer at the blade surface boundary of the plate, but the coupled temperature-displacement analysis in Abaqus prevents it as an input. This is deemed acceptable since the heat flux due to lightning strike is much greater than any heat dissipation due to convection directly after the strike. For complete accuracy of the heat transfer boundary condition at the plate surface, it is recommended that a study be completed which includes surface convection into the surrounding air. A surface heat flux of $4.6 \times 10^{10} \text{ W/m}^2$ is set to the partitioned 20 mm diameter region on the plate surface for 200 microseconds, after which the flux is subsequently set to zero. Figure 4-3 illustrates the heat flux input into the partitioned plate surface. The 3-2-1 method is used to set isostatic boundary conditions. Three points of the model are selected in which the first point constrains translation in all three directions, the

second point constrains rotation in two directions, and the third point constrains rotation in the last direction. The corner boundary conditions are shown in Figure 4-3.

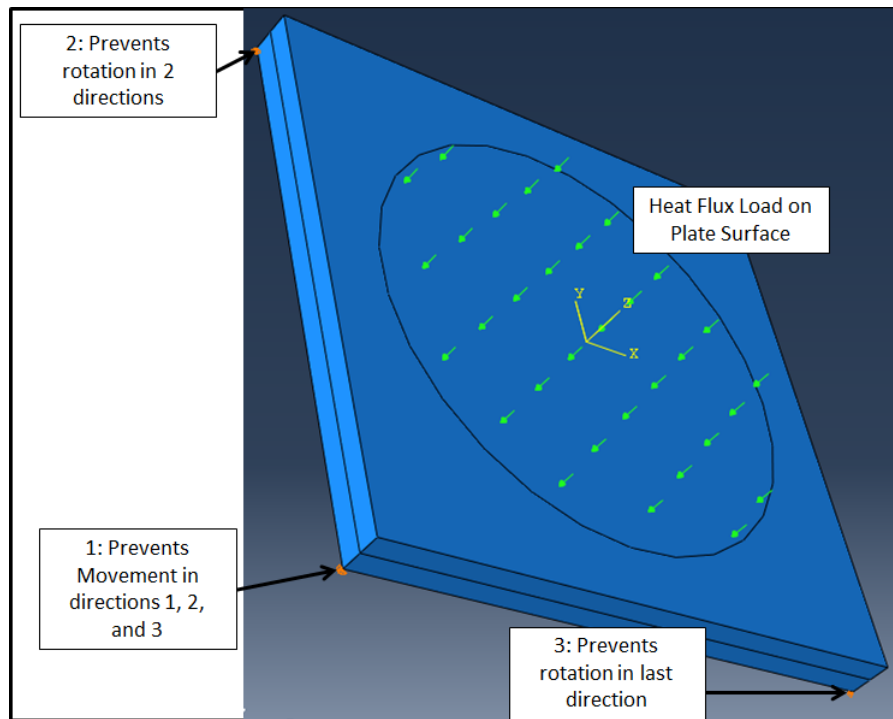


Figure 4-3: Boundary conditions and heat flux load for plate model

Abaqus allows for the simultaneous analysis of heat transfer and displacement in a model. This coupled analysis makes it possible to measure the thermal stress due to a simulated lightning strike. The model solves the transient three-dimensional heat equation:

$$\frac{\partial T}{\partial t} = \alpha_T \cdot \left(\frac{\partial^2 T}{\partial x^2} + \frac{\partial^2 T}{\partial y^2} + \frac{\partial^2 T}{\partial z^2} \right) \quad 4-1$$

where T is temperature, t is time, x, y, and z are spatial operators, and α_T is thermal diffusivity, defined as:

$$\alpha_T = \frac{k}{c_p \cdot \rho} \quad 4-2$$

where k, c_p , and ρ are thermal conductivity, specific heat capacity, and mass density, respectively, which are all material dependent properties. The coupled displacement aspect of the analysis allows the plate volume to expand given the material coefficient of thermal expansion, α . The resulting thermal strain is calculated as:

$$\epsilon_T = \alpha \cdot \Delta T \quad 4-3$$

where ΔT is the change in temperature between the initial temperature and final temperature for a node at each increment. Thermal stress is calculated knowing the thermal strain and the modulus of elasticity of the material given Hooke's Law:

$$\sigma = E \cdot \epsilon \quad 4-4$$

This yields an equation for thermal stress as a function of elastic modulus, coefficient of thermal expansion, and temperature change:

$$\sigma_T = E \cdot \alpha \cdot \Delta T \quad 4-5$$

The mesh is set such that the region of interest (the lightning strike area and immediate surrounding area) has a smaller mesh than the outer boundaries. This is done by setting a smaller mesh seed at the lightning strike partitioned region, and setting a somewhat larger seed around the outer boundaries. Similarly, the thickness-direction has differing mesh, with a smaller mesh directly next to the plate surface and a larger mesh toward the opposite boundary of the plate. Additional partitions are included to create constant node incrimination in the fiber-direction and in the transverse-direction of the composite. The reason for this is to create results that are easily comprehensible in the directions of interest. The running time is divided into two steps: the initial 200 microseconds in which lightning strike occurs called the "Lightning" step, and a pre-set time afterward to see the thermal gradient as time passes called the "After" step. Automatic time incrementation is set such that the initial increment, minimum, and maximum increments are set as inputs. These vary between models in order to maximize runtime efficiency. Abaqus starts computing with the initial increment until it finds the final increments converge quickly, at which time Abaqus automatically doubles the time increment. When there is no convergence, Abaqus sets the time increment smaller.

The heat flux input of $4.6 \times 10^{10} \text{ W/m}^2$ is manually limited to ensure that the surface temperature of the copper lightning receptor is constrained to the vaporization temperature of copper, 2868 K. The amplitude of the heat flux is decreased as a function of time during the lightning strike step so that the surface of the copper is limited to 2868 K for all time increments. The model in which lightning directly strikes E-glass composite is similarly limited to the glass fiber melting temperature of 1500 K, as explained in Chapter 3. Example Abaqus input files can

be found in Appendix C.1 (direct lightning strike to fiberglass blade surface material) and Appendix C.2 (lightning strike to copper protection receptor).

4.2. Thermomechanical Damage Results

The results from the two Abaqus models show the thermal diffusion as the heat from the lightning strike radiation flux spreads through the three-dimensional plate of blade surface material and the corresponding thermal stresses. Data is obtained from points in two directions, shown in Figure 4-4.

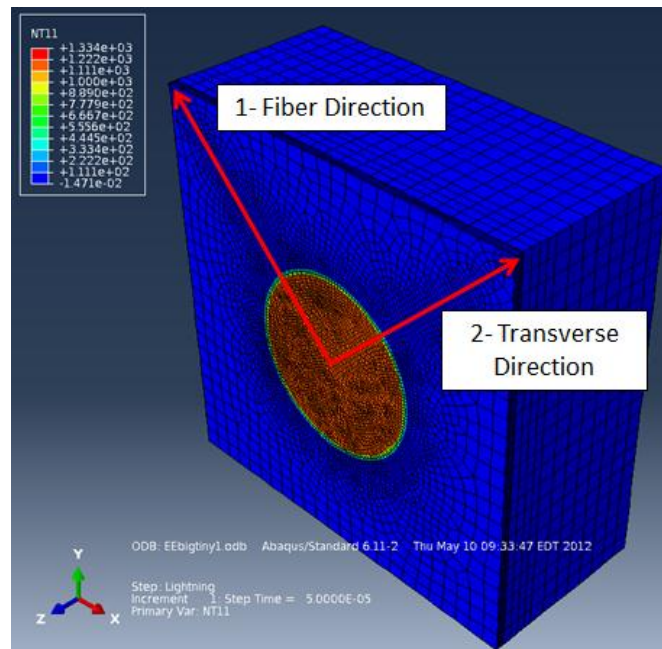


Figure 4-4: Data points analyzed in fiber-direction and transverse-direction (naming convention based on surface composite ply)

Data points in the 1-direction, named the “fiber direction,” fall along the fiber-direction of the first ply at the surface of the plate, and points in the 2-direction, the “transverse direction,” fall along the transverse-direction of the first ply. Since the plate surface is a 5-ply ($\pm 45,0$) layup of E-glass composite material, the second ply then reverses, and the points in the 1-direction now fall along the transverse-direction of the second ply. However, as the results later show, the temperature and thermal stresses deeper than the first E-glass composite ply are of little concern, so the naming convention is as follows: points along the 1-direction are described as being in the

fiber-direction of the first ply, and are therefore analyzed as S11 stresses, or the stresses in the fiber-direction of the material. Points in the 2-direction are in the transverse-direction of the first ply, and are analyzed as S22 stresses, which are the stresses in the transverse-direction of the material. This might not provide the most conservative results because depending on loading characteristics, various combinations of stress fields might result in lower material strength, rather than holding to either the S11 or S22 stresses. However, these loading cases were not addressed in this study. The analyzed points start at the center of the plate and continue in the fiber-direction or the transverse-direction to the end of the plate. As described earlier in this chapter, the plate is partitioned at a radius of 10 mm, termed the “lightning strike radius” because it is the boundary between the lightning strike heat input (represented as a radiation heat flux) and the blade material with no lightning attachment.

A thermal contour plot of a direct lightning strike to E-glass composite blade surface material is presented in Figure 4-5. The plot shows the nodal temperature in the plate, bisected along the y-axis to show the depth of thermal diffusion at 5 seconds after the lightning strike.

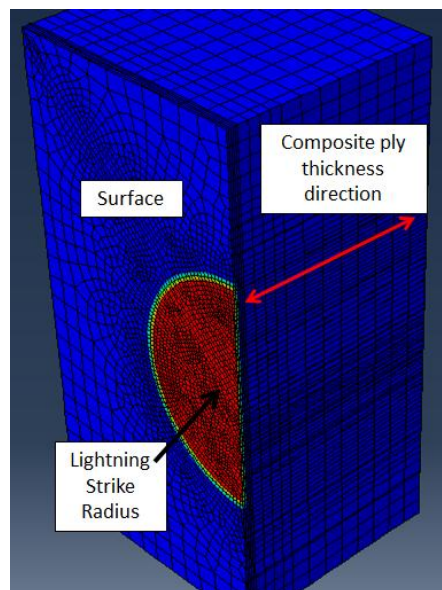


Figure 4-5: Thermal contour plot of direct lightning strike to composite material

Blue is room temperature whereas red is the hottest temperature, which is about 450 K 5 seconds after the lightning strike. Thermal diffusion is limited to the composite material immediately surrounding the lightning strike radius. This is due to the fact that the thermal conduction of E-

glass composite is extremely low. The contour plot of the model representing a strike to a copper blade lightning receptor is shown in Figure 4-6.

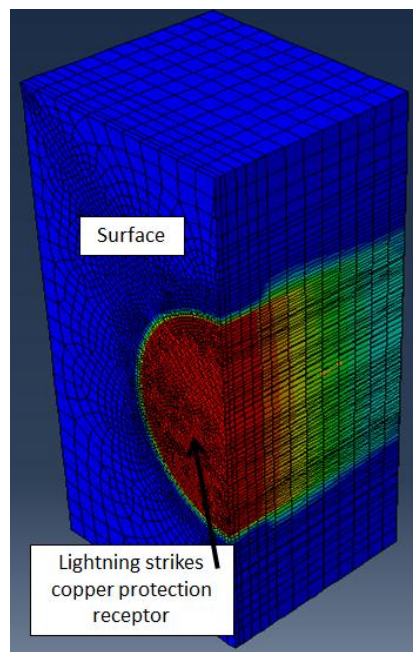


Figure 4-6: Contour plot of strike to copper lightning receptor

The contour is taken only 0.5 s after the lightning strike, and already the copper surface temperature has decreased from about 2750 K (nearing the vaporization temperature of the material) to only 360 K. Heat rapidly diffuses through the copper receptor because of a high thermal conductivity, whereas heat is slow to diffuse through composite material due to a relatively low conductivity. Note the expansion of the thermal gradient at a depth of 5 mm, the point at which the E-glass plies end and the carbon composite spar cap begins. This occurs because the thermal conductivity of carbon composite is greater than that of E-glass.

Before getting into the detailed results, it is important to see the stress contour plots of the thermomechanical plates to understand the general areas of tensile and compressive stress. Figure 4-7 shows the S11 (stress in the fiber-direction of the E-glass ply at the plate surface) stress contour plot for a direct lightning strike to composite material, focusing on the plate surface.

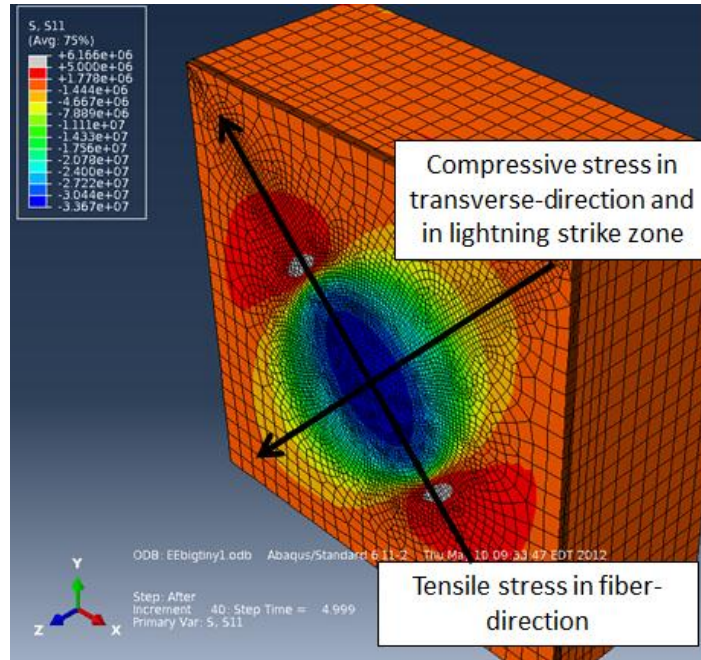


Figure 4-7: S11 contour plot for direct lightning strike to composite material, 5 s after lightning strike

As the figure shows, S11 stress in the transverse-direction and within the lightning strike zone is compressive (blue – yellow), whereas the stress in the fiber-direction is tensile (red). At the same time point, the S22 (the stress in the transverse direction of the first E-glass ply) contours are provided in Figure 4-8.

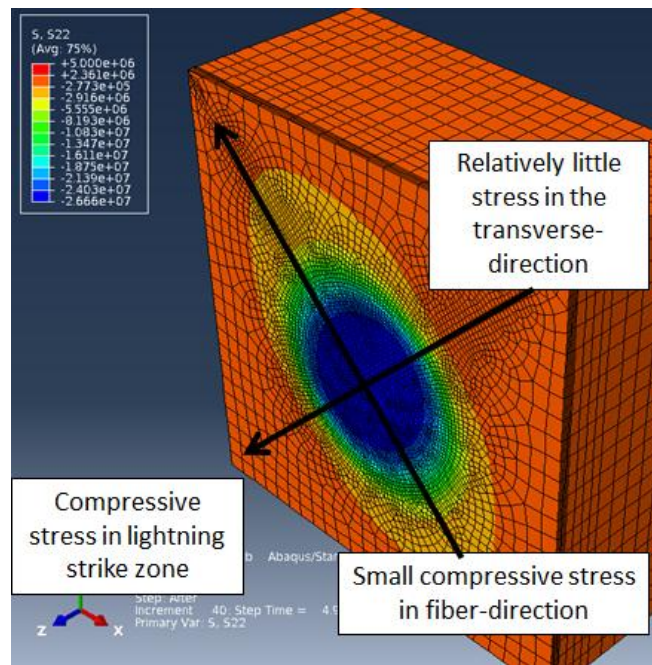


Figure 4-8: S22 contour plot for direct lightning strike to composite material, 5 s after lightning strike

Both figures show that stress in the lightning strike region is the highest in the entire plate and is compressive in nature, which is expected due to the fact that it has the highest temperature in the plate.

Focusing first on the model representing a direct strike to composite material, the Abaqus temperature and corresponding thermal stress results are presented in detail. A plot of temperature gradient as a function of radius from the center of the plate in the fiber-direction is shown in Figure 4-9. The plots show the temperature gradient from for multiple time steps up to 5 seconds after the lightning strike. The first time step of 0.0001 seconds represents a point in time halfway through the completion of the lightning heat flux, and the second time step of 0.0002 seconds represents a time at the completion of the lightning strike heat flux.

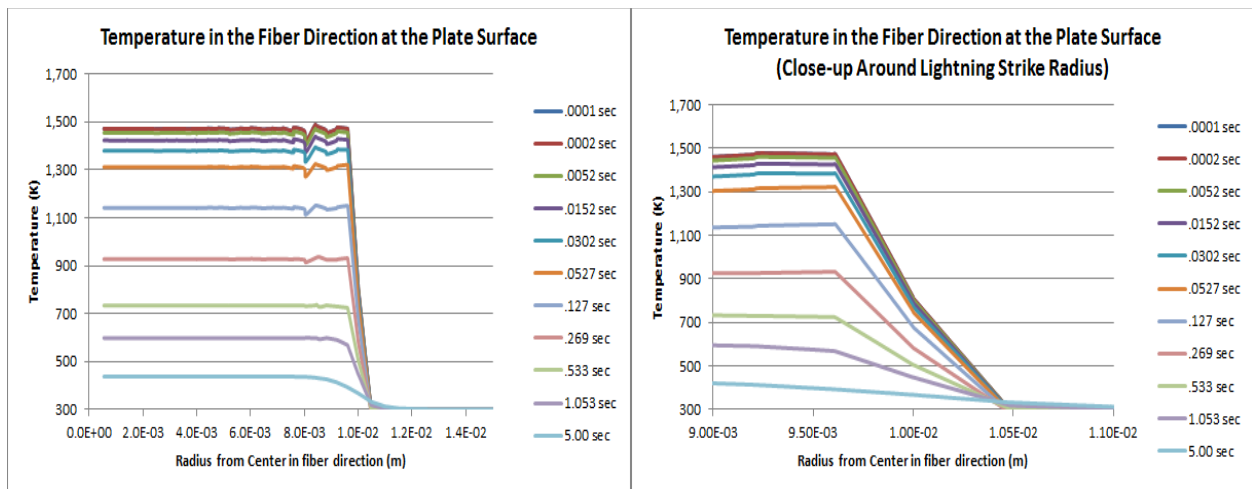


Figure 4-9: Thermal gradient as a function of radius from the plate center in the fiber-direction

It is clear to see that at the lightning strike radius, the boundary at which the lightning heat flux input is turned off, the surface temperature quickly falls off to room temperature within the next 0.5 mm radially for almost all time steps. This indicates that there is very little radial heat diffusion in the fiber-direction due to the low thermal conductivity of E-glass composite. The thermal gradient plot in the transverse-direction is almost identical, as shown in Figure 4-10, since the thermal conductivity in the transverse-direction is the same magnitude as the conductivity in the fiber-direction.

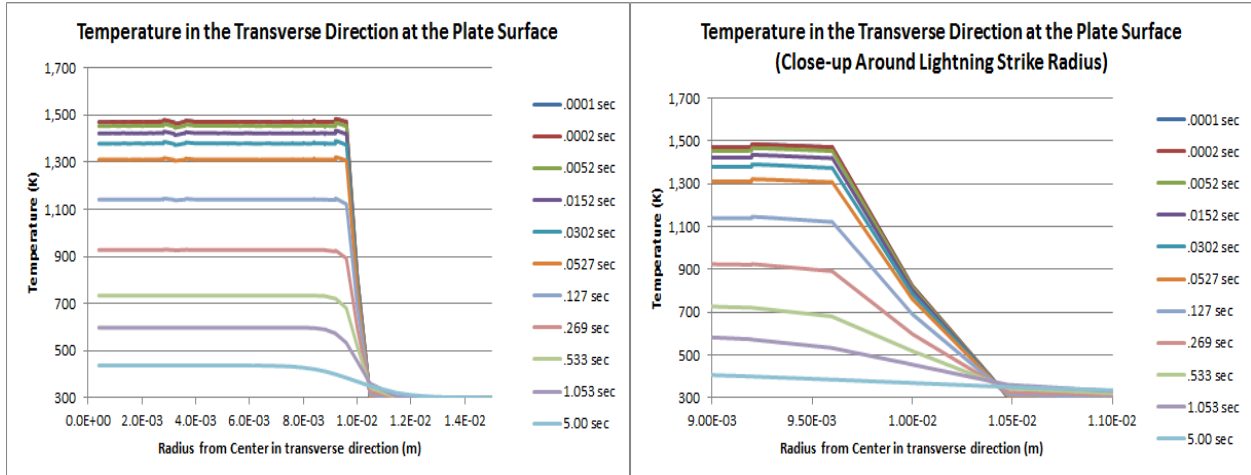


Figure 4-10: Thermal gradient as a function of radius from the plate center in the transverse-direction

It is important to look at the results at a time step at which the greatest amount of material damaged is observed. This occurs at a time step of 0.269 s after the lightning strike. Material damage is defined as a point at which plastic yielding occurs. In the fiber-direction, this occurs when the S11 stress exceeds the fiber-direction strength, and in the transverse-direction, this occurs when the S22 stress exceeds the transverse-direction strength (due to the fact that this is an elastic analysis of the material). Figure 4-11 shows a comparison of the thermal gradient and the corresponding thermal stress and material strength at the plate surface in the fiber-direction at 0.269 s after the lightning strike.

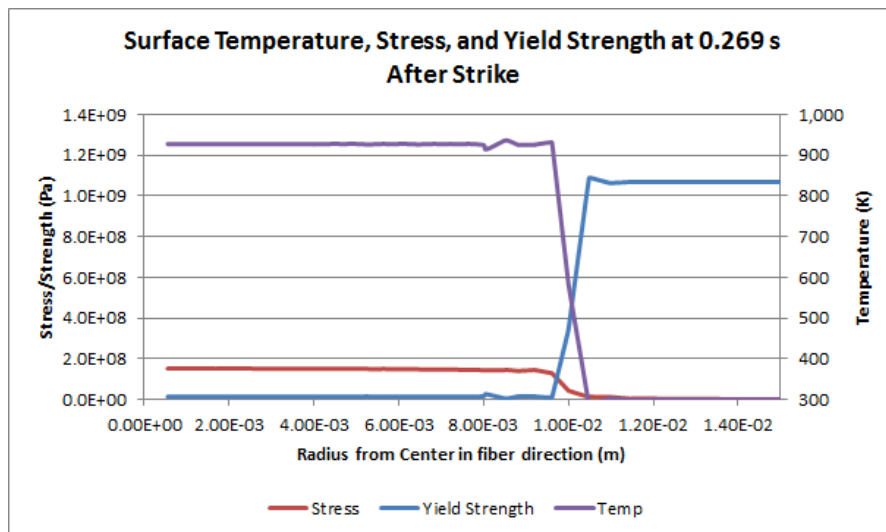


Figure 4-11: Fiber-direction surface temperature, stress, and material strength at 0.269 s after lightning strike

The material temperature at the surface, as presented in Figure 4-9, remains at about 930 K from the center of the plate to the lightning strike boundary, at which point it rapidly decreases to room temperature within 0.5 mm radially. The corresponding thermal stresses shift from compressive within the lightning strike radius to tensile outside of it, but the positive absolute values are given in order to make the comparison to material strength to determine the amount of material damage. As described in Chapter 3, the material strength is calculated as a function of temperature. At each node, the directional dependent material strength of the composite is calculated, accounting for differences in tensile or compressive strengths. See Appendix C.3 for an example of the material strength calculation logic. From the center of the plate to the lightning strike radius, the surface of the plate is nearly 943 K, the temperature at which the composite has zero material strength. All thermal stresses in the fiber-direction up to this boundary are greater than zero, at 147 MPa, and therefore all the material within the lightning strike radius plastically yields. Outside of this radius, the calculated composite yield strength quickly increases due to the much lower temperature, and is greater than the S11 strength. Figure 4-12 shows nearly identical results for the plate surface in the transverse-direction at 0.269 s after the lightning strike.

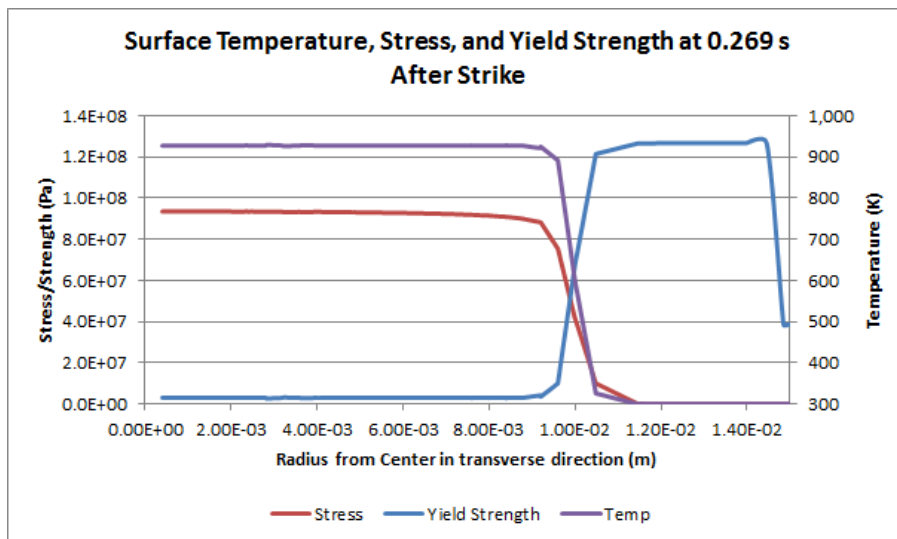


Figure 4-12: Transverse-direction surface temperature, stress, and material strength at 0.269 s after lightning strike

The thermal stress in the transverse-direction is 92 MPa from the center of the plate to the lightning strike radius, and decreases to relatively low values at nearly the same rate as the temperature. With the decrease in temperature, the yield strength of the material increases to a

point at which plastic yielding no longer occurs, within 0.5 mm outside of the lightning strike radius. The decrease in material strength at roughly 15 mm from the center of the plate is the point at which the stresses switch from compression to tension. The calculated material strength reflects that change.

Noting that the radial composite damage at the plate surface extends from the plate center to less than 0.5 mm outside of the lightning strike radius, it is necessary to determine the amount of damage that occurs depth-wise. The fiber-direction temperature results at 0.269 s after the lightning strike are presented in Figure 4-13 A and B. The associated stresses and yield strengths for relevant depth levels are shown in C and D.

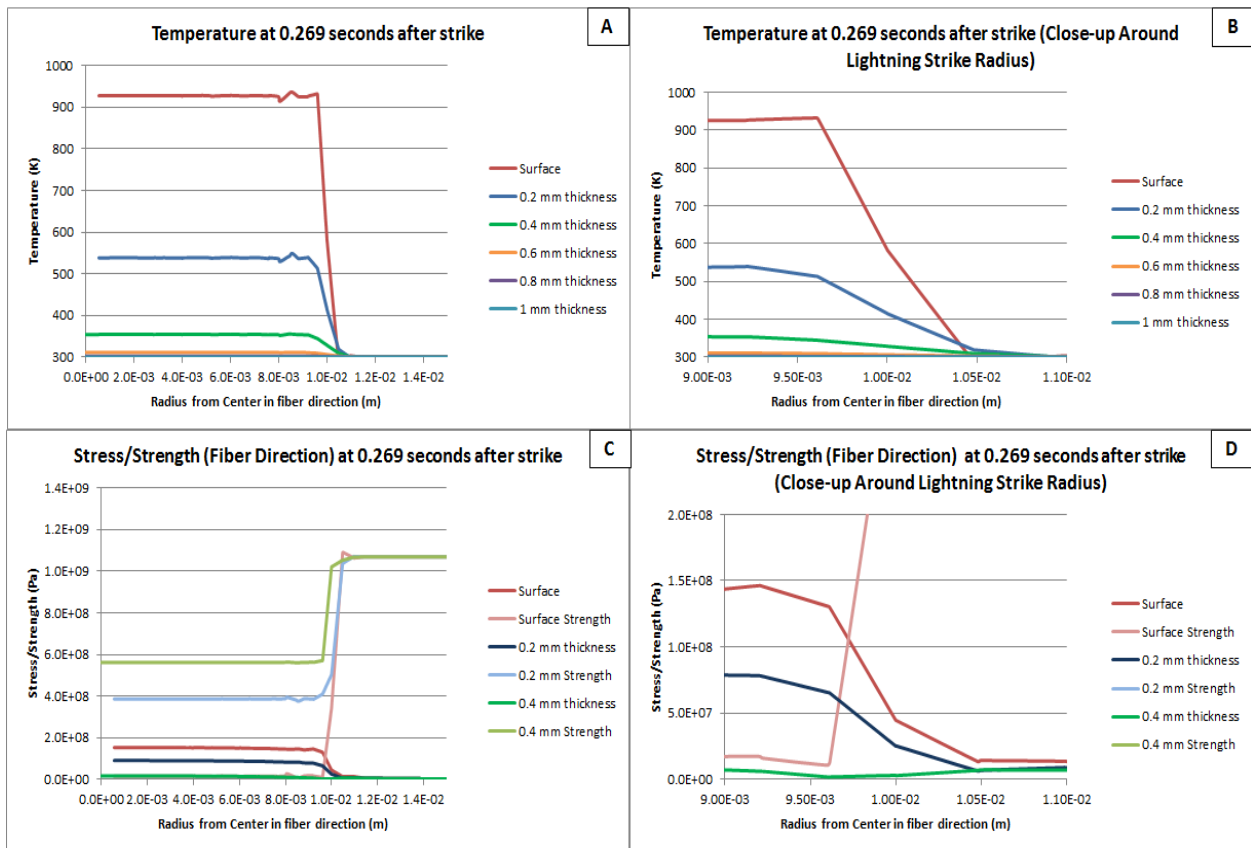


Figure 4-13: Temperature, stress, and composite strength distributions at different depths within the plate at 0.269 s after the strike in the fiber-direction

Figures A and B show that below 0.4 mm, the temperature of the composite is nearly room temperature across the entire plate. Radially, the temperature rapidly decreases to room temperature within 0.5 mm outside the lightning strike radius at all depths, as observed at the blade surface. The stresses and yield strengths are provided for the relevant depth intervals (the

plate surface, 0.2 mm below the surface, and 0.4 mm below the surface) in Figure 4-13 C and D. Figure C shows that at 0.2 and 0.4 mm below the plate surface, the yield strength is greater than the S11 stress of the material, indicating that no plastic yielding occurs. The material temperature within the lightning strike radius is enough such that the yield strength is well below the room temperature value, but not to the point where it is less than the S11 stress. The findings show that material damage extends less than 0.2 mm in depth within the first E-glass ply. The transverse-direction results at 0.269, shown in Figure 4-14, indicate that similar to the fiber-direction stresses, the S22 stress is below the corresponding yield strength 0.2 mm below the surface and below.

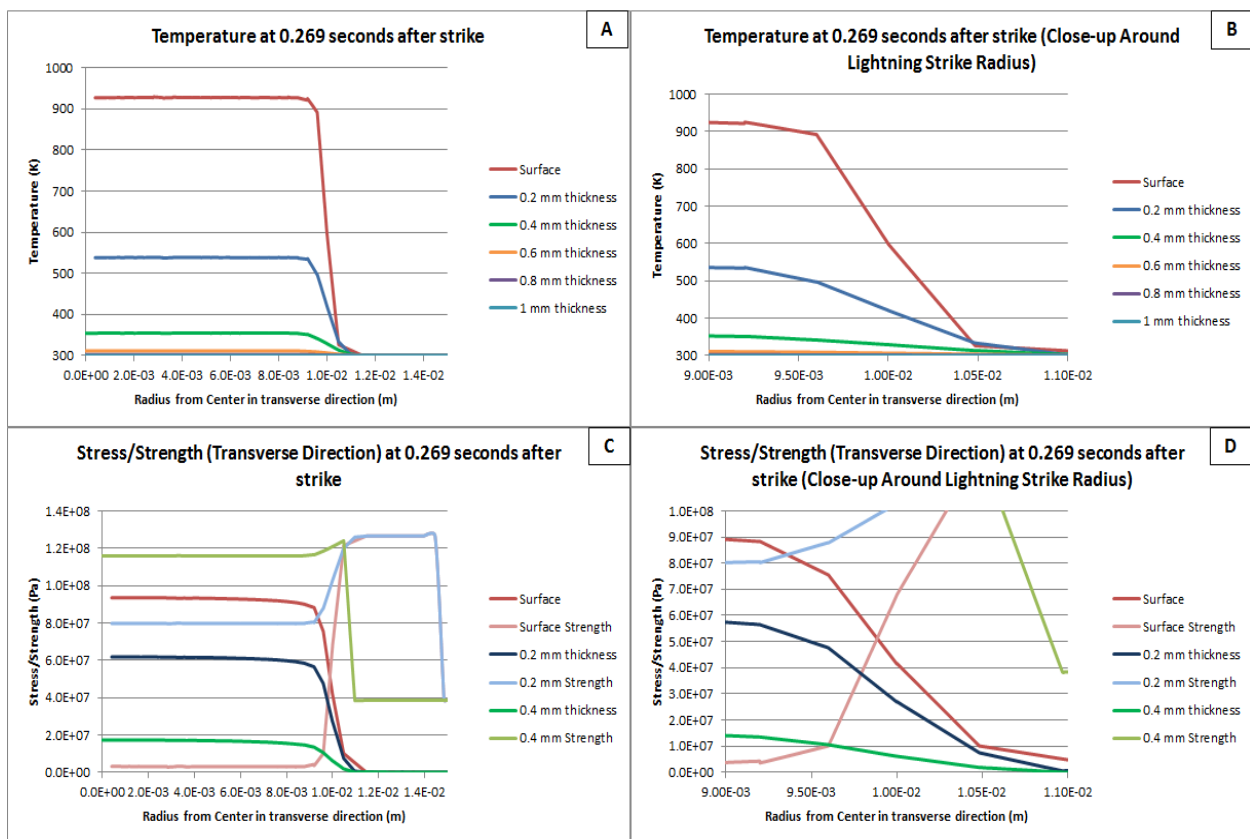


Figure 4-14: Temperature, stress, and composite strength distributions at different depths at 0.269 s after the strike in the transverse-direction

The decreases in material strength at 11 and 15 mm from the plate center result from switches from compressive to tensile stress. This does not alter the conclusion that the only depth level to undergo plastic yielding is the plate surface.

As expected, the plate surface cools as time passes. The temperature gradient and the corresponding fiber-direction stress strength gradients at 5 s after the lightning strike are presented in Figure 4-15.

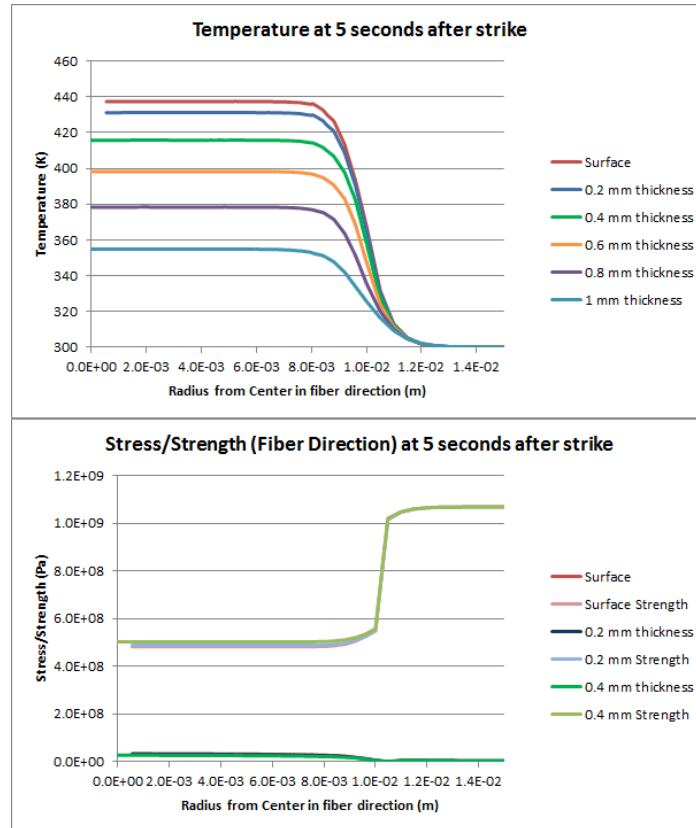


Figure 4-15: Temperature, stress, and yield strength in the fiber-direction 5 s after lightning strike

Lower depths increase in temperature as the surface heat diffuses through the ply thickness, but not enough to produce yield strengths lower than the thermal stresses. The same is true for stresses in the transverse-direction, shown in Figure 4-16.

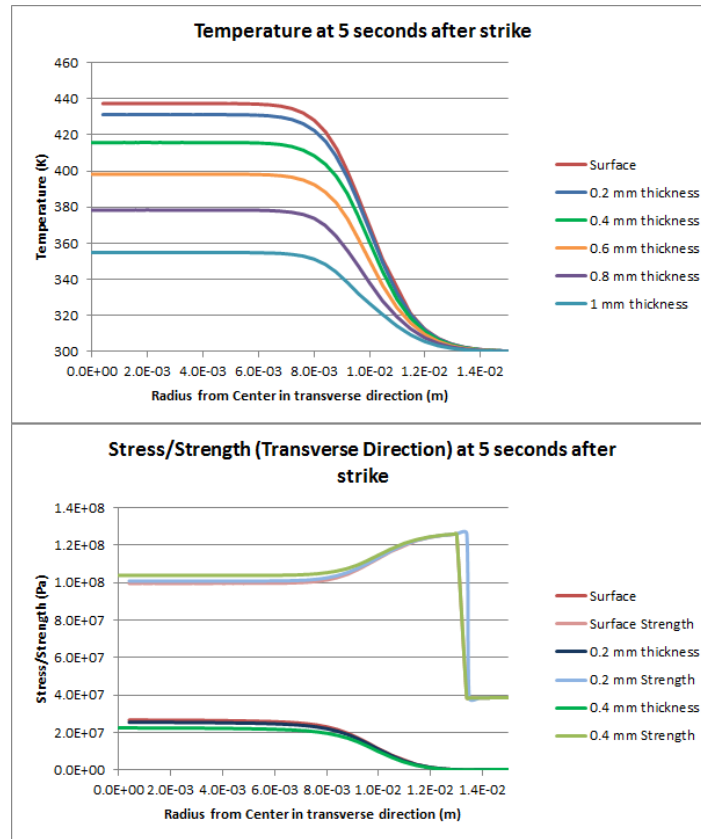


Figure 4-16: Temperature, stress, and yield strength in the transverse-direction 5 s after lightning strike

Due to the low thermal conductivity of E-glass composite, material damage due to plastic yielding is limited to less than 0.5 mm outside of the lightning strike zone in the radial-direction and less than 0.2 mm in the thickness-direction. The entire area of the strike zone at the plate surface undergoes plastic yielding.

Repeating the same investigation as with a direct lightning strike to composite material, the modeled strikes to a composite plate with a centered copper lightning receptor yield similar results in terms of the extent of composite material damage. As explained earlier in the chapter, a heat flux is applied to the lightning strike region (assigned copper material properties) on the surface of the plate, representing a lightning strike to a copper lightning protection receptor. A limit of 2720 K, nearly the vaporization temperature of copper, is placed, signifying that material exceeding this temperature is ablated, and material below this temperature remains in either solid or liquid form. A plot of temperature gradient as a function of radius from the center of the plate in the fiber-direction is given in Figure 4-17.

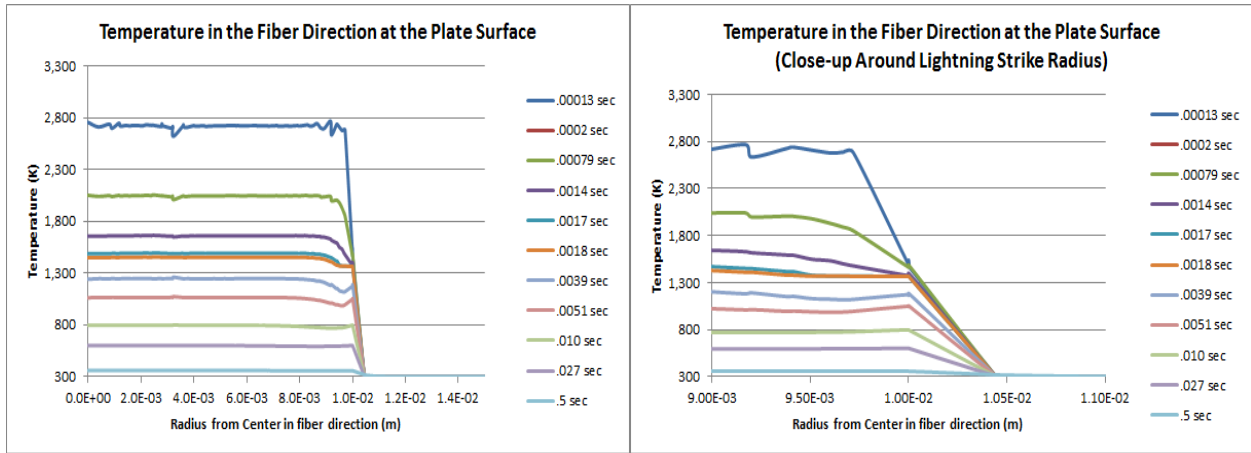


Figure 4-17: Temperature distribution at the plate surface for multiple time steps in the fiber-direction for a lightning strike to a copper receptor

As observed in simulations modeling direct strikes to composite material, the temperature outside the copper lightning strike zone rapidly decreases as the distance from the plate center increases as a result of the low thermal conductivity of E-glass material. Material 0.4 mm outside of the copper receptor remains at room temperature for all time steps. Figure 4-18 shows that the results are the same in the transverse-direction.

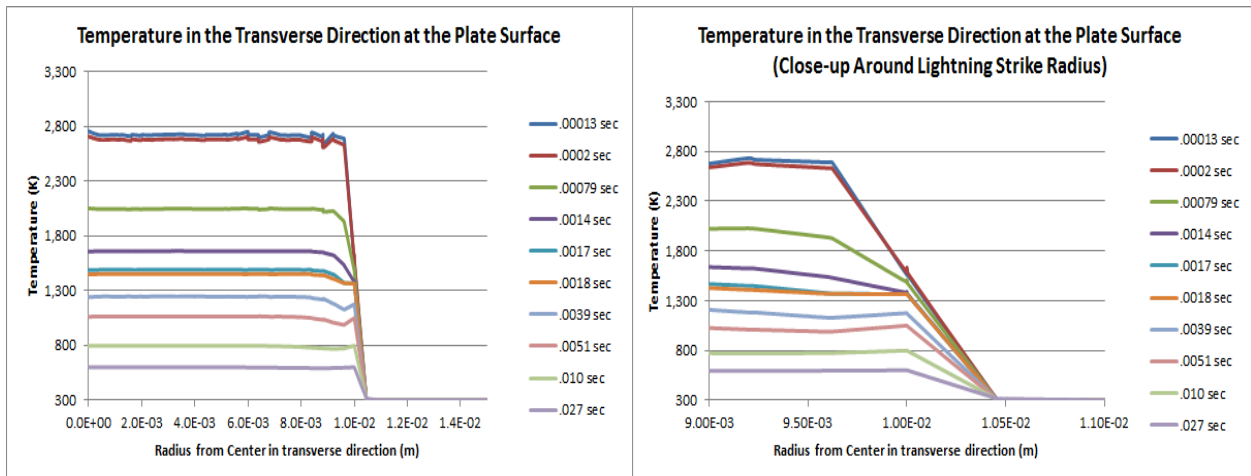


Figure 4-18: Temperature distribution at the plate surface for multiple time steps in the transverse-direction for a lightning strike to a copper receptor

At 0.005 s after the lightning strike, the farthest extent of damage is expected. Focusing on the plate surface, Figure 4-19 displays the thermal and stress gradients from the plate center in the fiber-direction.

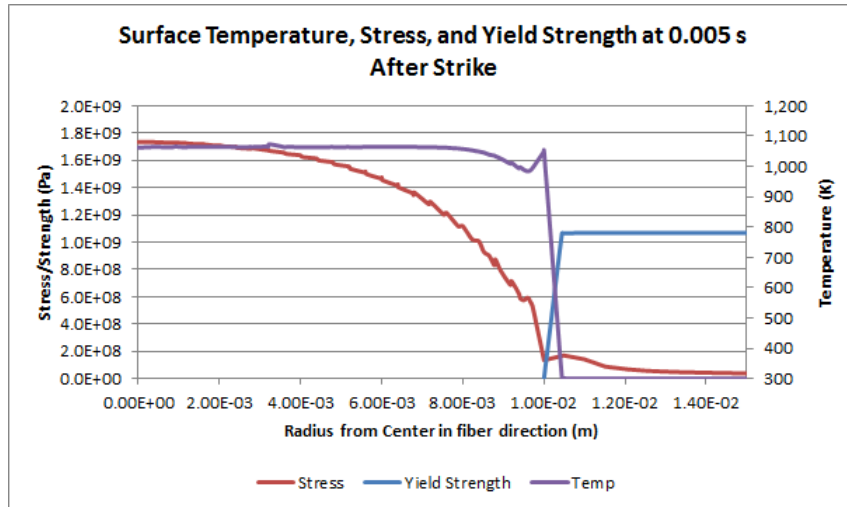


Figure 4-19: Fiber-direction temperature, stress, and strength gradients at 0.005 s after lightning strike

The important location to examine is the area immediately surrounding the copper lightning receptor. Plastic yielding of the copper is prevalent, but it isn't as important as determining the extent of E-glass composite damage because it does not exist to provide strength to the turbine blade, whereas damage to the composite material is detrimental to blade life. The plot shows that the first 0.4 mm outside of the copper receptor transition from zero material strength to the room temperature value of tensile strength, 1080 MPa. The material strength is greater than the S11 stress for almost all E-glass composite nodes. Plastic yielding occurs in less than 0.1 mm radially in the fiber-direction. The results are almost the same in the transverse-direction, in which plastic yielding occurs in less than 0.3 mm radially, shown in Figure 4-20.

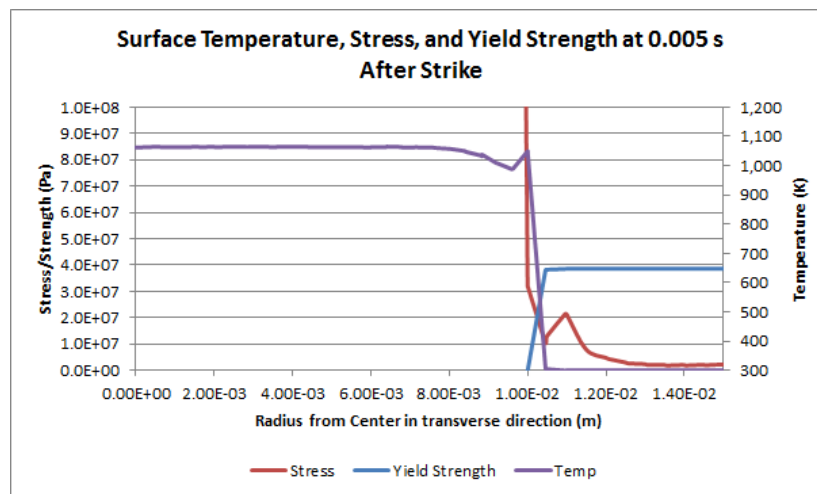


Figure 4-20: Transverse-direction temperature, stress, and strength gradients at 0.005 s after lightning strike

Despite the fact that material strength in the transverse-direction is much less than that in the fiber-direction, the thermal stresses within the E-glass composite material do not exceed material strength. Looking in the depth-direction of the material at 0.005 s after the lightning strike, it is clear that material deeper than 0.5 mm does not undergo plastic yielding. Figure 4-21 and Figure 4-22 show the fiber-direction and transverse-direction thermal and stress gradients at various depths below the plate surface.

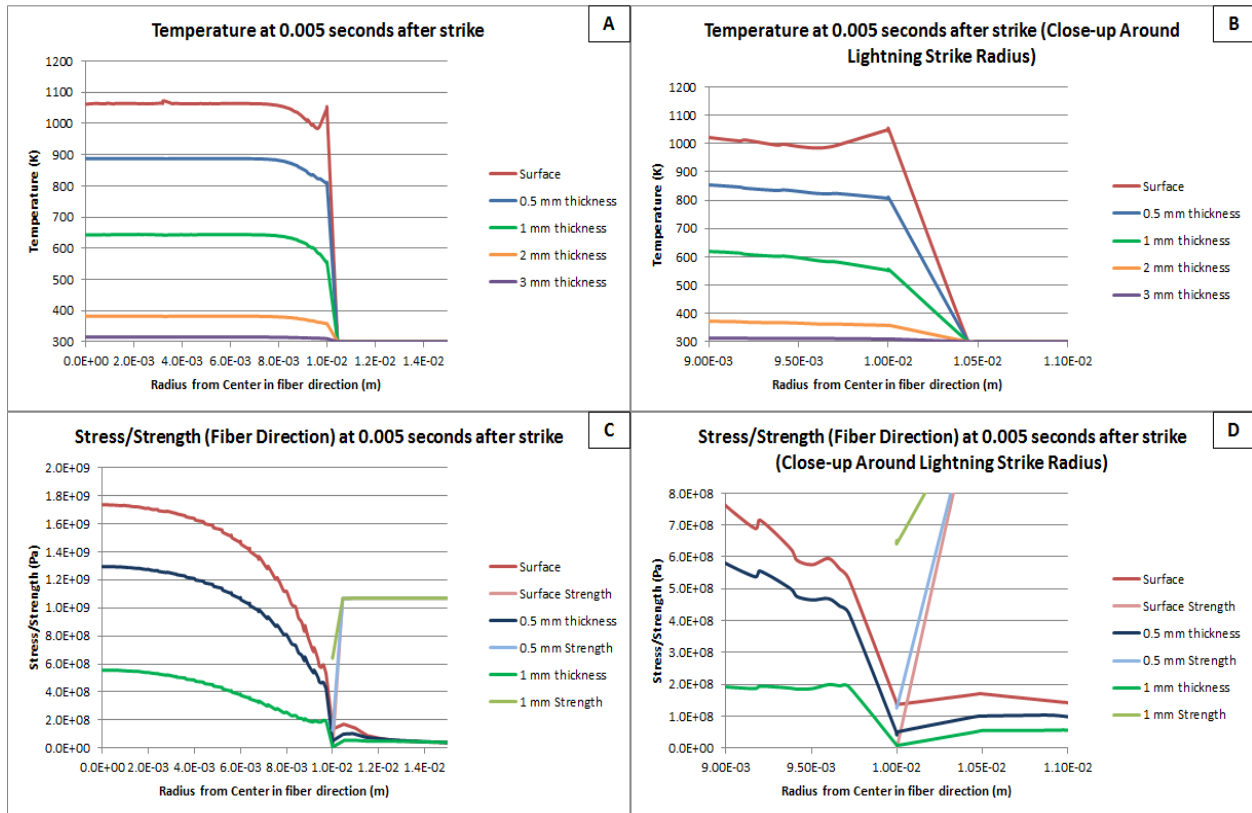


Figure 4-21: Fiber-direction temperature, stress, and strength plots at various depths within the plate

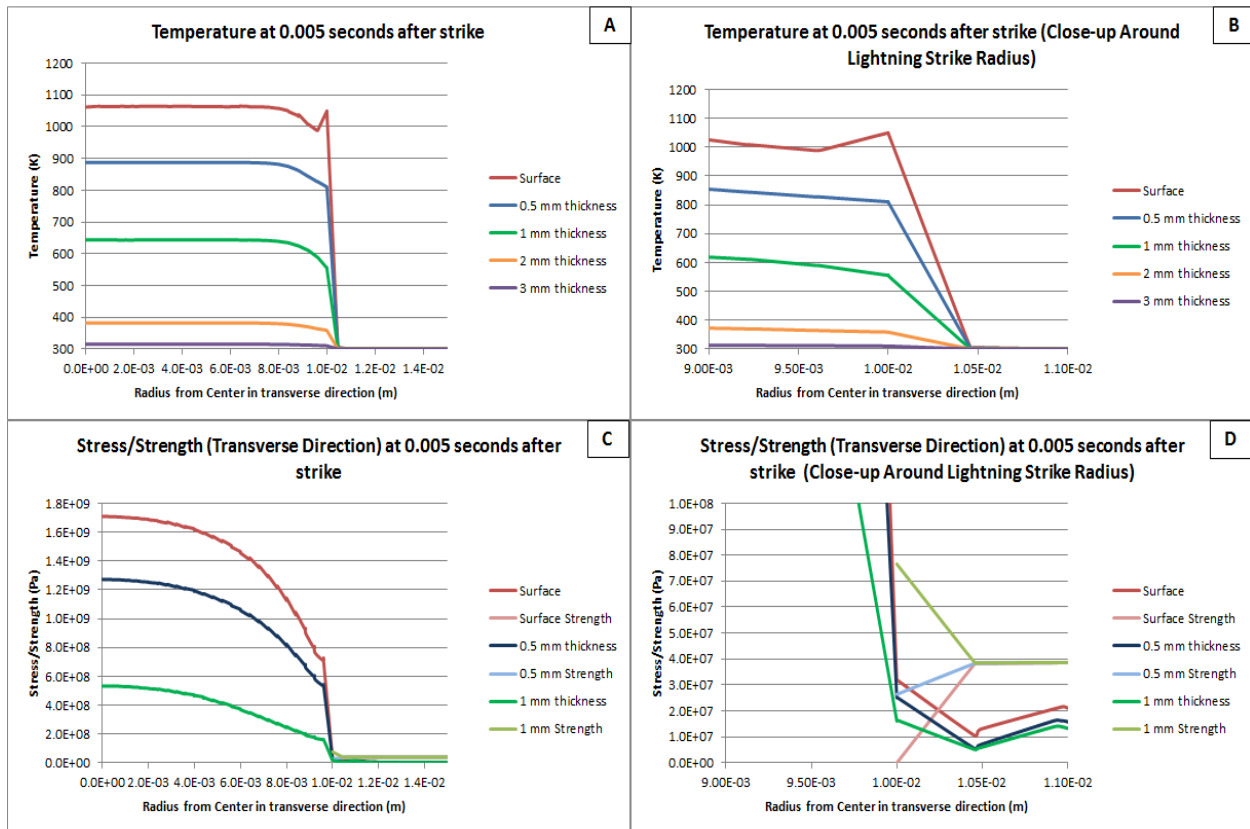


Figure 4-22: Transverse-direction temperature, stress, and strength plots at various depths within the plate

Plastic yielding is observed only at the plate surface in both the fiber and transverse-directions.

At a time step of 0.027 s after the lightning strike, sufficient time has passed so that the surface of the copper puck has cooled considerably, diffusing most of the initial heat in the thickness-direction due to the high thermal conductivity of the copper. However, the low thermal conductivity of the E-glass composites continues to prevent any significant amount of heat to diffuse into the composite, thereby keeping material strength high and thermal stresses low. Figure 4-23 and Figure 4-24 show that by 0.027 s after the lightning strike, no additional plastic yielding is present radially or in the depth-direction.

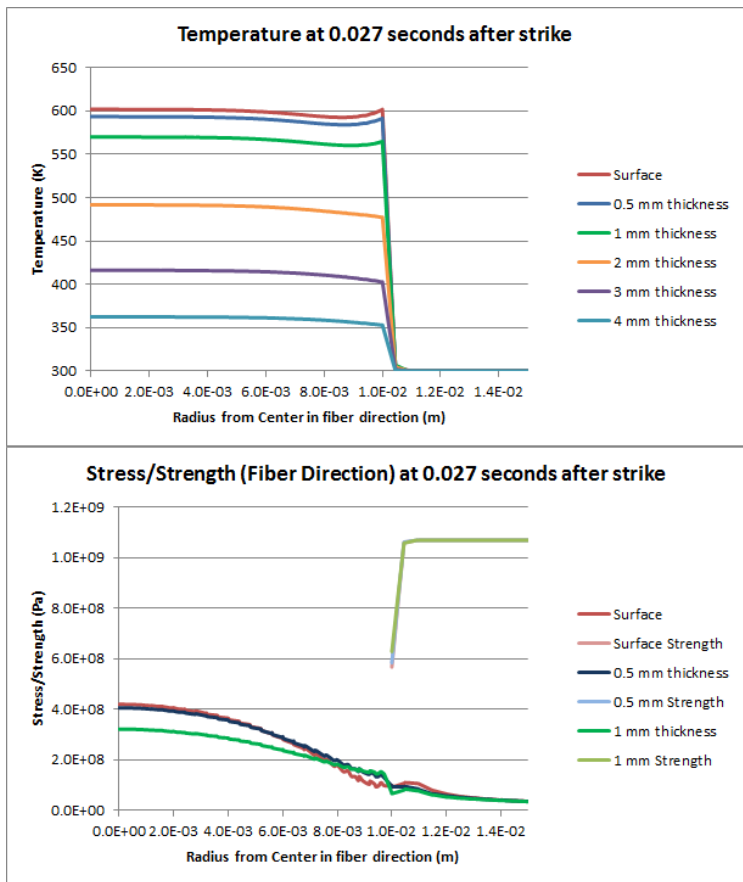


Figure 4-23: Fiber-direction temperature, stress, and strength 0.027 s after strike

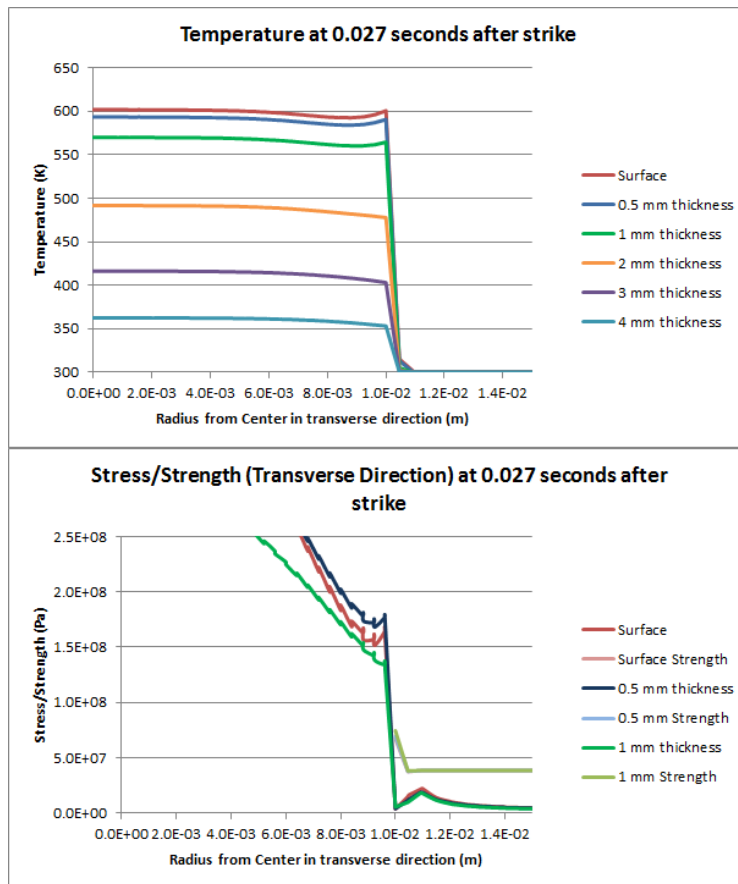


Figure 4-24: Transverse-direction temperature, stress, and strength 0.027 s after strike

Similar to direct lightning strikes to composite material, strikes to a central copper lightning receptor results in very little material damage due to yielding. Due to the low thermal conductivity of E-glass composite, material damage is limited to less than 0.3 mm outside of the lightning strike zone in the radial-direction and no damage is observed below the plate surface in the thickness-direction. The plots which compare material stress and yield strength show that the material damage is limited to the area immediately surrounding the lightning strike zone. However, the presence of plastically yielded material signifies that the damaged area now has a pre-stress, which causes negative performance effects in the blade. Additional stresses due to loading, internal pressure, or additional lightning strikes would result in an increase of damaged area, as the additional stress would build off of the pre-stressed, plastically deformed material. Since the stress results are non-linear, a superposition method of determining this additional stress is inadequate. It is recommended that future studies should research a modified superposition method to account for the damage accumulation. As explained earlier, analyzing

only the S11 and S22 stresses might not provide the most conservative yield information. Different loading cases must be analyzed in future studies in order to determine the worst-case yielding scenarios in terms of loading combinations.

5. How Damage Affects Blade Frequency Responses

5.1. Blade Condition Monitoring

Chapter 4 shows that material damage does indeed occur as a result of localized thermal stresses due to lightning strikes. Knowing that lightning causes damage to wind turbine blades, it is necessary to determine the ability to detect such damage before it becomes a repair concern. One of the biggest issues with wind turbines is the relatively high cost of operation and maintenance (OM). Most wind turbines are difficult to access, often located in remote areas, and require specialized equipment for repairs. The operations and part costs for turbines with over 20 years of operating life are estimated to be 10-15% of the total income for a wind farm. Despite the fact that larger turbines reduce the OM cost per unit power, the cost per failure is increased. The OM cost for a large offshore wind turbine is estimated to be 20-25% of the total income [40]. It is extremely important to monitor the condition of turbines to avoid greater damage and to therefore reduce unnecessary repair cost.

As wind turbines grew in size and power rating, most operators shifted from reactive maintenance to preventative maintenance. This required periodic inspections for condition assessment, which are generally expensive and require undesired scheduled down-time [40]. In addition, the periodic nature of these inspections proved to be disadvantageous as the equipment condition between checks was unknown. Predictive maintenance and condition-based maintenance have become increasingly more popular with the help of condition monitoring and fault diagnostic techniques [40]. The objective of condition monitoring systems is to autonomously detect early warnings of mechanical and electrical defects to prevent major component failures [41]. The advantages of such systems include the avoidance of premature breakdown, reduction in maintenance costs, and supervision at remote sites where inspection is difficult. Monitoring the condition of the rotor is especially important because it provides information about potential failure and allows time to arrange maintenance logistics.

Turbine blades can develop cracks and delaminations due to erosion, icing, creep, and lightning strikes. As mentioned in Chapter 2, it is possible for a lightning strike to cause a rapid expansion of air within the turbine blade, which could result in a high-pressure shock wave inside the blade. This high internal force sometimes causes delamination at the adhesive joints in the trailing edges and at the interface of the spar cap and shear web, which are generally the weakest points in the blade. Table 5-1 is a list of common types of damage to wind turbine blades; an accompanying sketch of the damage types is available in Figure 5-1.

Table 5-1: Typical damage of wind turbine blades [42]

Type	Description
Type 1	Damage formation and growth in the adhesive layer joining skin and main spar flanges (skin/adhesive debonding and/or main spar/adhesive layer debonding)
Type 2	Damage formation and growth in the adhesive layer joining the up- and downwind skins along leading and/or trailing edges (adhesive joint failure between skins)
Type 3	Damage formation and growth at the interface between face and core in sandwich panels in skins and main spar web (sandwich panel face/core debonding)
Type 4	Internal damage formation and growth in laminates in skin and/or main spar flanges, under a tensile or compression load (delamination driven by a tensional or a buckling load)
Type 5	Splitting and fracture of separate fibers in laminates of the skin and main spar (fiber failure in tension; laminate failure in compression)
Type 6	Buckling of the skin due to damage formation and growth in the bond between skin and main spar under compressive load (skin/adhesive debonding induced by buckling, a specific type 1 case)
Type 7	Formation and growth of cracks in the gel-coat; debonding of the gel-coat from the skin (gel-coat cracking and gel-coat/skin debonding)

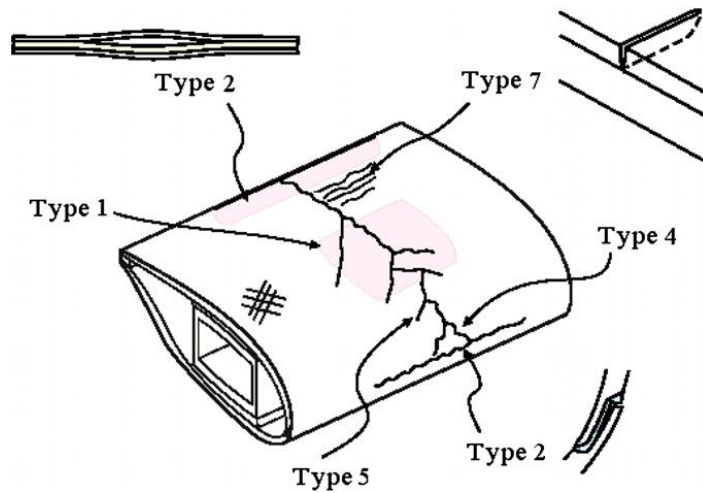


Figure 5-1: Sketch of a wind turbine blade segment illustrating some of the common damage types [42]

Various damage types were created in a laboratory test and are shown in Figure 5-2 and Figure 5-3.

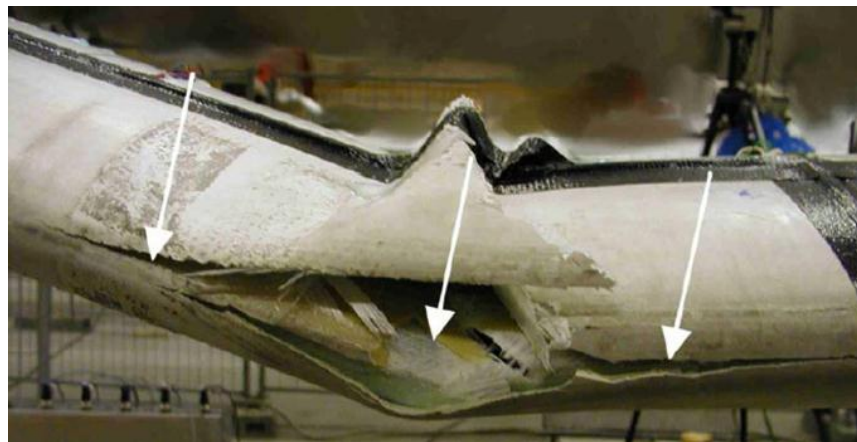


Figure 5-2: Damage type 2 (adhesive joint failure between skins) at the leading edge [42]

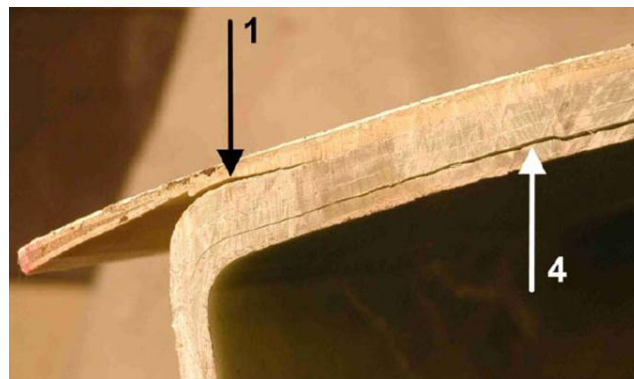


Figure 5-3: Damage type 1 (main spar flange/adhesive layer debonding) and type 4 (delamination by buckling load) [42]

Modal-based methods are among the most common damage detection methods utilized due to the fact that they are relatively simple to implement on any size structure [42]. Blades can be excited by ambient energy, an external shaker, or embedded actuators while the dynamic response can be monitored by embedded strain gauges, piezoceramics, or accelerometers. The concept is that modal frequencies are functions of the physical properties of the blade (mass, damping, and stiffness). Changes in the physical properties, such as cracks or delaminations, will produce detectable changes in the modal frequencies [42]. Any variation in frequency in the blade compared to the “pre-damage” control state is an indicator of damage. One detection option is to place piezoceramic patches at hot spots (an optimal placement of a sensor at which reliable damage data can be acquired) along the blade to compare resonant frequency changes. Ambient excitation is appealing since it allows for modal analysis to be performed under service conditions [42].

Regardless of how the frequency variation is measured, any sensor system has finite resolution accuracy. Frequency variation below this minimum detectable limit cannot be differentiated from background noise. Small cracks that alter the blade frequencies below this resolution accuracy are therefore invisible to damage detection methods that require frequency variation readings. It is important to determine the damage size detection limit because small cracks can quickly propagate if they are not addressed when they occur.

5.2. Wind Turbine Blade Design

Abaqus-CAE Version 6.11-2 is used to model a wind turbine blade. The blade profile and design are based off an average 1.5 MW wind turbine using a common E-glass composite skin material. The geometry of the blade is based on a combination of a 38 meter blade designed by Michael Edon in 2007 and the advice of Shu Ching Quek, an engineer in the wind industry [43], [44]. The airfoil shape is based on a NACA 64(3)-618 standard profile, which is similar to Edon’s FX66-S196-V1 geometry. The blade is sized as a typical industry turbine blade, specifically a 38 meter blade with a 4 meter chord at the base of the blade.

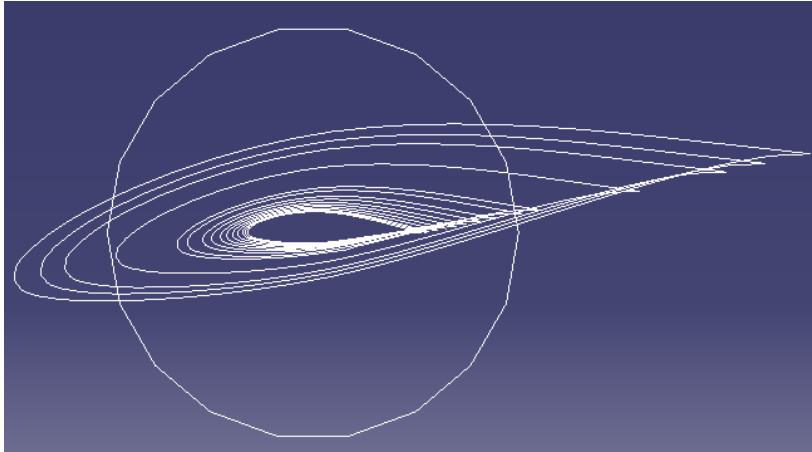


Figure 5-4: NACA 64(3)-618 Standard Airfoil, viewed from blade root in Abaqus-CAE

The airfoil geometry was provided as a set of two-dimensional points with a normalized chord length, provided in Appendix D.1 [45]. In order to match Edon's blade geometry, the widest airfoil chord occurs at a blade radius of 4.75 m, measuring 3.92 m in length from the leading edge to the trailing edge [43]. The blade hub is assumed to be a perfect circle, shifting gradually to a NACA 64(3)-618 airfoil with an angle of attack of 9 degrees, which is a typical value in the industry. By using chord lengths provided in Edon's report at specific blade radii and interpolating at intermediary points (to increase geometry accuracy in Abaqus), the blade geometry is defined and provided in Table 5-2. Angle of attack at each blade radius is also included.

Table 5-2: Blade Geometry [43]

Radius	Chord Length	Source	Angle of Attack
4.75	3.92	root	9.0
6	3.57	interpolation	8.7
7.13	3.25	provided	8.4
11.5	2.57	interpolation	7.2
16.63	1.77	provided	5.8
18.5	1.64	interpolation	5.3
21.38	1.43	provided	4.5
23.75	1.32	interpolation	3.9
26.13	1.20	provided	3.2
28.5	1.12	interpolation	2.6
30.88	1.04	provided	1.9
33.25	0.98	interpolation	1.3
35.63	0.91	provided	0.6
36.75	0.88	interpolation	0.3
38	0.85	tip	0.0

With the chord lengths and angles of attack at each blade radius, the two-dimensional airfoil points can be determined for a NACA 64(3)-618 airfoil profile. The calculation of two-dimensional points requires the definition of the shear web location, because the angle of attack is rotated about this location. The shear web is located at the shear center of the blade, which is between the center of mass and the aerodynamic center. In order to simplify calculations, it is acceptable to assume that this location occurs at 37.5% of the chord [44]. Appendix D.1 shows the calculations for determining the two-dimensional airfoil points for an example blade radius. These points are then input into Abaqus as nodes at each of the 15 blade radii using a recorded macro and the two-dimensional points calculated in Appendix D.1 (and similar points calculated at each blade radius). The Abaqus input code is provided in Appendix D.2. Figure 5-5 shows

the two-dimensional airfoil nodes at a blade radius of 4.75 m. Since the blade root is set at $z=0$, this signifies that a plane for a blade radius of 4.75 m occurs at $z=-4.75$.

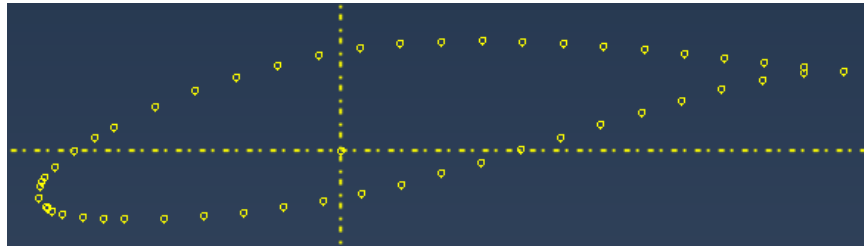


Figure 5-5: Uploaded airfoil nodes at a blade radius of 4.75 m

Once the nodes of the airfoils at each specified blade radius are uploaded into Abaqus, the basic outline of the turbine blade is then connected. This is achieved by use of the spline function in Abaqus CAE. The spline allows for a smooth wire transition between nodes. The airfoil outlines for each of the designated blade planes are shown in Figure 5-1. Once the spline wires for each airfoil is created, the outline for the 76 mm thick shear web is then designed. The shear web is parallel to the y-axis, which is normal to the chord-axis of the tip of the blade (the x-axis in this model). An example two-dimensional outline of the blade at the 4.75 meter plane, including the 76 mm thick shear web, is shown in Figure 5-6.

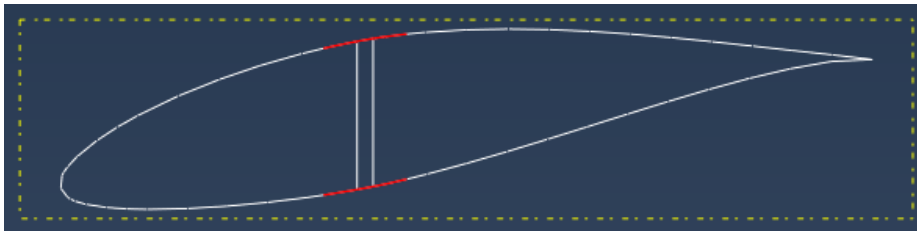


Figure 5-6: Wire outline of the blade airfoil at the 4.75 m plane

The wireframe outline is designed for the airfoils at each of the 15 blade planes. The spline of each airfoil is partitioned such that it allows for differentiation between the spar caps and the regular blade shell. The spar caps are designed to be 0.4 m wide (0.2 m on either side of the shear web). The spar caps are highlighted in red in Figure 5-6. The partition makes it easier to differentiate between spar caps and regular blade skin when assigning material properties.

Once completed, all of the airfoil outlines (as well as the blade root outline, a circle centered at the origin in Abaqus) are connected with the loft function. The loft function behaves

in a similar manner to the spline function in that it creates a smooth outline between two features. The difference is that a loft creates a three-dimensional feature rather than one that is two-dimensional. The outline of the blade is lofted as a shell, whereas the shear web is lofted as a solid to allow for multiple nodal connections along the top and bottom of the web. Figure 5-7 shows the fully-lofted wind turbine blade, including a close-up view of the root of the blade.

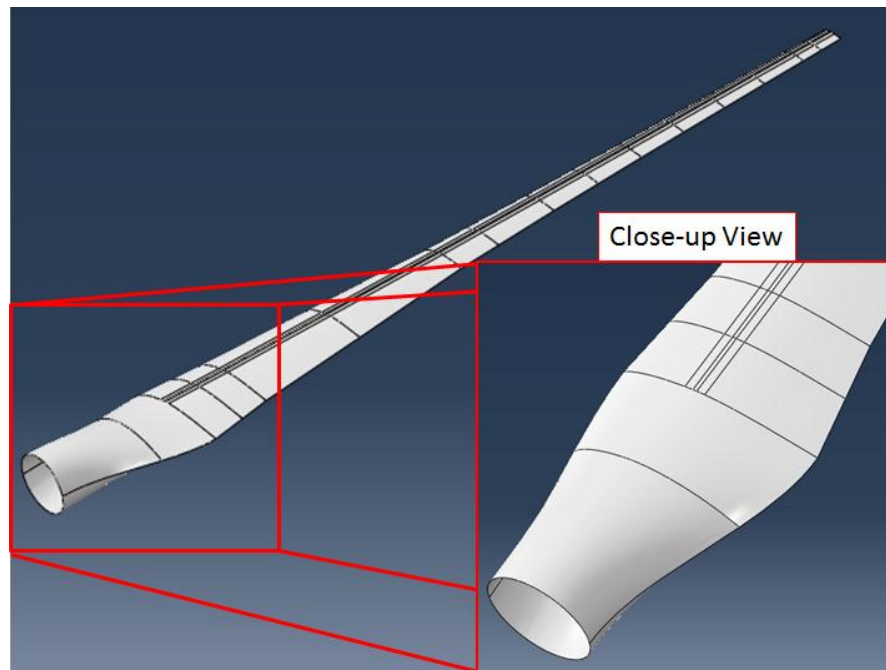


Figure 5-7: Lofted turbine blade

The close-up view shows the partitioned shell, differentiating the spar cap from the regular blade skin. The shear web and spar caps begin 4.75 m away from the blade root, at the widest chord, and the shear web ends 1.25 m from the blade tip. The spar caps continue through to the blade tip, but with diminishing thickness, which is controlled when assigning material properties. Figure 5-8 displays the solid shear web within the blade shell, viewed from the root of the blade.

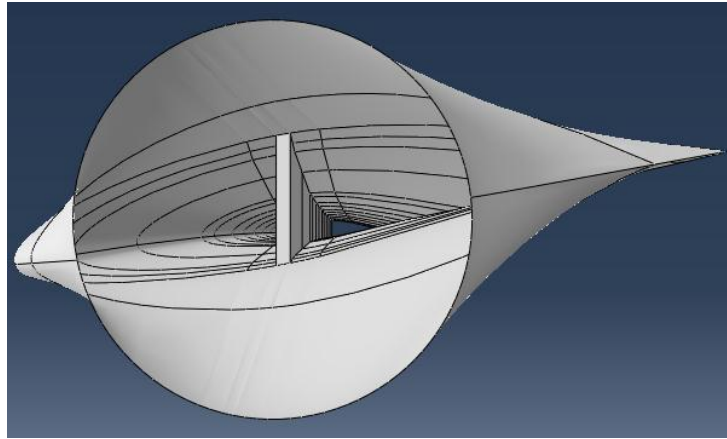


Figure 5-8: Lofted turbine blade viewed from the blade root

The material designation utilizes the same properties for E-glass composite, T300 carbon composite, and PVC foam as described in Chapter 3, but shell thickness and composite layup depends on blade component and location. The entire shear web consists of three 5-ply ($\pm 45, 0$) layups of E-glass composite material sandwiching a homogeneous foam core. Abaqus allows for composite layup definitions for solid as well as shell features. The PVC foam core, which is 46 mm thick, and the 30 E-glass plies, each 1 mm thick, must be entered in as an element relative thickness since the layup is being applied to a solid feature. Each ply is assigned material properties (E-glass composite or PVC foam, defined in Chapter 3), an element relative thickness (0.0132 for each E-glass ply and 0.6053 for the foam), an orientation angle (45, -45, or 0 for the biaxial E-glass plies and 0 for the foam, since directionality does not matter), and number of integration points (left at the default of 3). The solid shear web layup is provided in Appendix D.3.

The blade shell is partitioned to allow for a wide range of ply thicknesses. This is important, because real wind turbine blade thicknesses taper along the blade length. Creating partitions and setting different ply thicknesses for each segment allows for a coarse tapering of the blade. The thicknesses at each of the partitions therefore don't match up perfectly, but the small deviation from what is found in the field is considered to be negligible as far as analysis is concerned. A future detailed continuation of the analysis can account for the coarse tapering of the blade. Figure 5-9 shows the segments of the blade where shell thickness tapering occurs versus the segments where it does not occur.

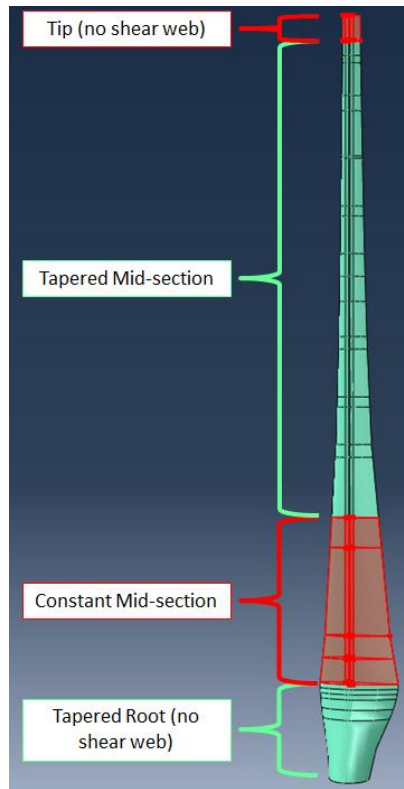


Figure 5-9: Blade breakdown between tapered and constant segments

The blade root does not have a shear web and consists entirely of biaxial E-glass composite material up until the widest airfoil chord, at 4.75 m blade length. It tapers in shell thickness from 80 E-glass composite plies (each 1 mm thick) in the form of 16 5-ply ($\pm 45,0$) layups down to 50 plies, as 10 5-ply ($\pm 45,0$) layups. The tapering calculations are provided in Appendix D.3. The tip of the blade (the last 1.25 m) also does not have a shear web. It is only 10 plies thick in the form of two 5-ply ($\pm 45,0$) layups of E-glass composite.

The remaining portion of the blade includes a shear web and spar caps, which are partitioned in order to allow for a different layup definition from the rest of the blade shell. The spar cap and the regular blade shell share the same thickness, but while the regular blade shell consists of two 5-ply ($\pm 45,0$) layups of E-glass composite material sandwiching PVC foam core, the spar caps have the exact same E-glass skin layup sandwiching an equally thick core of unidirectional T300 carbon composite material. In the constant section of the blade that does not taper (shown in red in Figure 5-9), the thickness of this “core material” is 38 mm. However, starting at 1/3 the blade length from the root (at a blade length of about 13 m), the core thickness

decreases in thickness, tapering to nothing at the blade tip (the final 1.25 m of the blade). The details of this gradual tapering of core material are provided in Appendix D.3. An example of one of the shell material layup definitions is also included in the appendix.

The directional material properties require an axial definition of the blade shell and solid shear web. The definition of the material orientation input in Abaqus is important to note (except for PVC foam, which is assumed to be homogeneous). For the layup definitions an orientation angle of 0 means that the 1-direction of the material (the fiber-direction for E-glass composite and carbon composite in this case) is the same direction as defined on the feature. An orientation angle of +45 or -45 degrees means that the 1-direction of the material is offset +45 degrees or -45 degrees from the 1-direction defined on the feature, respectively. The material orientation of the shear web is defined in Abaqus such that the 1-direction is along the blade length, the 2-direction is along the airfoil height, and the 3-direction is along the airfoil chord. The blade shell material orientation definition is more complicated given the geometry of the blade and is shown in Figure 5-10.

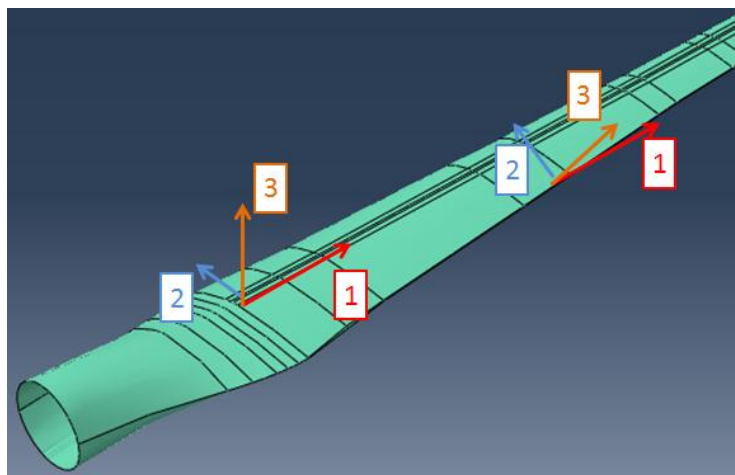


Figure 5-10: Material orientation definition for blade shell

The 1-direction of the material orientation is defined to be along the blade length (ensuring that the fiber-direction, the strongest direction of carbon composite, provides strength along the blade). The 2-direction is tangent to the surface of the blade in the airfoil chord-direction and the 3-direction (the thickness-direction) is normal to the surface of the blade in the airfoil height-direction.

The goal of this analysis is to determine the extent of natural frequency shift caused by increasingly larger cracks at various locations in the blade. As such, Abaqus is used to run a frequency analysis for the first ten eigenvalues of the blade. The only boundary condition is shown in Figure 5-11 in which the circumference of the blade root is set to “encastre,” to ensure that displacement and rotation are prohibited. This represents a wind turbine blade in operation; the blade root is bolted firmly to the hub to prevent rotation and displacement relative to the hub.

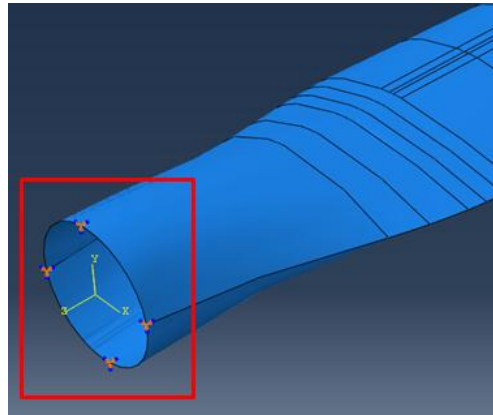


Figure 5-11: Boundary condition prevents rotation and displacement at the root

The mode shape images for each of the first ten modes are provided in Appendix D.4, and an example input file is provided in Appendix D.5. The natural frequencies for the first ten modes of the baseline blade are provided in Table 5-3.

Table 5-3: Natural Frequencies for First Ten Modes of Baseline Turbine Blade

Mode	Eigenfrequency [Hz]	Mode Shape
1	0.275	Flap-1
2	0.938	Edge-2
3	1.045	Edge-2
4	2.257	Flap-2
5	3.563	Edge-3
6	4.118	Flap-3
7	6.514	Flap-4
8	7.962	Edge-4
9	9.161	Torsion-1
10	9.366	Flap-5

Cracks are simulated in the model at various locations along the blade and are varied in length. This data is used to determine the frequency variation from the baseline values. Seams are created by first partitioning off the intended length of each crack. The seam is then assigned by selecting the partitioned line segment in the part feature within the “interactions” module. Assigning a seam creates double nodes at the exact same points when meshed, allowing the feature to “unzip” during analysis. The nodes along the assigned seam are not attached to each other, representing a crack that varies in length, dependent on the length of the feature partition. Two types of cracks are investigated: splits in the trailing edges and splits between the spar cap and shear web. These locations are generally the weakest parts of the blade construction due to the fact that lamination material makes up a large portion of the connections. The lengths of the detachments that are tested are provided in Table 5-4. The seam lengths are provided as a percentage of the blade between the widest chord and the blade tip rather than the entire blade length based on the assumption that cracks rarely develop between the blade root and the widest chord. The blade length is 38 m, but the length between the widest chord and the tip is only 33.25 m, and all percentages are based on that value.

Table 5-4: Variation in Crack Length Assigned to Blade

Crack Length [m]	Percent of Blade Length (Widest Chord to Tip)
0.0254	~1 inch
0.665	2%
1.33	4%
1.995	6%
2.66	8%
3.325	10%
6.65	20%

The study takes three locations along the blade into account: cracks that initiate at the blade tip, cracks that initiate near the root, at the widest airfoil chord, and cracks that initiate near the middle of the blade, halfway between the widest airfoil and the blade tip. Figure 5-12 shows the location of the seam assignment for cracks that initiate at the trailing edge of the tip of the blade.

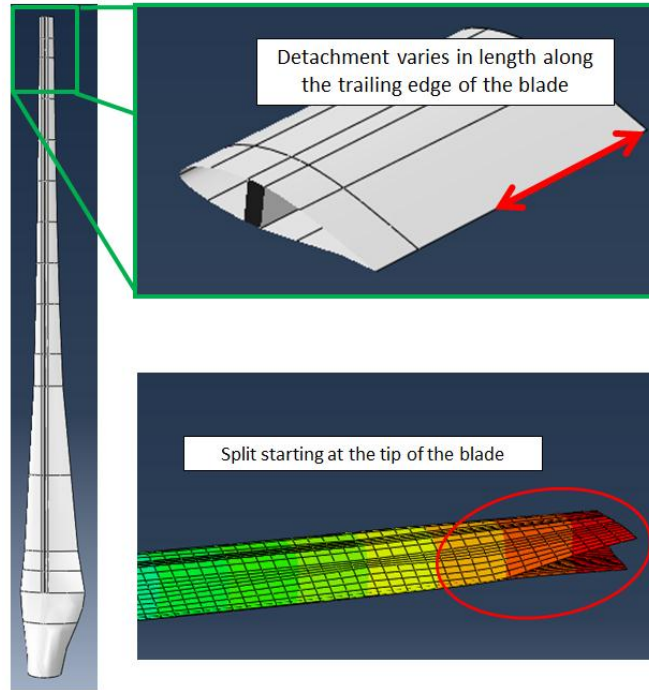


Figure 5-12: Crack propagation along the trailing edge at the blade tip

The crack initiates at the tip of the blade and runs the length of the blade, varying in length according to Table 5-4. The first seam in the study runs from the blade tip, down 0.0254 m toward the blade root. The second seam analyzed is 0.665 m, and so on. Figure 5-13 shows the initiation site of a crack at the middle of the blade at the trailing edge of the airfoil.

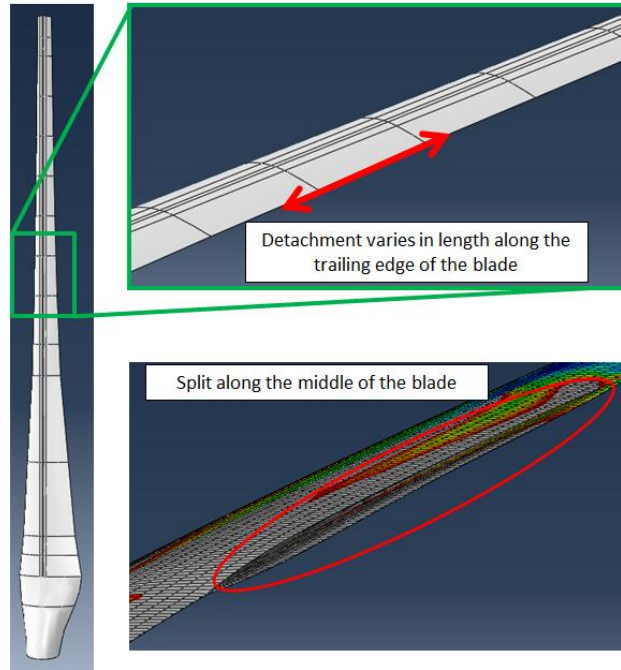


Figure 5-13: Crack propagation along the trailing edge at the middle of the blade

The final location for detachment along the trailing edge is the widest airfoil chord near the blade root, shown in Figure 5-14.

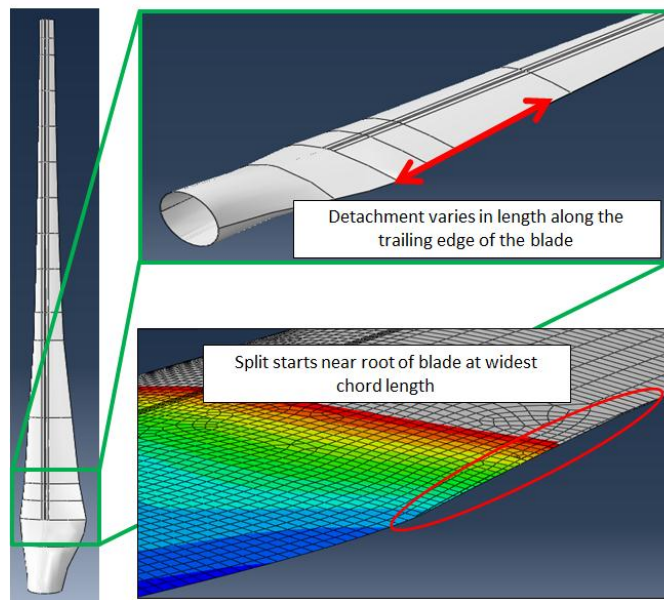


Figure 5-14: Crack propagation along the trailing edge at the widest chord near the root of the blade

Cracks that initiate between the spar cap and the shear web occur at the same locations along the blade: at the start of the shear web near the blade tip, at the widest chord, and halfway between

the widest chord and the tip. Figure 5-15 shows an example of a crack location at the tip of the blade.

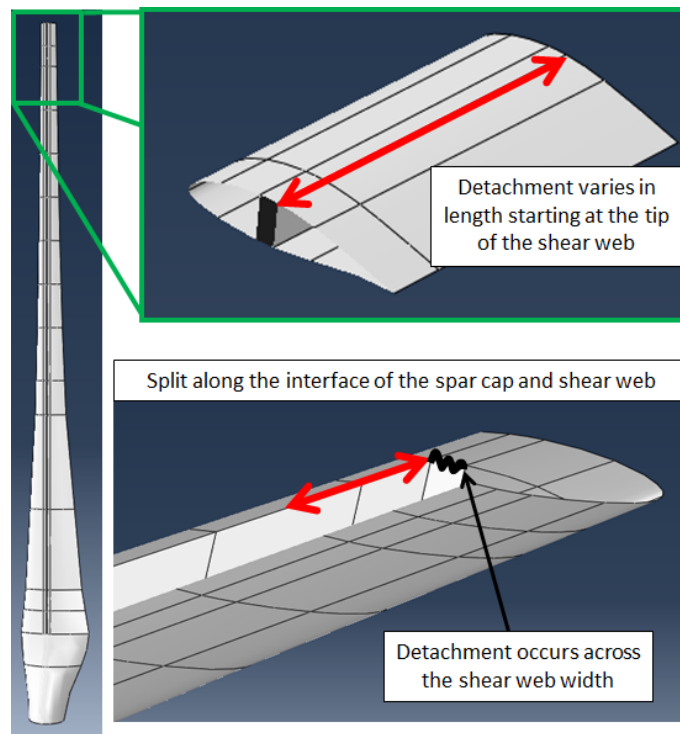


Figure 5-15: Crack propagation across the shear web near the tip of the blade

Appendix D.5 shows an example Abaqus input file used during the analysis of a blade with an assigned seam.

5.3. Blade Damage Results

Using the wind turbine blade model described in the previous section as a baseline, Abaqus natural frequency analysis results reveal the percent frequency change for the first ten modes as varying crack lengths are input at key locations in the blade. The resulting frequency change as a function of crack length is calculated, shown in Appendix D.6, for each location within the blade.

Cracks along the trailing edge of the blade tend to produce the greatest frequency change from the baseline, especially for flap and torsion modes. Figure 5-16 shows the natural

frequency difference from the baseline values for cracks along the trailing edge at the tip of the blade.

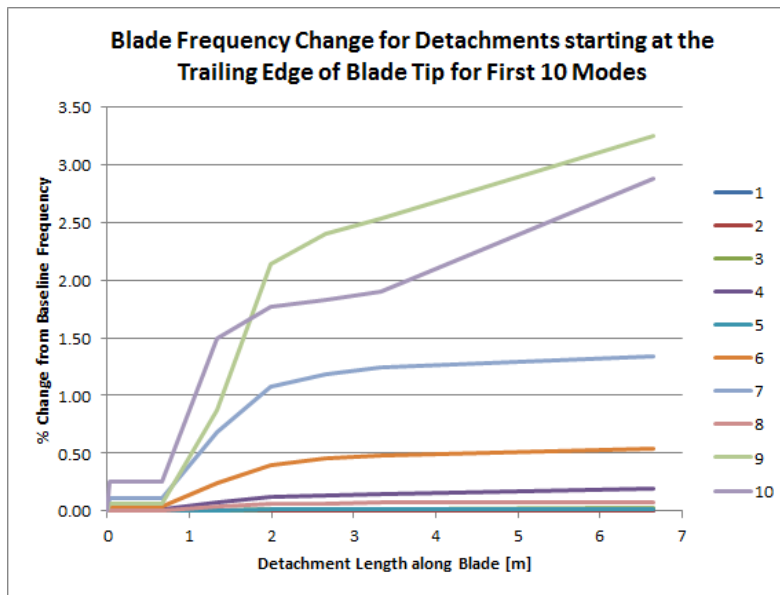


Figure 5-16: Natural frequency difference for first 10 modes at trailing edge of blade tip

The four modes that produce the greatest difference in natural frequency from the baseline model are 6, 7, 9, and 10, which correspond to the third flap, fourth flap, first torsion, and fifth flap mode shapes, respectively. It is evident that even a 0.5% change in natural frequency would be detected for cracks less than one meter for a sensing system capable of tracking modes 7, 9 and 10. Longer cracks will give rise to greater changes in natural frequency. However, systems that are not robust enough to track modes 6 or higher would not be able to detect cracks greater than 6 m in length, over 10% of the blade length, unless extremely sensitive sensing equipment is utilized. Figure 5-17 presents the difference in natural frequency for crack seams at the trailing edge of the middle of the blade, between the blade tip and the widest chord.

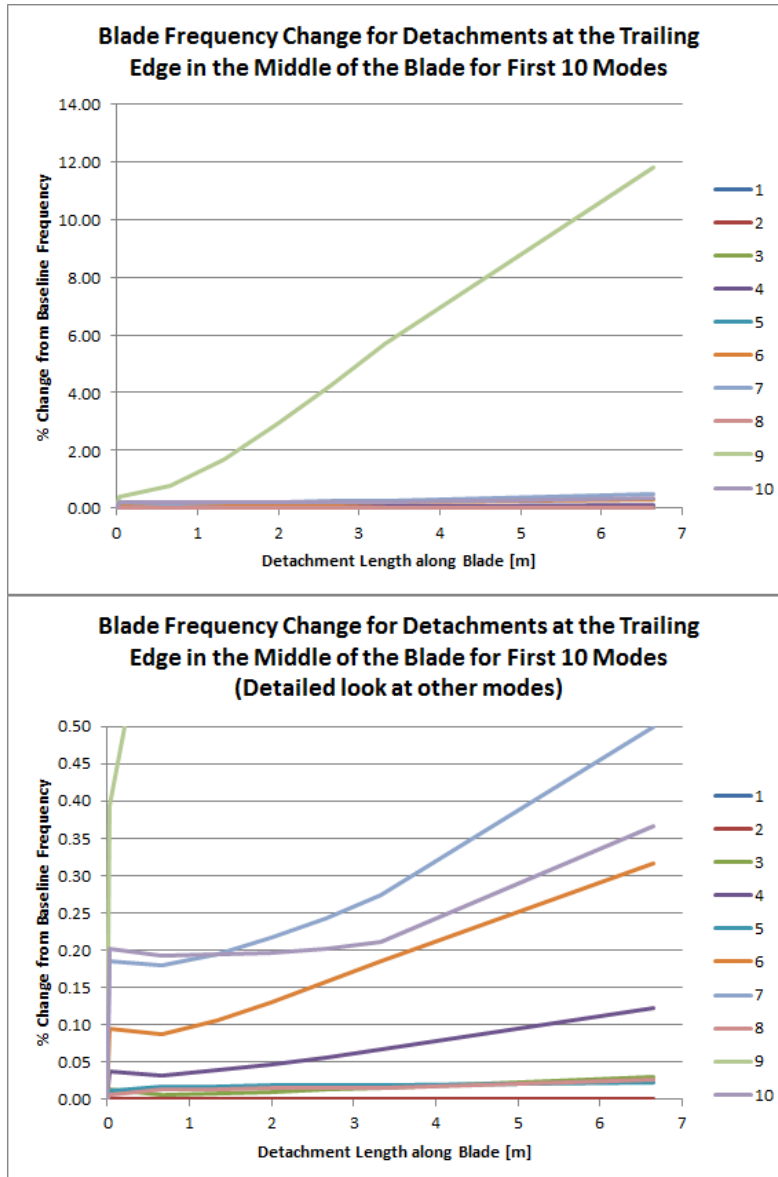


Figure 5-17: Natural frequency difference for first 10 modes at trailing edge of blade mid-length

It is clear that the first torsion mode frequency change is easily detected for very small cracks at the trailing edge mid-blade. However, the detailed view shows that measurement equipment must be sensitive enough to detect a 0.2% frequency change if this torsion mode is not accounted for. The Abaqus results show that small cracks initiating at the widest airfoil chord of the blade are most likely neglected unless the sensing equipment is capable of detecting a 0.1% change in natural frequency. Figure 5-18 illustrates that cracks larger than two m produce substantial changes in the blade natural frequency for the torsion mode and most of the flap modes, but cracks smaller than one meter require extremely sensitive equipment in order to be identified.

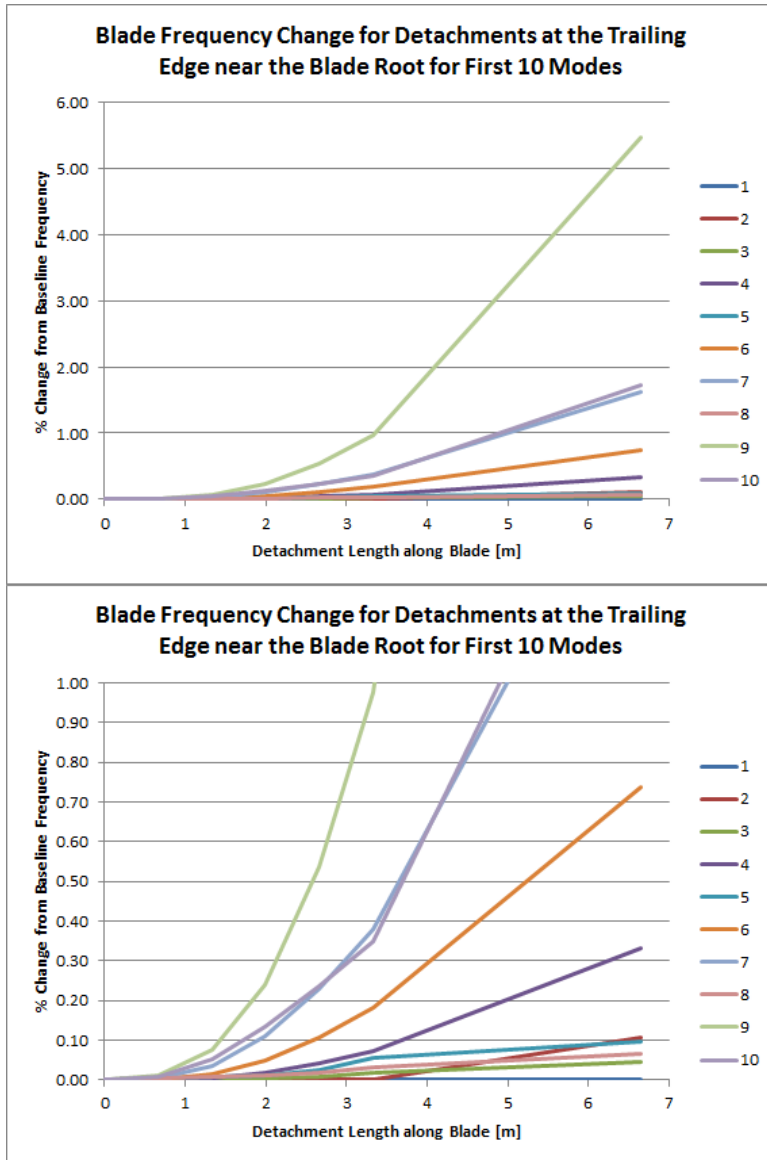


Figure 5-18: Natural frequency difference for first 10 modes at trailing edge of blade at the widest chord

While it is possible for sensing systems to readily detect cracks at the trailing edge of the blade, provided they are able to measure higher mode frequencies, it is much more difficult to detect natural frequency differences for cracks that initiate between the shear web and the spar cap. In Figure 5-19, it is obvious that precise measurements are necessary to discover small cracks near the blade tip.

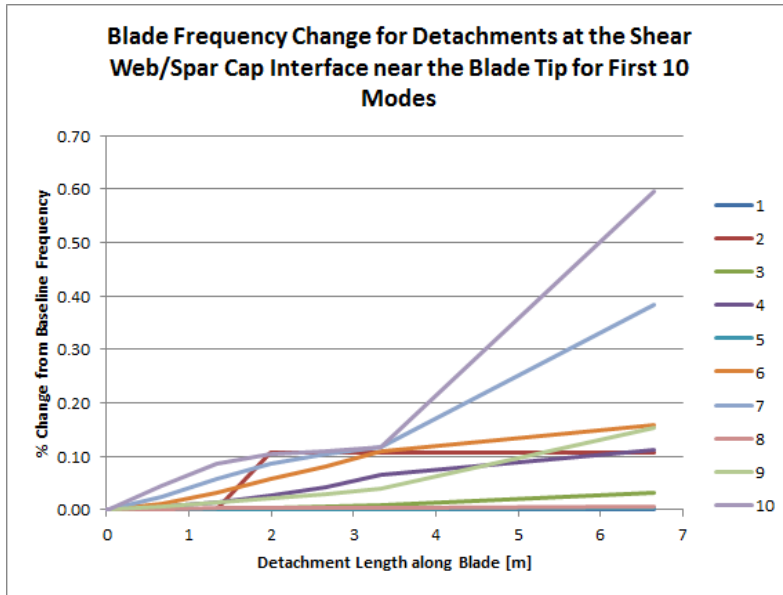


Figure 5-19: Natural frequency difference for first 10 modes at shear web/spar cap interface near blade tip

A 0.2% change in natural frequency will not be identified unless the split is almost four m in length. Figure 5-20 shows that cracks at the interface between the spar cap and shear web, near the mid-point of the blade length, result in natural frequency differences almost as small as cracks near the tip.

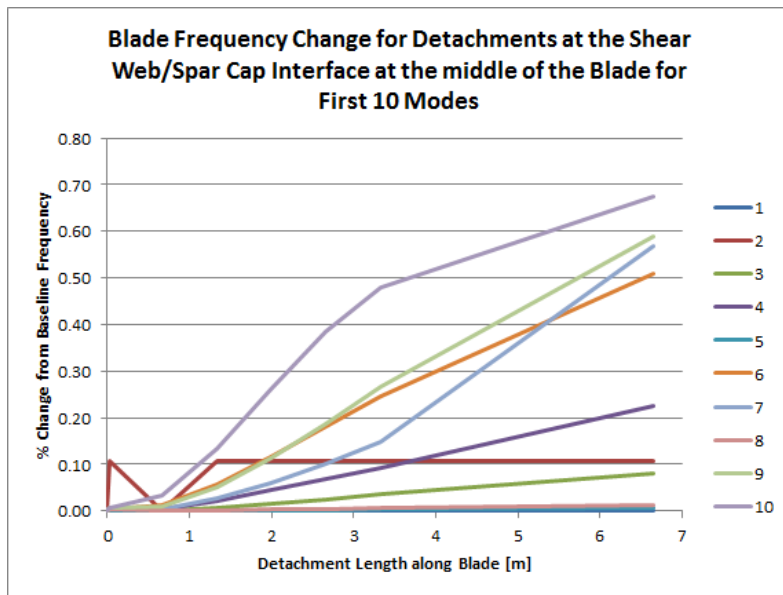


Figure 5-20: Natural frequency difference for first 10 modes at shear web/spar cap interface near blade mid-length

Only cracks which initiate at the widest chord cause a relatively large change in blade natural frequency, as seen in Figure 5-21.

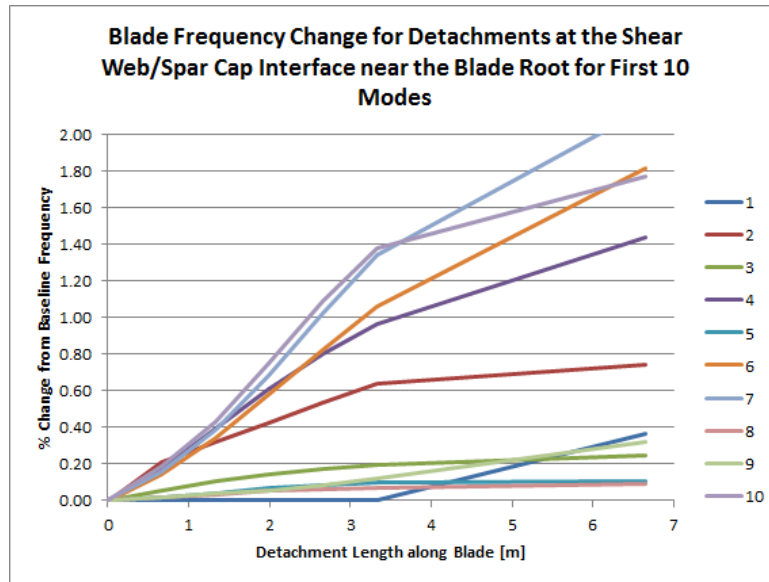


Figure 5-21: Natural frequency differences for first 10 modes at shear web/spar cap interface at largest chord

It is not unexpected that lightning strikes to produce large internal pressures as a result of rapid heat expansion, and likely regions of resulting cracks in attachment resin occur at the trailing edge and at the shear web/spar cap interface. However, these Abaqus natural frequency results indicate that without sensitive measuring systems in place, it might be impractical to attempt to detect small cracks using the method of measuring natural frequency changes from the baseline. The goal of this section is to act as a guide for sensor requirements for detecting damage size. Cracks along the trailing edge are relatively easier to identify than cracks at the interface of the shear web and spar cap, which is difficult to visually detect as well. The results must also take into account the effect of wind load carrying capacity. Noting that the higher flap mode shapes and the first torsion mode shape produce the biggest changes in natural frequency, it is important to understand that while smaller cracks are easier to detect for these modes, they might not be important with regards to wind load carrying capacity. Modes that are strong drivers in terms of frequency variation might not be of particular import depending on a blade's expected loading characteristics. The key questions to take away are what critical modes are getting impacted, and how much? The answers depend on the blade type and the load cases which it was designed for. It is possible that small cracks could go undetected for certain modes, but if the reason they are going undetected is because they do not heavily impact the typical loading cases corresponding to those modes, then the fact that a crack exists at that particular location might not be important from a load carrying standpoint. However, undetected cracks

can quickly grow to sizes that do in fact impact blade life, which makes undetected cracks, regardless of whether they initiate at locations where load carrying capacity is unaffected, are can result in expensive repairs and turbine down-time.

6. Conclusions and Future Work

The Abaqus thermomechanical plate studies confirm that very little material damage due to plastic yielding occurs outside of the lightning strike radius. The low thermal conductivity of E-glass composite material prevents extensive thermal diffusion, and as a result, the areas at which high temperature is observed are restricted to the material within 1 mm of the strike radius. Thermal stresses only exceed material strength in these high-temperature regions, where the composite material strength is substantially lower than at room temperature. Consequently, areas of material damage do not extend farther than 0.5 mm outside of the lightning strike zone in the radial-direction or 0.2 mm in the thickness-direction for direct strikes to composite material. For strikes to copper lightning protection receptors, E-glass damage is limited to less than 0.3 mm outside of the lightning strike zone in the radial-direction while no damage is observed below the plate surface in the thickness-direction. As demonstrated in Chapter 4, it is possible that analyzing only the S11 and S22 stresses does not present the most conservative yield results. It is conceivable that combined loading cases, which were not considered in this paper, could lead to worst-case yielding scenarios. Additional studies must determine the exact damage extend under a variety of specific loading conditions.

Chapter 5 shows that, depending on location within the blade, relatively large cracks produce very small changes in blade natural frequency. For seams between the shear web and spar cap near the tip of the blade, a crack four m long will result in a change in only 0.2% from the baseline frequency. Cracks along the trailing edge of the blade are easier to detect, assuming the frequency measurement system is capable of detecting higher modal frequencies, but cracks can still go unnoticed if the minimum detectable frequency change is large enough. Without sensitive equipment, it might be impractical to detect small cracks with the method of measuring changes in natural frequencies. It is recommended that an increased number of robust, sensitive frequency measurement systems be used to detect modal frequency changes. Alternative methods of detecting blade damage should also be pursued. Although it might not be the most cost-effective method, perhaps the industry should move toward more frequent site inspections, especially after known lightning activity in the area. Crack initiation can quickly lead to rapid crack grown, which can lead to expensive down-time. An additional complication that should be

investigated further is that regardless of sensor resolution accuracy, material property variation and inconsistent manufacturing tolerances might actually present a larger variation in blade frequency than the sensor resolution. Even testing a single blade in the field, the material property variation due to fatigue during use might be more of a variation than damage variation. Material variation issues might not be critical if there is a robust experimental frequency and mode shape measurement plan before and after damage occurs for every blade, but that might not be feasible, especially for commercial blades in the field. Further research is required to determine the frequency variation resulting from differences in material properties compared to the frequency variation resulting from blade damage.

The next phase of lightning strike research includes testing material samples to determine exact blade material properties to eventually model and find any potential deterioration in performance or decrease in fatigue life, comparing this to the FEA model results. This includes running tension and compression tests with a Split-Hopkinson pressure bar over a range of high temperatures to get material properties as a function of temperature. The idea would be to get exact temperature-dependent material properties in order to improve the thermomechanical model. Material testing at elevated temperatures is essential in understanding specific material properties in order to create a robust and accurate model.

If time and resources allow, there may be an opportunity to use Sandia National Laboratories' lightning strike facility. The goal would be to provide experimental data that could supplement the literature research information for lightning flux and temperature inputs to the model. The Sandia Lightning Simulator has the capabilities of simulating severe lightning strikes up to a maximum peak current of 200 kA for a single stroke [46]. The advantage of using the Sandia Lightning Simulator to gather data is that the heat transfer model can be improved to match real data, adding confidence to the results.

A robust thermomechanical blade model is recommended for future research in order to determine actual damage for the complex geometry of the turbine blade when lightning attachment occurs. The effects can then be assessed, similar to the blade condition analysis, to determine whether the amount of damage is able to be traced with current damage detection practices. In addition, data from such a complex model can be used to find the effects in long-term blade fatigue performance.

When lightning directly strikes a turbine blade, it can travel on the outside of the blade surface, the inside surface, or within the blade laminations. Lightning often takes more than one of these paths, resulting in a damage pattern known as stitching [2]. This happens when a lightning discharge creates a hole in the blade material, continuing some distance inside the blade, and then passing back out. Figure 6-1 shows a damage pattern when stitching is repeated more than once along a blade segment.



Figure 6-1: Stitching pattern a blade material pattern, generated in a laboratory [2]

It is possible for complete puncturing of the blade material to result in a high-pressure shock wave, creating a large internal force. Modeling this phenomenon would be very important for future work to determine the effects of this type of damage.

The lightning heat transfer analysis in this thesis is limited to a single type of lightning protection system (an external copper lightning receptor). A more thorough analysis of multiple lightning protection options is recommended in order to represent a wider range of wind turbines in the field, including a system with multiple lightning receptors. The use of multiple receptors is required for blades greater than 30 m in order to provide better protection for a blade than would otherwise be provided by a single receptor located at the tip of the blade [10]. Although not as prevalent, modeling a protection system in which the conductor is at or near the surface of the blade, such as concepts C and D in Figure 2-7, would be useful to the wind energy community. In conjunction with the different types of lightning protection systems, future research can determine the effects of lightning strikes at different locations along the blade. This thesis focuses on attachment points above the spar cap, near the tip of the blade. Studies have shown that long wind turbine blades are vulnerable to lightning strike attachment away from the tip receptor [10]. Strikes at other locations can be analyzed in order to find the performance effects of different attachment points.

Artificial lightning testing on graphite-epoxy composite material has shown a type of damage commonly found with fiberglass composite damaged by lightning strikes. One of the major causes of fiber damage is considered to be shockwaves due to supersonic-speed expansion of the ionized leader channel when a return stroke occurs [47]. While observations at the attachment point show that resin evaporation is present, further study is recommended for the fiber damage resulting from the lightning channel shockwaves. This phenomenon has not been extensively researched, so the full effects of the lightning channel expansion are currently unknown.

Bibliography

- [1] American Wind Energy Association, "U.S. Wind Industry Fourth Quarter 2011 Market Report," 2012.
- [2] I. Cotton, N. Jenkins and K. Pandiaraj, "Lightning Protection for Wind Turbine Blades and Bearings.," *Wind Energy*, vol. 4, no. 1, pp. 23-37, 2001.
- [3] F. Rachidi, M. Rubinstein and J. Montanya, "A Review of Current Issues in Lightning Protection of New-Generation Wind-Turbine Blades.," *IEEE Transactions on Industrial Electronics*, vol. 5, no. 6, pp. 2489-2496, 2008.
- [4] M. Hoppe-Kilpper and M. Durstewitz, "Blitz und Überspannungsschutz von Windkraftanlagen," in *Institut für solare Energieversorgungstechnik (ISET), BMBF-Gespräch Blitzschutz von Windkraftanlagen*, Bonn, 1995.
- [5] "Lightning Protection," Solacity Inc., [Online]. Available: <http://www.solacity.com/Lightning.htm>. [Accessed 20 August 2011].
- [6] B. Chittum, "Why Protecting Wind Turbines from Lightning Is Critical.," *Renewable Energy World*, 28 December 2009. [Online]. Available: <http://www.renewableenergyworld.com/rea/blog/post/2009/12/why-protecting-wind-turbines-from-lightning-is-critical1>. [Accessed 22 February 2011].
- [7] S. G. Krämer, F. P. León, B. Lewke and Y. M. Hernández, "Lightning Impact Classification on Wind Turbine Blades Using a Fiber Optic Measurement System.," Technische Universität München, Fachgebiet Verteilte Messsysteme, Munich.
- [8] T. Soerensen, "Lightning protection of wind turbines," in *Lightning Protection*, London, Institution of Electrical Engineers, 2010, pp. 681-722.
- [9] J. C. Watson and J. C. Serrano, "Composite Materials for Wind Blades," Media Solutions,

- Inc., 2010.
- [10] B. Glushakow, "Effective Lightning Protection for Wind For Wind Turbine Generators," *IEEE Transactions on Energy Conversion*, vol. 22, no. 1, pp. 214-222, 2007.
- [11] M. Caie and M. Gassman, "Planning for Lightning Protection on Wind Turbines.," *Wind Power: Engineering & Development*, 5 April 2010. [Online]. Available: <http://www.windpowerengineering.com/policy/environmental/planning-for-lightning-protection-on-wind-turbines/>. [Accessed 26 January 2011].
- [12] S. Yokoyama, "Lightning Protection of Wind Turbine Generation Systems," in *7th Asia-Pacific International Conference on Lightning*, Chengdu, China, 2011.
- [13] R. Kathil, "Case Study of Lightning Damage to Wind Turbine Blade," National Lightning Safety Institute, 2008.
- [14] R. R. Hill, J. A. Stinebaugh, D. Briand, A. S. Benjamin and J. Lindsay, "Wind Turbine Reliability: A Database and Analysis Approach," Sandia National Laboratories, Albuquerque, 2008.
- [15] L. Rademakers, H. Braam, H. R. A. Wessels, R. K. N. J. Prins, R. Lok, L. Leunis and S. Ramakers, "Lightning damage of OW ECS (Part 1: 'parameters relevant for cost modeling')," 2002.
- [16] F. M. Larsen and T. Sorensen, "New Lightning Qualification Test Procedure for Large Wind Turbine Blades".
- [17] T. S. Sorensen, "The Update of IEC 61400-24 Lightning Protection of Wind Turbines," in *29th International Conference on Lightning Protection*, Uppsala, Sweden, 2008.
- [18] F. Heidler, J. M. Cvetic and B. V. Stanic, "Calculation of Lightning Current Parameters," *IEEE Transactions on Power Delivery*, vol. 14, no. 2, pp. 399-404, April 1999.

- [19] F. Heidler, W. Zischank, Z. Flisowski, C. Bouquegneau and C. Mazzetti, "Parameters of Lightning Current Given in IEC 62305 - Background, Experience and Outlook," in *29th International Conference on Lightning Protection*, Uppsala, Sweden, 2008.
- [20] V. A. Rakov and M. A. Uman, *Lightning: Physics and Effects*, Cambridge, U.K.: Cambridge UP, 2003.
- [21] T. Ogasawara, Y. Hirano and A. Yoshimura, "Coupled thermal-electrical analysis of carbon fiber/epoxy composites exposed to simulated lightning current," *Composites Part A: Applied Science and Manufacturing*, vol. 41, no. 8, pp. 973-981, 2010.
- [22] E. U. Chowdhury, M. F. Green, L. A. Bisby, N. Benichou and V. K. R. Kodur, "Thermal and Mechanical Characterization of Fibre Reinforced Polymers, Concrete, Steel, and Insulation Materials for use in Numerical Fire Endurance Modelling," National Research Council Canada.
- [23] F. P. Incropera and D. P. DeWitt, *Fundamentals of Heat and Mass Transfer*, 6th ed., New York: Wiley, 1990.
- [24] "MatWeb Material Property Data," [Online]. Available: www.matweb.com. [Accessed 2012].
- [25] "The Engineering ToolBox," [Online]. Available: http://www.engineeringtoolbox.com/melting-boiling-temperatures-d_392.html. [Accessed 2012].
- [26] "Pure Copper," ARIES Program UC San Diego, [Online]. Available: <http://aries.ucsd.edu/LIB/PROPS/PANOS/cu.html>. [Accessed 2012].
- [27] "Thermal insulation materials made of rigid polyurethane foam," BING: Federation of European Rigid Polyurethane Foam Associations, October 2006. [Online]. Available: <http://www.excellence-in-insulation.eu/site>. [Accessed 2012].

- [28] "PVCell™ G-Foam Structural Foam Core," Gurit, [Online]. Available:
<http://www.gurit.com/files/documents/pvcellgfoamv1pdf.pdf>. [Accessed 2012].
- [29] J. M. Yang and T. N. Tiegs, "Strength and Toughness of Ceramic Composites at Elevated Temperatures," in *High Temperature Mechanical Behavior of Ceramic Composites*, Elsevier, 1995, pp. 87-119.
- [30] Toray Carbon Fibers America, Inc., "T300 Data Sheet".
- [31] J. W. Klett, V. J. Ervin and D. D. Edie, "Finite-element modeling of heat transfer in carbon/carbon composites," *Composites Science and Technology*, vol. 59, no. 4, pp. 593-607, 1999.
- [32] M. W. Hyer, C. T. Herakovich, S. M. Milkovich and J. S. Short, "Temperature dependence of mechanical and thermal expansion properties of T300/5208 graphite/epoxy," *Composites*, vol. 14, no. 3, pp. 276-280, 1983.
- [33] "Abaqus Analysis User's Manual," Simulia, 2011.
- [34] B. Berenberg, "About.com Composites/Plastics," [Online]. Available:
http://composite.about.com/od/data/1/blg_egepoxy.htm. [Accessed 2012].
- [35] V. Cecen, I. H. Tavman, M. Kok and Y. Aydogdu, "Epoxy- and Polyester-Based Composites Reinforced With Glass, Carbon and Aramid Fabrics: Measurement of Heat Capacity and Thermal Conductivity of Composites by Differential Scanning Calorimetry," *Polymer Composites*, vol. 30, no. 9, pp. 1299-1311, 2009.
- [36] B. W. James, G. H. Wostenholm, G. S. Keen and S. D. McIvor, "Prediction and measurement of the thermal conductivity of composite materials," *Appl. Phys.*, vol. 20, pp. 261-268, 1987.
- [37] AGY, "High Strength Glass Fibers," 2006. [Online]. Available:
http://www.agy.com/technical_info/graphics_PDFs/HighStrengthTechPaperEng.pdf.

[Accessed February 2012].

- [38] "Polymer Material Properties: Epoxy," efunda, [Online]. Available: http://www.efunda.com/materials/polymers/properties/polymer_cat.cfm. [Accessed February 2012].
- [39] Y. C. Wang and V. Kodur, "Variation of strength and stiffness of fibre reinforced polymer reinforcing bars with temperature," *Cement & Concrete Composites*, vol. 27, no. 9-10, pp. 864-874, 2005.
- [40] B. Lu, Y. Li, X. Wu and Z. Yang, "A Review of Recent Advances in Wind Turbine Condition Monitoring and Fault Diagnosis," *IEEE*, 2009.
- [41] Z. Hameed, Y. S. Hong, Y. M. Cho, S. H. Ahn and C. K. Song, "Condition monitoring and fault detection of wind turbines and related algorithms: A review," *Renewable and Sustainable Energy Reviews*, vol. 13, pp. 1-39, 2009.
- [42] C. C. Ciang, J.-R. Lee and H.-J. Bang, "Structural health monitoring for a wind turbine system: a review of damage detection methods," *Measurement Science and Technology*, vol. 19, pp. 1-20, 2008.
- [43] M. Edon, "38 Meter Wind Turbine Blade Design," Tech. Denmark: Nordvestjysk Folkecenter for Vedvarende Energi, 2007.
- [44] S. C. Quek, Interviewee, *Wind Turbine Blade Geometry and Materials*. [Interview]. 2012.
- [45] "NACA 64(3)-618," Airfoil Investigation Database, 25 February 2012. [Online]. Available: <http://www.worldofkrauss.com/foils/1671>.
- [46] M. Caldwell and L. E. Martinez, "The Sandia Lightning Simulator: Recommissioning and Upgrades," Albuquerque.
- [47] Y. Hirano, S. Katsumata, Y. Iwahori and A. Todoroki, "Artificial Lightning Testing on

Graphite/epoxy Composite Laminate," *Composites: Part A: Applied Science and Manufacturing*, vol. 41, no. 8, pp. 1461-1470, 2010.

[48] K. J. Jackson, M. D. Zuteck, C. P. van Dam, K. J. Standish and D. Berry, "Innovative Design Approaches for Large Wind Turbine Blades," *Wind Energy*, vol. 8, pp. 141-171, 2005.

[49] L. Fingersh, M. Hand and A. Laxson, "Wind Turbine Design Cost and Scaling Model," 2006.

Appendix A: Heat Transfer Calculations

A.1. 1-D MathCAD Heat Transfer Calculations

MathCAD V15.0 was used for analytical one-dimensional calculations [7], [46], [20], [23]:

Chris Severino

Temperature Calculation at $t=0$ for r =radius of copper puck

Protection level	Peak current [kA]	Specific energy [kJ/Ω]	Average rate of current rise [kA/μs]	Total charge transfer [C]
I	200	10000	200	300
II	150	5600	150	225
III	100	2500	100	150
IV				

200 kA for worst case scenario

Krämer, Sebastian G.M. *Lightning Impact Classification on Wind Turbine Blades Using a Fiber Optic Measurement System*. Tech. Munich: Technische Universität München. Garching: GE Global Research, Hybrid & Renewable Systems Lab.

Lightning parameters	STS requirements		Known parameters	
	Most severe	50% level	2% level	50% level
Peak current ¹	200 kA	20 kA	140 kA	20 kA
Time to peak current	0.2 μs	2.0 μs	12 μs	1.8 μs
Current rate of rise	100 kA/μs	20 kA/μs	100 kA/μs	22 kA/μs
Pulse width (full width half maximum)	200 μs	50 μs	170 μs	45 μs
Continuing current amplitude	700 A	140 A	520 A	140 A
Continuing current duration	500 ms	160 ms	400 ms	160 ms
Number of strokes	1 - 12	2	10 -11	2 - 3

1. Caldwell, Michele, and Leonard E. Martinez. *The Sandia Lightning Simulator: Recommissioning and Upgrades*. Tech. Albuquerque, NM: Sandia National Laboratories.

From these sources, I'm using a lightning current amplitude of 200,000 A and a duration time of 200 microseconds = $2 \cdot 10^{-4}$ seconds

Table 4.9. Estimated characteristics of the lightning channels associated with various processes of the lightning discharge. Adapted from Rakov (1998)

Channel characteristics ^a	Pre-dart-leader channel (ahead of dart-leader front)	Pre-return-stroke channel (behind dart-leader front and ahead of return-stroke front)	Return-stroke channel (behind return-stroke front)
Temperature, K	~ 3000	≥ 20 000	≥ 30 000
Conductivity, S m ⁻¹	~ 0.02	~ 10 ⁴	~ 10 ⁴
Radius, cm	~ 3	~ 0.3	~ 3
R, Ω m ⁻¹	~ 18 000	~ 3.5	~ 0.035

^aFor comparison, the electrical conductivity of carbon is $3 \times 10^4 \text{ S m}^{-1}$, of seawater is 4 S m^{-1} , and of copper is $5.8 \times 10^7 \text{ S m}^{-1}$ (Sadiku 1994); the temperature of the solar interior is 10^7 K and of the solar surface is 6000 K , and the temperatures at which tungsten and lead melt are 3600 K and 600 K , respectively (Halliday and Resnick 1974).

Rakov, Vladimir A., and Martin A. Uman. *Lightning: Physics and Effects*. Cambridge, U.K.: Cambridge UP, 2003.

http://books.google.com/books?hl=en&lr=&id=NvIMsvVOHJ4C&oi=fnd&pg=PA1&dq=lightning+damage+conducting+pole&ots=uK5lxuQzJZ&sig=_6xSsrhZ6uQtCHk6W7p007j0VCU#v=onepage&q=temperature&f=true

30,000K is temperature of lightning return stroke

Copper Properties

all properties are assumed at melting temperature

$$c_p := 506 \cdot \frac{\text{J}}{\text{kg} \cdot \text{K}} \quad \text{specific heat}$$

$$\rho := 7940 \cdot \frac{\text{kg}}{\text{m}^3} \quad \text{density}$$

$$k := 335.74 \cdot \frac{\text{W}}{\text{m} \cdot \text{K}}$$

$$\alpha := \frac{k}{\rho \cdot c_p} \quad \alpha = 8.357 \times 10^{-5} \frac{\text{m}^2}{\text{s}} \quad \text{thermal diffusivity}$$

Geometry of Puck

$$r := .01 \cdot \text{m} \quad \text{radius of copper puck}$$

$$L := .048 \cdot \text{m} \quad \text{thickness of composite skin and puck}$$

$$A := \pi \cdot r^2 \quad A = 3.142 \times 10^{-4} \text{ m}^2$$

Surface Heat Flux Calculation

$T_s := 300\text{-K}$ surface is room temperature

$T := 30000\text{-K}$ lightning temperature (Rakov)

$$\sigma := 5.67 \cdot 10^{-8} \cdot \left(\frac{\text{W}}{\text{m}^2 \cdot \text{K}^4} \right)$$

$$q_{\text{sflux}} := \sigma \cdot (T^4 - T_s^4)$$

$$q_{\text{sflux}} = 4.593 \times 10^{10} \cdot \frac{\text{W}}{\text{m}^2}$$

Temperature Calculation as a function of x and t

For constant heat flux:

Incropera, Frank P., and David P. DeWitt. Fundamentals of Heat and Mass Transfer. 6th ed. New York: Wiley, 1990. Pg 286: Transient Conduction for Constant Surface Heat Flux.

$\tau := 2 \cdot 10^{-4} \cdot \text{s}$ time of lightning strike

$$T(x, t) := \begin{cases} \frac{2 \cdot q_{\text{sflux}} \cdot \left(\frac{\alpha \cdot t}{\pi} \right)^{\frac{1}{2}} \cdot e^{\left(\frac{-x^2}{4 \cdot \alpha \cdot t} \right)} - \frac{q_{\text{sflux}} \cdot x}{k} \cdot \text{erfc} \left(\frac{x}{2 \cdot \sqrt{\alpha \cdot t}} \right)}{k} & \text{if } t \leq \tau \\ \left[\frac{2 \cdot q_{\text{sflux}} \cdot \left[\frac{\alpha \cdot (t - \tau)}{\pi} \right]^{\frac{1}{2}} \cdot e^{\left[\frac{-x^2}{4 \cdot \alpha \cdot (t - \tau)} \right]} - \frac{q_{\text{sflux}} \cdot x}{k} \cdot \text{erfc} \left[\frac{x}{2 \cdot \sqrt{\alpha \cdot (t - \tau)}} \right]}{k} \right] \dots & \text{if } t > \tau \\ + \left[\frac{2 \cdot q_{\text{sflux}} \cdot \left(\frac{\alpha \cdot t}{\pi} \right)^{\frac{1}{2}} \cdot e^{\left(\frac{-x^2}{4 \cdot \alpha \cdot t} \right)} - \frac{q_{\text{sflux}} \cdot x}{k} \cdot \text{erfc} \left(\frac{x}{2 \cdot \sqrt{\alpha \cdot t}} \right)}{k} \right] & \end{cases}$$

$$T(0, .000001 \cdot \text{s}) = 1.411 \times 10^3 \text{ K}$$

$$T(0, .0001 \cdot \text{s}) = 1.411 \times 10^4 \text{ K}$$

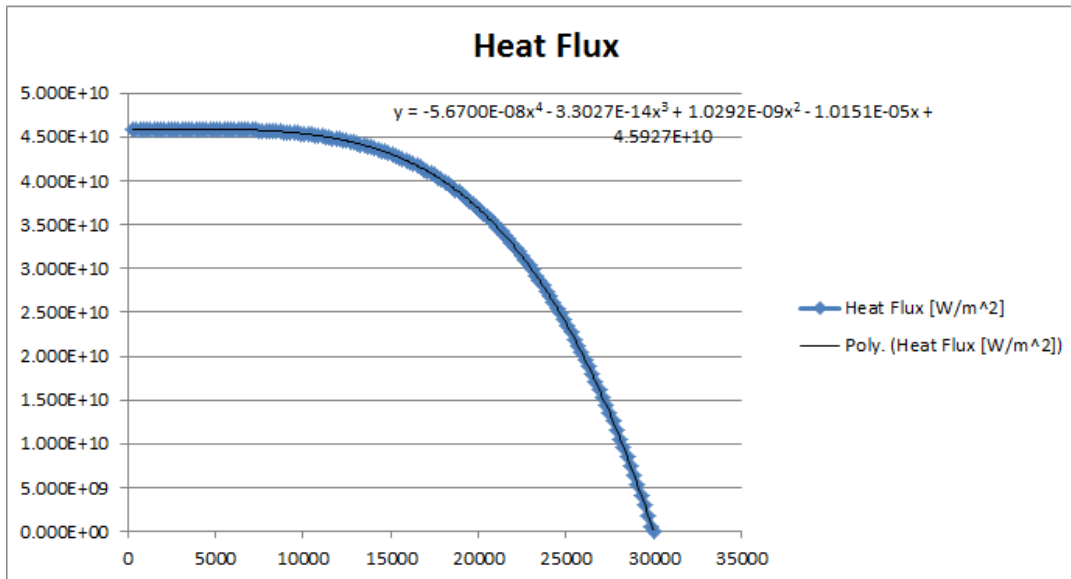
$$T(0, .0002 \cdot \text{s}) = 1.995 \times 10^4 \text{ K}$$

A.2. Excel Heat Flux Calculations

Excel was used to determine heat flux as a function of the surface temperature of the lightning strike area of the blade:

Surface Temperature [K]	Heat Flux [W/m ²]	
Room Temp	$5.67 \cdot 10^{-8} \cdot (30000^4 - A^4)$	
300	4.593E+10	
500	4.593E+10	
700	4.593E+10	
900	4.593E+10	

Calculations continue until surface temperature is 30,000 K (zero radiative heat flux).



A.3. Abaqus-CAE Copper Ablation Input File

Abaqus-CAE V6.11-2 was used for a 1-D heat transfer analysis to determine the depth of ablation of copper and E-glass composite. The copper input file is shown here (abridged to save space):

```
*Heading
** Job name: CopperFluxVerySmallMesh Model name: Model-1
** Generated by: Abaqus/CAE 6.10-2
*Preprint, echo=NO, model=NO, history=NO, contact=NO
**
** PARTS
**
*Part, name=Part-1
*Node
  1, 9.56940348e-05, 2.90284679e-05, 0.
... remainder of mesh nodes are not included for brevity...
*Nset, nset=_PickedSet2, internal, generate
```

```

1, 48581, 1
*Elset, elset=_PickedSet2, internal, generate
1, 44800, 1
** Section: Section-1
*Solid Section, elset=_PickedSet2, material=Copper
,
*End Part
**
**
** ASSEMBLY
**
*Assembly, name=Assembly
**
*Instance, name=Part-1-1, part=Part-1
*End Instance
**
*Nset, nset=_PickedSet8, internal, instance=Part-1-1, generate
1, 481, 1
*Elset, elset=_PickedSet8, internal, instance=Part-1-1, generate
1, 448, 1
*Elset, elset=_FluxIn_S1, internal, instance=Part-1-1, generate
44353, 44800, 1
*Surface, type=ELEMENT, name=FluxIn
_FluxIn_S1, S1
*Elset, elset=_PickedSurf10_S1, internal, instance=Part-1-1, generate
44353, 44800, 1
*Surface, type=ELEMENT, name=_PickedSurf10, internal
_PickedSurf10_S1, S1
*Elset, elset=_PickedSurf11_S1, internal, instance=Part-1-1, generate
44353, 44800, 1
*Surface, type=ELEMENT, name=_PickedSurf11, internal
_PickedSurf11_S1, S1
*End Assembly
**
** MATERIALS
**
*Material, name=Copper
*Conductivity
390.,
*Density
7764.,
*Specific Heat
385.,
**
** BOUNDARY CONDITIONS
**
** Name: BC-1 Type: Temperature
*Boundary
_PickedSet8, 11, 11
** -----
**
** STEP: RT
**
*Step, name=RT
*Heat Transfer, steady state, deltmx=0.
1., 1., 1e-05, 1.,
**
** BOUNDARY CONDITIONS
**
** Name: BC-1 Type: Temperature
*Boundary
_PickedSet8, 11, 11, 300.
**
** OUTPUT REQUESTS
**
*Restart, write, frequency=0
**
** FIELD OUTPUT: F-Output-1
**
*Output, field, variable=PRESELECT

```

```

*Output, history, frequency=0
*End Step
** -----
**
** STEP: Lightning
**
*Step, name=Lightning, inc=5
*Heat Transfer, end=PERIOD
5e-05, 0.0002, , ,
**
** LOADS
**
** Name: Load-1  Type: Surface heat flux
*Dflux
_PickedSurf11, S, 4.593e+10
**
** INTERACTIONS
**
** Interaction: Int-1
*Sfilm
_PickedSurf10, F, 30000., 5.
**
** OUTPUT REQUESTS
**
*Restart, write, frequency=0
**
** FIELD OUTPUT: F-Output-1
**
*Output, field, variable=PRESELECT
*Output, history, frequency=0
*End Step
** -----
**
** STEP: After
**
*Step, name=After, inc=5
*Heat Transfer, end=PERIOD
0.0001, 0.0004, , ,
**
** LOADS
**
** Name: Load-1  Type: Surface heat flux
*Dflux
_PickedSurf11, S, 0.
**
** INTERACTIONS
**
** Interaction: Int-1
*Sfilm
_PickedSurf10, F, 300., 5.
**
** OUTPUT REQUESTS
**
*Restart, write, frequency=0
**
** FIELD OUTPUT: F-Output-1
**
*Output, field, variable=PRESELECT
*Output, history, frequency=0
*End Step

```

A.4. 1-D MathCAD Heat Transfer Calculations for Ablation Depth

MathCAD V15.0 was used for analytical one-dimensional calculations [23]:

Copper Properties all properties are assumed at melting temperature

$$C_{p_c} := 506 \cdot \frac{\text{J}}{\text{kg} \cdot \text{K}} \quad \text{specific heat}$$

$$\rho_c := 7940 \cdot \frac{\text{kg}}{\text{m}^3} \quad \text{density}$$

$$k_c := 335.74 \cdot \frac{\text{W}}{\text{m} \cdot \text{K}}$$

$$\alpha_c := \frac{k_c}{\rho_c \cdot C_{p_c}} \quad \alpha_c = 8.357 \times 10^{-5} \frac{\text{m}^2}{\text{s}} \quad \text{thermal diffusivity}$$

Temperature Calculation as a function of x and t

For constant heat flux:

Incropera, Frank P., and David P. DeWitt. Fundamentals of Heat and Mass Transfer. 6th ed. New York: Wiley, 1990. Pg 286: Transient Conduction for Constant Surface Heat Flux.

$$t := 2 \cdot 10^{-4} \cdot \text{s} \quad \text{time of lightning strike}$$

$$T(x) := \frac{2 \cdot q_{\text{sflux}} \cdot \left(\frac{\alpha_c \cdot t}{\pi} \right)^{\frac{1}{2}}}{k_c} \cdot e^{\left(\frac{-x^2}{4 \cdot \alpha_c \cdot t} \right)} - \frac{q_{\text{sflux}} \cdot x}{k_c} \cdot \text{erfc} \left(\frac{x}{2 \cdot \sqrt{\alpha_c \cdot t}} \right)$$

$$T(0) = 1.995 \times 10^4 \text{ K}$$

$$T(.000218 \cdot \text{m}) = 2.85 \times 10^3 \text{ K}$$

This suggests that copper is above its vaporization temperature of 2868 K down to a depth of 0.218mm.

E-glass Composite Properties

$$C_{p_{cc}} := 850 \cdot \frac{\text{J}}{\text{kg} \cdot \text{K}} \quad \text{specific heat}$$

$$\rho_{cc} := 2100 \cdot \frac{\text{kg}}{\text{m}^3} \quad \text{density}$$

$$k_{cc} := .18 \cdot \frac{\text{W}}{\text{m} \cdot \text{K}} \quad \text{thermal conductivity in the transverse/depth direction}$$

$$\alpha_{cc} := \frac{k_{cc}}{\rho_{cc} \cdot C_{p_{cc}}} \quad \alpha_{cc} = 1.008 \times 10^{-7} \frac{\text{m}^2}{\text{s}} \quad \text{thermal diffusivity}$$

Temperature Calculation as a function of x and t

For constant heat flux:

Incropera, Frank P., and David P. DeWitt. Fundamentals of Heat and Mass Transfer. 6th ed. New York: Wiley, 1990. Pg 286: Transient Conduction for Constant Surface Heat Flux.

$$t := 2 \cdot 10^{-4} \cdot \text{s} \quad \text{time of lightning strike}$$

$$T(x) := \frac{2 \cdot q_{sflux} \cdot \left(\frac{\alpha_{cc} \cdot t}{\pi} \right)^{\frac{1}{2}} \cdot e^{\left(\frac{-x^2}{4 \cdot \alpha_{cc} \cdot t} \right)} - \frac{q_{sflux} \cdot x}{k_{cc}} \cdot \text{erfc} \left(\frac{x}{2 \cdot \sqrt{\alpha_{cc} \cdot t}} \right)}$$

$$T(0) = 1.293 \times 10^6 \text{ K}$$

$$T(.0000187\text{-m}) = 1.505 \times 10^3 \text{ K}$$

This suggests that E-glass composite is above melting temperature of 1500 K down to a depth of 0.0187mm (Abaqus finds this to be .025mm).

$$T(.00001954\text{-m}) = 942.34 \text{ K}$$

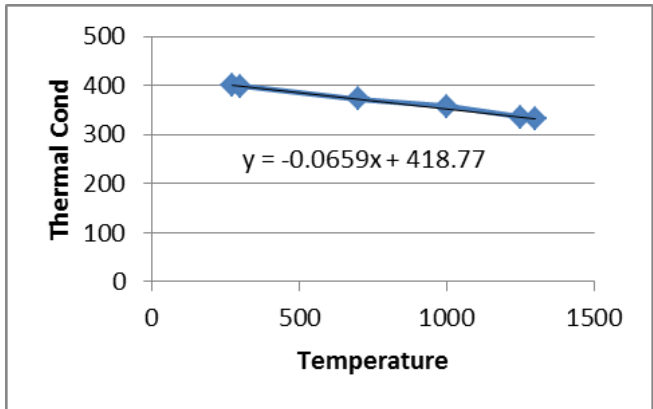
This suggests that E-glass composite is above melting temperature of 943 K down to a depth of 0.01954mm (Abaqus finds this to be .0275mm).

Appendix B: Material Calculations

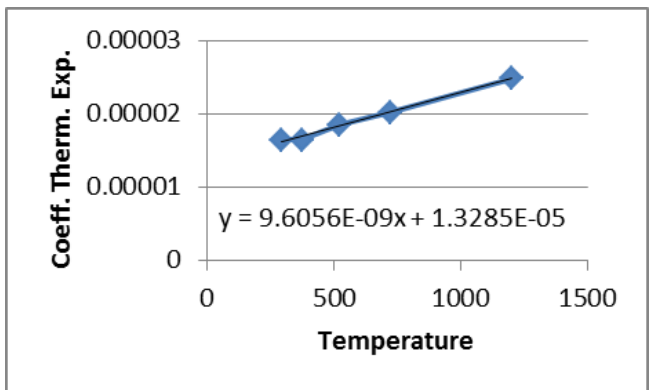
B.1. Excel Material Calculations for Copper

Copper linear extrapolation from linear trend lines [24], [26]:

Thermal Conductivity [W/m-K]	Temperature, K
401	273
398	300
372	700
357	1000
335.13	1250
331.71	1300
329.37006	1356.6
Final point extrapolated with best fit linear line:	



Coefficient of Thermal [m/m-K]	Temperature, K
0.0000164	293
0.0000164	373
0.0000185	523
0.0000202	723
0.0000248	1198
0.0000263	1356.6
Final point extrapolated with best fit linear line:	



B.2. Excel Material Calculations for T300-Epoxy Carbon Composite

Material testing by Hyer et al. provides the following least-squares fit curve equations and corresponding equations for various parameters [32].

Table 1. Coefficients for temperature dependence of elastic and strength properties*

Property	C_0	C_1	C_2
E_1 (GPa)	1.82×10^2	-2.72×10^{-1}	5.18×10^{-4}
E_2 (GPa)	1.47×10^2	-8.03×10^{-1}	1.16×10^{-3}
ν_{12}	6.29×10^{-1}	-1.22×10^{-3}	3.94×10^{-7}
G_{12} (GPa)	7.46	6.52×10^{-3}	-2.73×10^{-5}
σ_1^{ult} (MPa)	1.07×10^3	1.14	3.05×10^{-4}
σ_2^{ult} (MPa)	45.4	-1.35×10^{-1}	2.61×10^{-4}

* $P = C_0 + C_1T + C_2T^2$ where P is the property of interest and T is temperature in K

Table 2. Coefficients for temperature dependence of thermal expansion*

Laminate	C_0	C_1	C_2	C_3
0°	-110	1.84	-0.810×10^{-2}	0.106×10^{-4}
90°	-5570	18.0	-0.903×10^{-2}	0.404×10^{-4}
Quasi-isotropic	-626	2.48	-0.338×10^{-2}	0.686×10^{-5}

* $\epsilon = C_0 + C_1T + C_2T^2 + C_3T^3$ where ϵ is the thermal strain in micro-strain units and T is the temperature in K

These equations and their coefficients were input into Excel to determine the directional material properties at 300 K and 400 K.

Modulus of Elasticity		[Pa]		
			$1.82 \times 10^{11} - 2.72 \times 10^8 T + 5.18 \times 10^5 T^2$	
Temperature, K		Fiber-direction		
300			1.4702E+11	
400			1.5608E+11	
			$1.47 \times 10^{11} - 8.03 \times 10^8 T + 1.16 \times 10^6 T^2$	
Temperature, K		Transverse-direction		
300			1.050E+10	
400			1.140E+10	
Poisson's Ratio		[-]		
			Coefficient of Thermal Expansion [m/m-K]	
			$(-110 + 1.84T - 0.81 \times 10^{-2} T^2 + 0.106 \times 10^{-4} T^3) \times 10^{-6}$	
Temperature, K		nu (1,2 direction)	Temperature, K	
300		0.298	Fiber-direction	
400		0.204	300	
			-8.00E-07	
			400	
			8.40E-06	
Shear Modulus		[Pa]		
			$(-5570 + 18T - 0.903 \times 10^{-2} T^2 + 0.404 \times 10^{-4} T^3) \times 10^{-6}$	
Temperature, K		G (1,2 direction)	Temperature, K	
300		3.687E+10	Transverse-direction	
400		5.887E+10	300	
			1.08E-04	
			400	
			2.77E-03	

B.3. Determination of Stiffness Matrix Terms for T300-Epoxy and E-glass Elastic Material Properties

Orthotropic Materials in Abaqus

T300 Properties: 300 K

$$E1 := 1.4702 \cdot 10^{11}$$

$$E2 := 1.05 \cdot 10^{10}$$

$$E3 := 1.05 \cdot 10^{10}$$

$$G12 := 3.687 \cdot 10^{10}$$

$$G13 := G12$$

$$\nu12 := .298$$

$$\nu23 := .4 \quad \text{estimate, similar for most epoxy composite materials}$$

$$\nu13 := .298$$

$$\nu21 := \nu12 \cdot \frac{E2}{E1}$$

$$\nu32 := \nu23$$

$$\nu31 := \nu21$$

$$G23 := \frac{E2}{2 \cdot (1 + \nu23)}$$

ABAQUS Analysis User's Manual section 19.2.1 Linear elastic behavior, Defines the stiffness matrix

$$\begin{Bmatrix} \sigma_{11} \\ \sigma_{22} \\ \sigma_{33} \\ \sigma_{12} \\ \sigma_{13} \\ \sigma_{23} \end{Bmatrix} = \begin{bmatrix} D_{1111} & D_{1122} & D_{1133} & 0 & 0 & 0 \\ & D_{2222} & D_{2233} & 0 & 0 & 0 \\ & & D_{3333} & 0 & 0 & 0 \\ & & & D_{1212} & 0 & 0 \\ & sym & & & D_{1313} & 0 \\ & & & & & D_{2323} \end{bmatrix} \begin{Bmatrix} \varepsilon_{11} \\ \varepsilon_{22} \\ \varepsilon_{33} \\ \gamma_{12} \\ \gamma_{13} \\ \gamma_{23} \end{Bmatrix} = [D^{el}] \begin{Bmatrix} \varepsilon_{11} \\ \varepsilon_{22} \\ \varepsilon_{33} \\ \gamma_{12} \\ \gamma_{13} \\ \gamma_{23} \end{Bmatrix}.$$

Abaqus Analysis User's Manual provides definitions for stiffness matrix terms [33]:

$$\begin{aligned}
D_{1111} &= E_1(1 - \nu_{23}\nu_{32})\Upsilon, \\
D_{2222} &= E_2(1 - \nu_{13}\nu_{31})\Upsilon, \\
D_{3333} &= E_3(1 - \nu_{12}\nu_{21})\Upsilon, \\
D_{1122} &= E_1(\nu_{21} + \nu_{31}\nu_{23})\Upsilon = E_2(\nu_{12} + \nu_{32}\nu_{13})\Upsilon, \\
D_{1133} &= E_1(\nu_{31} + \nu_{21}\nu_{32})\Upsilon = E_3(\nu_{13} + \nu_{12}\nu_{23})\Upsilon, \\
D_{2233} &= E_2(\nu_{32} + \nu_{12}\nu_{31})\Upsilon = E_3(\nu_{23} + \nu_{21}\nu_{13})\Upsilon, \\
D_{1212} &= G_{12}, \\
D_{1313} &= G_{13}, \\
D_{2323} &= G_{23},
\end{aligned}$$

$$\Upsilon := \frac{1}{1 - \nu_{12}\nu_{21} - \nu_{23}\nu_{32} - \nu_{31}\nu_{13} - 2\nu_{21}\nu_{32}\nu_{13}}$$

Stiffness Parameters (Abaqus Guide):

$D_{1111} := E_1 \cdot (1 - \nu_{23} \cdot \nu_{32}) \cdot \Upsilon$	$D_{1111} = 1.502 \times 10^{11}$
$D_{2222} := E_2 \cdot (1 - \nu_{13} \cdot \nu_{31}) \cdot \Upsilon$	$D_{2222} = 1.269 \times 10^{10}$
$D_{3333} := E_3 \cdot (1 - \nu_{12} \cdot \nu_{21}) \cdot \Upsilon$	$D_{3333} = 1.269 \times 10^{10}$
$D_{1122} := E_1 \cdot (\nu_{21} + \nu_{31} \cdot \nu_{23}) \cdot \Upsilon$	$D_{1122} = 5.328 \times 10^9$
$D_{1133} := E_1 \cdot (\nu_{31} + \nu_{21} \cdot \nu_{32}) \cdot \Upsilon$	$D_{1133} = 5.328 \times 10^9$
$D_{2233} := E_2 \cdot (\nu_{32} + \nu_{12} \cdot \nu_{31}) \cdot \Upsilon$	$D_{2233} = 5.189 \times 10^9$
$D_{1212} := G_{12}$	$D_{1212} = 3.687 \times 10^{10}$
$D_{1313} := G_{13}$	$D_{1313} = 3.687 \times 10^{10}$
$D_{2323} := G_{23}$	$D_{2323} = 3.75 \times 10^9$

T300 Properties: 400 K

$$E1 := 1.5608 \cdot 10^{11}$$

$$E2 := 1.14 \cdot 10^{10}$$

$$E3 := 1.14 \cdot 10^{10}$$

$$G12 := 5.887 \cdot 10^{10}$$

$$G13 := G12$$

$$\nu12 := .204$$

$$\nu23 := .4 \quad \text{estimate, similar for most epoxy composite materials}$$

$$\nu13 := .204$$

$$\nu21 := \nu12 \cdot \frac{E2}{E1}$$

$$\nu32 := \nu23$$

$$\nu31 := \nu21$$

$$G23 := \frac{E2}{2 \cdot (1 + \nu23)}$$

$$Y := \frac{1}{1 - \nu12 \cdot \nu21 - \nu23 \cdot \nu32 - \nu31 \cdot \nu13 - 2 \cdot \nu21 \cdot \nu32 \cdot \nu13}$$

Stiffness Parameters (Abaqus Guide):

$$D1111 := E1 \cdot (1 - \nu23 \cdot \nu32) \cdot Y \quad D1111 = 1.577 \times 10^{11}$$

$$D2222 := E2 \cdot (1 - \nu13 \cdot \nu31) \cdot Y \quad D2222 = 1.367 \times 10^{10}$$

$$D3333 := E3 \cdot (1 - \nu12 \cdot \nu21) \cdot Y \quad D3333 = 1.367 \times 10^{10}$$

$$D1122 := E1 \cdot (\nu21 + \nu31 \cdot \nu23) \cdot Y \quad D1122 = 3.916 \times 10^9$$

$$D1133 := E1 \cdot (\nu31 + \nu21 \cdot \nu32) \cdot Y \quad D1133 = 3.916 \times 10^9$$

$$D2233 := E2 \cdot (\nu32 + \nu12 \cdot \nu31) \cdot Y \quad D2233 = 5.526 \times 10^9$$

$$D1212 := G12 \quad D1212 = 5.887 \times 10^{10}$$

$$D1313 := G13 \quad D1313 = 5.887 \times 10^{10}$$

$$D2323 := G23 \quad D2323 = 4.071 \times 10^9$$

E-Glass Properties: 300 K

$$E1 := 4.18 \cdot 10^{10}$$

$$E2 := 9.49 \cdot 10^9$$

$$E3 := 9.49 \cdot 10^9$$

$$G12 := 3.51 \cdot 10^9$$

$$G13 := G12$$

$$\nu12 := .283$$

$$\nu23 := .3 \quad \text{estimate, set such that material properties agree with other sources}$$

$$\nu13 := .283$$

$$\nu21 := \nu12 \cdot \frac{E2}{E1}$$

$$\nu32 := \nu23$$

$$\nu31 := \nu21$$

$$G23 := \frac{E2}{2 \cdot (1 + \nu23)}$$

$$Y := \frac{1}{1 - \nu12 \cdot \nu21 - \nu23 \cdot \nu32 - \nu31 \cdot \nu13 - 2 \cdot \nu21 \cdot \nu32 \cdot \nu13}$$

Stiffness Parameters (Abaqus Guide):

$$D1111 := E1 \cdot (1 - \nu23 \cdot \nu32) \cdot Y \quad D1111 = 4.409 \times 10^{10}$$

$$D2222 := E2 \cdot (1 - \nu13 \cdot \nu31) \cdot Y \quad D2222 = 1.08 \times 10^{10}$$

$$D3333 := E3 \cdot (1 - \nu12 \cdot \nu21) \cdot Y \quad D3333 = 1.08 \times 10^{10}$$

$$D1122 := E1 \cdot (\nu21 + \nu31 \cdot \nu23) \cdot Y \quad D1122 = 4.047 \times 10^9$$

$$D1133 := E1 \cdot (\nu31 + \nu21 \cdot \nu32) \cdot Y \quad D1133 = 4.047 \times 10^9$$

$$D2233 := E2 \cdot (\nu32 + \nu12 \cdot \nu31) \cdot Y \quad D2233 = 3.5 \times 10^9$$

$$D1212 := G12 \quad D1212 = 3.51 \times 10^9$$

$$D1313 := G13 \quad D1313 = 3.51 \times 10^9$$

$$D2323 := G23 \quad D2323 = 3.65 \times 10^9$$

E-Glass Properties: 811 K

$$E1 := 4.68 \cdot 10^{10}$$

$$E2 := 9.56 \cdot 10^9$$

$$E3 := 9.56 \cdot 10^9$$

$$G12 := 3.54 \cdot 10^9$$

$$G13 := G12$$

$$\nu12 := .272$$

$$\nu23 := .3 \quad \text{estimate, set such that material properties agree with other sources}$$

$$\nu13 := .272$$

$$\nu21 := \nu12 \cdot \frac{E2}{E1}$$

$$\nu32 := \nu23$$

$$\nu31 := \nu21$$

$$G23 := \frac{E2}{2 \cdot (1 + \nu23)}$$

$$Y := \frac{1}{1 - \nu12 \cdot \nu21 - \nu23 \cdot \nu32 - \nu31 \cdot \nu13 - 2 \cdot \nu21 \cdot \nu32 \cdot \nu13}$$

Stiffness Parameters (Abaqus Guide):

$$D1111 := E1 \cdot (1 - \nu23 \cdot \nu32) \cdot Y \quad D1111 = 4.891 \times 10^{10}$$

$$D2222 := E2 \cdot (1 - \nu13 \cdot \nu31) \cdot Y \quad D2222 = 1.081 \times 10^{10}$$

$$D3333 := E3 \cdot (1 - \nu12 \cdot \nu21) \cdot Y \quad D3333 = 1.081 \times 10^{10}$$

$$D1122 := E1 \cdot (\nu21 + \nu31 \cdot \nu23) \cdot Y \quad D1122 = 3.882 \times 10^9$$

$$D1133 := E1 \cdot (\nu31 + \nu21 \cdot \nu32) \cdot Y \quad D1133 = 3.882 \times 10^9$$

$$D2233 := E2 \cdot (\nu32 + \nu12 \cdot \nu31) \cdot Y \quad D2233 = 3.46 \times 10^9$$

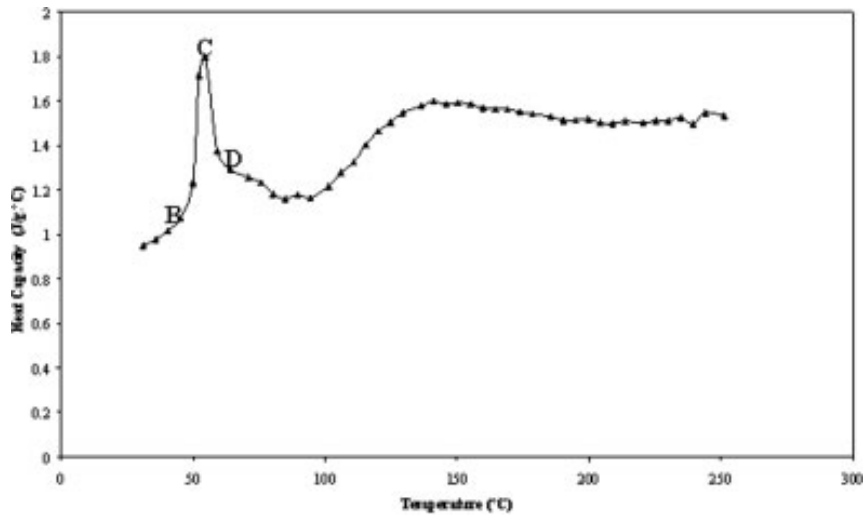
$$D1212 := G12 \quad D1212 = 3.54 \times 10^9$$

$$D1313 := G13 \quad D1313 = 3.54 \times 10^9$$

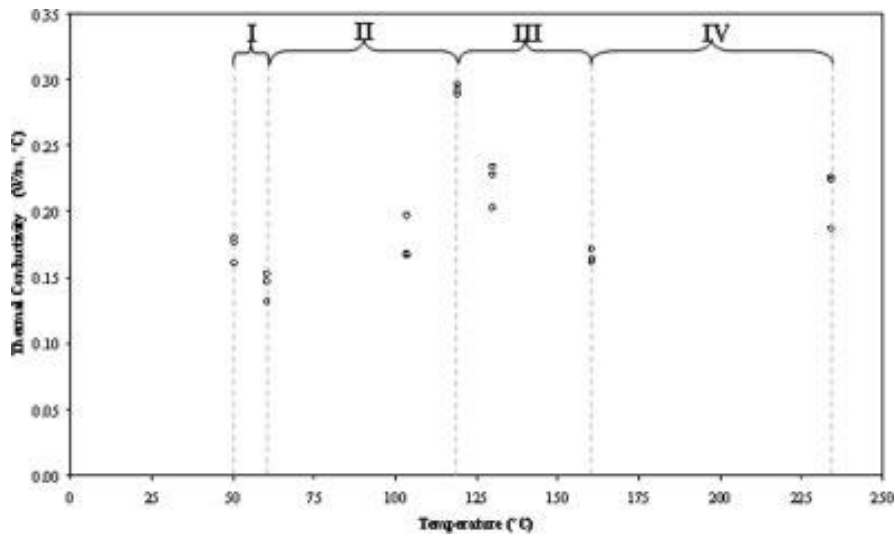
$$D2323 := G23 \quad D2323 = 3.677 \times 10^9$$

B.4. DSC Test Results for Temperature-Dependent Thermal Conductivity and Specific Heat Properties of Fiberglass-epoxy Composite

Plots from test results provided by Cecen et al. [35].



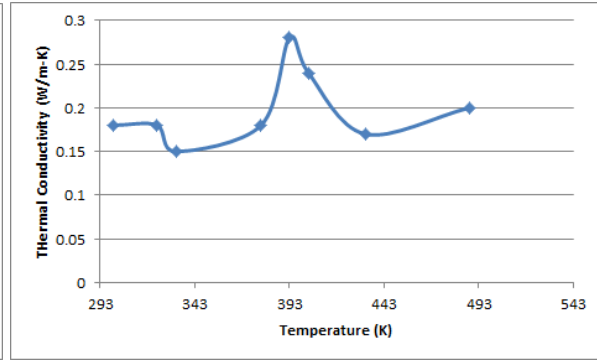
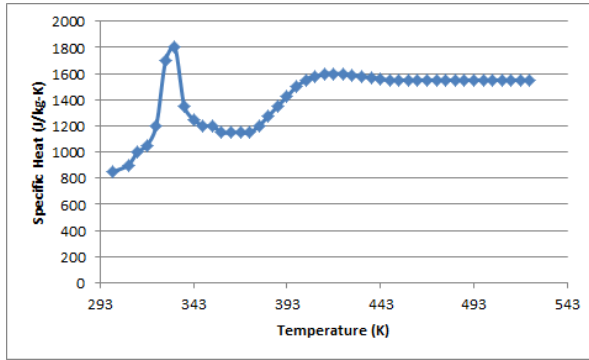
Specific heat of glass/epoxy composite material obtained from DSC experiments.



Thermal conductivity in the transverse-direction as a function of temperature for glass/epoxy composite material. Test data were averaged at each temperature point when transcribed into Excel. The Excel data points transcribed (and input into Abaqus) are:

Specific Heat	[J/kg-K]
Temperature, K	Cp
300	850
308	900
313	1000
318	1050
323	1200
328	1700
333	1800
338	1350
343	1250
348	1200
353	1200
358	1150
363	1150
368	1150
373	1150
378	1200
383	1275
388	1350
393	1425
398	1500
403	1550
408	1575
413	1600
418	1600
423	1600
428	1590
433	1580
438	1570
443	1560
448	1550
453	1550
458	1550
463	1550
468	1550
473	1550
478	1550
483	1550
488	1550
493	1550
498	1550
503	1550
508	1550
513	1550
518	1550
523	1550

Transverse Thermal Co [W/m-K]		
Temperature, K	k	
300	0.18	
323	0.18	
333	0.15	
378	0.18	
393	0.28	
403	0.24	
433	0.17	
488	0.2	



B.5. Calculation of Thermal Conductivity of Fiberglass-epoxy Composite in the Fiber-direction

The following MathCAD code shows the calculation of the fiber-direction thermal conduction for E-glass composite [35].

$$V_f := .55 \quad \text{volume fraction of glass fiber} = 55\% \quad \text{Typical volume fraction for E-glass composite}$$

$$V_m := 1 - V_f \quad \text{volume fraction of epoxy matrix} = 45\%$$

Thermal Conductivity:

$$k_f := 1.03 \cdot \frac{\text{W}}{\text{m} \cdot \text{K}} \quad \text{Thermal conductivity of fiber in W/mK}$$

$$k_m := .049 \cdot \frac{\text{W}}{\text{m} \cdot \text{K}} \quad \text{Thermal conductivity of matrix in W/mK}$$

$$k_1 := k_f \cdot V_f + V_m \cdot k_m \quad k_1 = 0.589 \cdot \frac{\text{W}}{\text{m} \cdot \text{K}}$$

B.6. Volume Fraction Calculations for E-glass Composite Elastic Material Properties

The following MathCAD code shows the calculations for elastic properties for E-glass composite [37], [38], [34].

Fiber volume fraction of 55%
 1 - fiber direction, 2 - transverse direction

At 300 K:

$$V_f := .55 \quad \text{volume fraction of glass fiber} = 55\% \quad \text{Typical volume fraction for E-glass composite}$$

$$V_m := 1 - V_f \quad \text{volume fraction of epoxy matrix} = 45\%$$

Modulus of Elasticity of fiber and epoxy matrix:

$$E_f := 72.3\text{-GPa} \quad \text{fiber modulus in GPa} \quad \nu_f := .22 \quad \text{fiber Poisson's ratio}$$

$$E_m := 4.6\text{-GPa} \quad \text{matrix modulus in GPa} \quad \nu_m := .36 \quad \text{matrix Poisson's ratio}$$

Find the effective properties of unidirectional composite.

Modulus of Elasticity:

$$E_1 := E_f \cdot V_f + E_m \cdot V_m \quad \boxed{E_1 = 41.835\text{-GPa}}$$

$$E_2 := \frac{E_m}{\left[V_f \cdot \left(\frac{E_m}{E_f} - 1 \right) + 1 \right]} \quad \boxed{E_2 = 9.485\text{-GPa}}$$

Poisson's Ratio:

$$\nu_{12} := V_f \cdot \nu_f + V_m \cdot \nu_m \quad \boxed{\nu_{12} = 0.283} \quad \text{Poisson's ratio of the composite}$$

Shear Modulus:

$$G_f := \frac{E_f}{2 \cdot (1 + \nu_f)} \quad G_f = 29.631\text{-GPa} \quad \text{Shear Modulus of fiber in GPa}$$

$$G_m := \frac{E_m}{2 \cdot (1 + \nu_m)} \quad G_m = 1.691\text{-GPa} \quad \text{Shear Modulus of matrix in GPa}$$

$$G_{12} := \frac{1}{\left(\frac{1}{G_f} \cdot V_f + \frac{1}{G_m} \cdot V_m \right)} \quad \boxed{G_{12} = 3.513\text{-GPa}} \quad \text{Shear Modulus of composite in GPa}$$

At 811 K:

Modulus of Elasticity of fiber and epoxy matrix (assume epoxy properties are constant):

$$E_f := 81.3\text{-GPa} \quad \text{fiber modulus in GPa} \quad \nu_f := .2 \quad \text{fiber Poisson's ratio}$$

$$E_m := 4.6\text{-GPa} \quad \text{matrix modulus in GPa} \quad \nu_m := .36 \quad \text{matrix Poisson's ratio}$$

Find the effective properties of unidirectional composite.

Modulus of Elasticity:

$$E_1 := E_f \cdot V_f + E_m \cdot V_m \quad E_1 = 46.785\text{-GPa}$$

$$E_2 := \frac{E_m}{\left[V_f \cdot \left(\frac{E_m}{E_f} - 1 \right) + 1 \right]} \quad E_2 = 9.561\text{-GPa}$$

Poisson's Ratio:

$$\nu_{12} := V_f \cdot \nu_f + V_m \cdot \nu_m \quad \nu_{12} = 0.272 \quad \text{Poisson's ratio of the composite}$$

Shear Modulus:

$$G_f := \frac{E_f}{2 \cdot (1 + \nu_f)} \quad G_f = 33.875\text{-GPa} \quad \text{Shear Modulus of fiber in GPa}$$

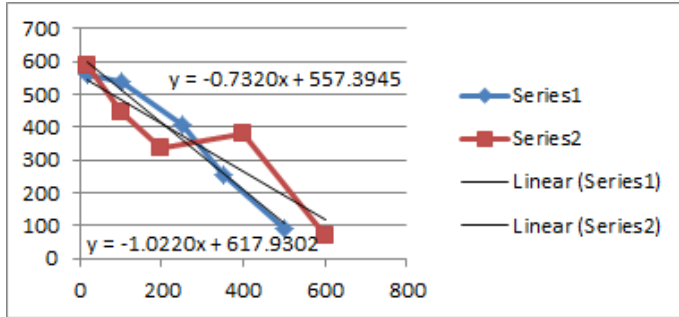
$$G_m := \frac{E_m}{2 \cdot (1 + \nu_m)} \quad G_m = 1.691\text{-GPa} \quad \text{Shear Modulus of matrix in GPa}$$

$$G_{12} := \frac{1}{\left(\frac{1}{G_f} \cdot V_f + \frac{1}{G_m} \cdot V_m \right)} \quad G_{12} = 3.542\text{-GPa} \quad \text{Shear Modulus of composite in GPa}$$

B.7. Directional Material Strength Using Normalized Test Data

Test data from two fiber size material samples were averaged out in Excel, to get one linear equation as a function of temperature [39].

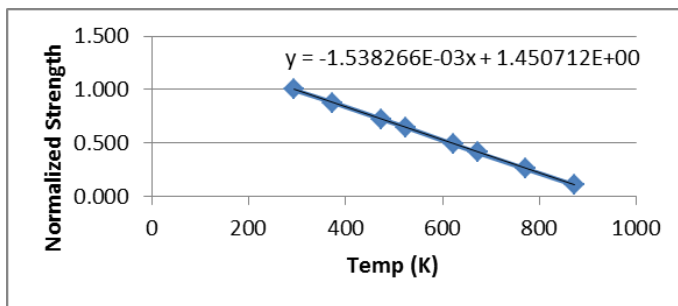
GFRP Test Data	GFRP Size 1					GFRP Size 2				
	temp [C]	Data 1	Data 2	Data 3	Avg	temp [C]	Mpa	Mpa	Mpa	Avg
	20	561.95	560.49		561.22	20	608.56	572.81	578.5	586.6233
	100	559.04	511.85		535.445	100	436.72	457.84		447.28
	250	398.59	410.93		404.76	200	331.5	340.44		335.97
	350	286.78	257.01	215.63	253.14	400	371.73	387.7		379.715
	500	114.71	61.71		88.21	600	132.86	9.44		71.15



Both equations were used at the same temperature intervals to create a single set of averaged data as a function of temperature:

temp [C]	MPa1	MPa2	avg
20	597.4902	542.7545	570.12235
100	515.7302	484.1945	499.96235
200	413.5302	410.9945	412.26235
250	362.4302	374.3945	368.41235
350	260.2302	301.1945	280.71235
400	209.1302	264.5945	236.86235
500	106.9302	191.3945	149.16235
600	4.7302	118.1945	61.46235

Dividing by the strength at room temperature, we come up with a normalized equation for material strength as a function of temperature:



Apply room temperature material strengths to the normalized yield strength equation, obtaining directional E-glass yield strengths as functions of temperature [34].

Temp [C]	Temp [K]	Temp (Abq ten	Normalized Strengl	Fiber Tensile [F	Transverse Ter	Fiber Compr	Transverse C	Shear 1-2
20	293	-7	1.000E+00	1.080E+09	3.900E+07	6.200E+08	1.280E+08	89000006
100	373	73	8.769E-01	9.471E+08	3.420E+07	5.437E+08	1.122E+08	78047552
200	473	173	7.231E-01	7.810E+08	2.820E+07	4.483E+08	9.256E+07	64356984
250	523	223	6.462E-01	6.979E+08	2.520E+07	4.006E+08	8.271E+07	57511700
350	623	323	4.924E-01	5.318E+08	1.920E+07	3.053E+08	6.302E+07	43821133
400	673	373	4.155E-01	4.487E+08	1.620E+07	2.576E+08	5.318E+07	36975849
500	773	473	2.616E-01	2.826E+08	1.020E+07	1.622E+08	3.349E+07	23285282
600	873	573	1.078E-01	1.164E+08	4.204E+06	6.684E+07	1.380E+07	9594715
650	923	623	3.089E-02	3.336E+07	1.205E+06	1.915E+07	3.954E+06	2749431
670	943	643	1.272E-04	1.373E+05	4.959E+03	7.884E+04	1.628E+04	11317.42
671	944	644	0.000E+00	0.000E+00	0.000E+00	0.000E+00	0.000E+00	0
700	973	673	0.000E+00	0.000E+00	0.000E+00	0.000E+00	0.000E+00	0
850	1123	823	0.000E+00	0.000E+00	0.000E+00	0.000E+00	0.000E+00	0
1000	1273	973	0.000E+00	0.000E+00	0.000E+00	0.000E+00	0.000E+00	0
1100	1373	1073	0.000E+00	0.000E+00	0.000E+00	0.000E+00	0.000E+00	0
1227	1500	1200	0.000E+00	0.000E+00	0.000E+00	0.000E+00	0.000E+00	0
Function:	(Yield strength at RM)*(-1.538266*10^-3*(Temp in K) + 1.450712) if under 943 K							
	0 if over 943 K							

Appendix C: Abaqus Thermomechanical Plate Model

C.1. Thermomechanical Plate Segment – Direct Lightning Strike to E-glass Composite Material

Abaqus input file for thermomechanical plate without a copper lightning protection receptor representing a direct lightning strike to fiberglass composite blade surface (abridged to save room – eliminated listing every node).

```
*Heading
** Job name: EEbigtiny1 Model name: Model-2-big-2
** Generated by: Abaqus/CAE 6.11-2
*Preprint, echo=NO, model=NO, history=NO, contact=NO
** PARTS
*Part, name=Part-1
*Node
    1,    0.,    0.,    0.
    2, 0.00707106758, 0.00707106758,    0.
CODE ABRIDGED TO REMOVE ALL NODES TO SAVE ROOM
** Section: Plate
*Solid Section, elset=_I2, orientation=Ori-3, material=EGlass0,
*Orientation, name=Ori-1
1., 0., 0., 0., 1., 0.
1, 0.
** Region: (Plate:Picked), (Material Orientation:Picked)
*Elset, elset=_I3, internal, generate
31903, 37219,    1
** Section: Plate
*Solid Section, elset=_I3, orientation=Ori-1, material=EGlass0,
** Section: UD
*Solid Section, elset=_PickedSet72, orientation=Ori-1, material=T300-nostress0,
*End Part
** ASSEMBLY
*Assembly, name=Assembly
*Instance, name=Part-1-1, part=Part-1
*End Instance
*Nset, nset=_PickedSet26, internal, instance=Part-1-1
31,
*Nset, nset=_PickedSet29, internal, instance=Part-1-1
```

```

32,
*Nset, nset=_PickedSet30, internal, instance=Part-1-1
30,
*Elset, elset=__PickedSurf32_S1, internal, instance=Part-1-1, generate
  1, 2475,  1
*Surface, type=ELEMENT, name=_PickedSurf32, internal
__PickedSurf32_S1, S1
*End Assembly
*Amplitude, name=Amp-1
  0., 0.33, 2.5e-05, 0.29, 4.5e-05, 0.09, 5e-05, 0.001
  0.0001, 1e-10, 0.00015, 1e-10, 0.0002, 1e-10
** MATERIALS
*Material, name=EGlass0
*Conductivity, type=ORTHO
0.589, 0.18, 0.18, 0.
0.589, 0.18, 0.18, 23.
0.589, 0.15, 0.15, 33.
0.589, 0.18, 0.18, 78.
0.589, 0.28, 0.28, 93.
0.589, 0.24, 0.24, 103.
0.589, 0.17, 0.17, 133.
0.589, 0.2, 0.2, 188.
*Density
2100.,
*Elastic, type=ORTHOTROPIC
4.409e+10, 4.047e+09, 1.08e+10, 4.047e+09, 3.5e+09, 1.08e+10, 3.51e+09, 3.51e+09
3.65e+09, 0.
4.891e+10, 3.882e+09, 1.081e+10, 3.882e+09, 3.46e+09, 1.081e+10, 3.54e+09, 3.54e+09
3.677e+09, 511.
*Expansion, type=ORTHO
7e-06, 2.1e-05, 2.1e-05
*Specific Heat
850., 0.
900., 8.
1000., 13.
1050., 18.
1200., 23.
1700., 28.
1800., 33.
1350., 38.
1250., 43.
1200., 48.
1200., 53.

```

1150., 58.
1150., 63.
1150., 68.
1150., 73.
1200., 78.
1275., 83.
1350., 88.
1425., 93.
1500., 98.
1550.,103.
1575.,108.
1600.,113.
1600.,118.
1600.,123.
1590.,128.
1580.,133.
1570.,138.
1560.,143.
1550.,148.
1550.,153.
1550.,158.
1550.,163.
1550.,168.
1550.,173.
1550.,178.
1550.,183.
1550.,188.
1550.,193.
1550.,198.
1550.,203.
1550.,208.
1550.,213.
1550.,218.
1550.,223.
*Material, name=T300-nostress0
*Conductivity, type=ORTHO
80.5, 7.09, 7.09
*Density
1500.,
*Elastic, type=ORTHOTROPIC
1.502e+11, 5.328e+09, 1.269e+10, 5.328e+09, 5.189e+09, 1.269e+10, 3.687e+10, 3.687e+10
3.75e+09, 0.
1.577e+11, 3.916e+09, 1.367e+10, 3.916e+09, 5.526e+09, 1.367e+10, 5.887e+10, 5.887e+10

```

4.071e+09, 100.
*Expansion, type=ORTHO
-8e-07, 0.000108, 0.000108, 0.
8.4e-06, 0.00277, 0.000277, 100.
*Specific Heat
1500.,
** PHYSICAL CONSTANTS
*Physical Constants, absolute zero=-300., stefan boltzmann=5.67e-08
** BOUNDARY CONDITIONS
** Name: BC-1 Type: Symmetry/Antisymmetry/Encastre
*Boundary
_PickedSet26, PINNED
** Name: BC-3 Type: Displacement/Rotation
*Boundary
_PickedSet29, 2, 2
_PickedSet29, 3, 3
** Name: BC-4 Type: Displacement/Rotation
*Boundary
_PickedSet30, 3, 3
** -----
** STEP: Lightning
*Step, name=Lightning, inc=10
*Coupled Temperature-displacement, creep=none, deltmx=3000.
5e-05, 0.0002, 2e-09, 0.0002
** LOADS
** Name: Load-1 Type: Surface heat flux
*Dflux, amplitude=Amp-1
_PickedSurf32, S, 4.593e+10
** OUTPUT REQUESTS
*Restart, write, frequency=0
*Print, solve=NO
** FIELD OUTPUT: F-Output-1
*Output, field
*Node Output
COORD, NT, U, UR
*Element Output, directions=YES
NFLUX, S, TEMP
*Output, history, frequency=0
*End Step
** -----
** STEP: After
*Step, name=After
*Coupled Temperature-displacement, creep=none, deltmx=4000.

```

```

0.01, 10., 1e-05, 1.
** LOADS
** Name: Load-1 Type: Surface heat flux
*Dflux
_PickedSurf32, S, 0.
** OUTPUT REQUESTS
*Restart, write, frequency=0
** FIELD OUTPUT: F-Output-1
*Output, field
*Node Output
COORD, NT, U, UR
*Element Output, directions=YES
NFLUX, S, TEMP
*Output, history, frequency=0
*End Step

```

C.2. Thermomechanical Plate Segment – Lightning Strike to Copper Lightning Protection Receptor

Abaqus input file for thermomechanical plate with a copper lightning receptor (abridged to save room – eliminated listing every single node).

```

*Heading
** Job name: CuEbig1 Model name: Model-2-big-2
** Generated by: Abaqus/CAE 6.11-2
*Preprint, echo=NO, model=NO, history=NO, contact=NO
** PARTS
*Part, name=Part-1
*Node
1, 0.00707106758, 0.00707106758, 0.
CODE ABRIDGED TO REMOVE ALL NODES TO SAVE ROOM
** Section: Plate
*Solid Section, elset=_I2, orientation=Ori-4, material=EGlass0,
*Orientation, name=Ori-2
1., 0., 0., 0., 1., 0.
1, 0.
** Region: (Plate:Picked), (Material Orientation:Picked)

```

```

*Elset, elset=_I3, internal, generate

11110, 14812, 1

** Section: Plate

*Solid Section, elset=_I3, orientation=Ori-2, material=EGlass0,

** Section: UD

*Solid Section, elset=_PickedSet62, orientation=Ori-2, material=T300-nostress0,

*Orientation, name=Ori-1

1., 0., 0., 0., 1., 0.

1, 0.

** Section: Puck

*Solid Section, elset=_PickedSet55, orientation=Ori-1, material=Copper0,

*End Part

** ASSEMBLY

*Assembly, name=Assembly

*Instance, name=Part-1-1, part=Part-1

*End Instance

*Nset, nset=_PickedSet25, internal, instance=Part-1-1

36,

*Nset, nset=_PickedSet28, internal, instance=Part-1-1

37,

*Nset, nset=_PickedSet29, internal, instance=Part-1-1

35,

*Elset, elset=__PickedSurf31_S2, internal, instance=Part-1-1, generate

51843, 55366, 1

*Surface, type=ELEMENT, name=_PickedSurf31, internal

__PickedSurf31_S2, S2

*End Assembly

*Amplitude, name=Amp-1

0., 0.95, 6.5e-05, 0.95, 7.5e-05, 0.95, 8e-05, 0.925

0.0001, 0.925, 0.000114, 0.925, 0.000116, 0.89, 0.00012, 0.15

0.000135, 0.009, 0.00017, 0.0001, 0.0002, 0.0002

** MATERIALS

*Material, name=Copper0

*Conductivity

```

401., -27.
398., 0.
372., 400.
357., 700.
335.13, 950.
331.71, 1000.
329.37, 1056.
*Density
8930., -7.
7940., 1056.
7924., 1073.
7846., 1173.
7764., 1273.
*Elastic
1.29e+11, 0.343, -7.
1.25e+11, 0.343, 73.
1.14e+11, 0.343, 293.
1.07e+11, 0.343, 440.
1e+11, 0.343, 573.
*Expansion
1.64e-05, -7.
1.64e-05, 73.
1.85e-05, 223.
2.02e-05, 423.
2.48e-05, 898.
2.63e-05, 1056.
*Latent Heat
205000., 1056., 1070.
*Specific Heat
385., 0.
398., 100.
417., 300.
432., 500.
451., 700.

506.,1000.

*Material, name=EGlass0

*Conductivity, type=ORTHO

0.589, 0.18, 0.18, 0.

0.589, 0.18, 0.18, 23.

0.589, 0.15, 0.15, 33.

0.589, 0.18, 0.18, 78.

0.589, 0.28, 0.28, 93.

0.589, 0.24, 0.24, 103.

0.589, 0.17, 0.17, 133.

0.589, 0.2, 0.2, 188.

*Density

2100.,

*Elastic, type=ORTHOTROPIC

4.409e+10, 4.047e+09, 1.08e+10, 4.047e+09, 3.5e+09, 1.08e+10, 3.51e+09, 3.51e+09

3.65e+09, 0.

4.891e+10, 3.882e+09, 1.081e+10, 3.882e+09, 3.46e+09, 1.081e+10, 3.54e+09, 3.54e+09

3.677e+09, 511.

*Expansion, type=ORTHO

7e-06, 2.1e-05, 2.1e-05

*Specific Heat

850., 0.

900., 8.

1000., 13.

1050., 18.

1200., 23.

1700., 28.

1800., 33.

1350., 38.

1250., 43.

1200., 48.

1200., 53.

1150., 58.

1150., 63.

1150., 68.
1150., 73.
1200., 78.
1275., 83.
1350., 88.
1425., 93.
1500., 98.
1550.,103.
1575.,108.
1600.,113.
1600.,118.
1600.,123.
1590.,128.
1580.,133.
1570.,138.
1560.,143.
1550.,148.
1550.,153.
1550.,158.
1550.,163.
1550.,168.
1550.,173.
1550.,178.
1550.,183.
1550.,188.
1550.,193.
1550.,198.
1550.,203.
1550.,208.
1550.,213.
1550.,218.
1550.,223.

*Material, name=PVCFoam

*Conductivity

0.032,

*Density

150.,

*Elastic

1.28e+08, 0.32

*Expansion

3.5e-05,

*Specific Heat

1500.,

*Material, name=T300-nostress0

*Conductivity, type=ORTHO

80.5, 7.09, 7.09

*Density

1500.,

*Elastic, type=ORTHOTROPIC

1.502e+11, 5.328e+09, 1.269e+10, 5.328e+09, 5.189e+09, 1.269e+10, 3.687e+10, 3.687e+10

3.75e+09, 0.

1.577e+11, 3.916e+09, 1.367e+10, 3.916e+09, 5.526e+09, 1.367e+10, 5.887e+10, 5.887e+10

4.071e+09, 100.

*Expansion, type=ORTHO

-8e-07, 0.000108, 0.000108, 0.

8.4e-06, 0.00277, 0.000277, 100.

*Specific Heat

1500.,

** PHYSICAL CONSTANTS

*Physical Constants, absolute zero=-300., stefan boltzmann=5.67e-08

** BOUNDARY CONDITIONS

** Name: BC-2 Type: Symmetry/Antisymmetry/Encastre

*Boundary

_PickedSet25, PINNED

** Name: BC-3 Type: Displacement/Rotation

*Boundary

_PickedSet28, 2, 2

_PickedSet28, 3, 3

```

** Name: BC-4 Type: Displacement/Rotation

*Boundary
_PickedSet29, 3, 3

** -----

** STEP: Lightning

*Step, name=Lightning

*Coupled Temperature-displacement, creep=none, deltmx=3000.
0.0002, 0.0002, 2e-07, 0.0002

** LOADS

** Name: Load-1 Type: Surface heat flux

*Dflux, amplitude=Amp-1
_PickedSurf31, S, 4.593e+10

** OUTPUT REQUESTS

*Restart, write, frequency=0

*Print, solve=NO

** FIELD OUTPUT: F-Output-1

*Output, field

*Node Output

NT, U, UR

*Element Output, directions=YES

NFLUX, S, TEMP

*Output, history, frequency=0

*End Step

** -----

** STEP: After

*Step, name=After, inc=450

*Coupled Temperature-displacement, creep=none, deltmx=500.
0.001, 0.5, 2e-06, 0.02

** LOADS

** Name: Load-1 Type: Surface heat flux

*Dflux

_PickedSurf31, S, 0.

** OUTPUT REQUESTS

*Restart, write, frequency=0

```

** FIELD OUTPUT: F-Output-1

*Output, field

*Node Output

COORD, NT, U, UR

*Element Output, directions=YES

NFLUX, S, TEMP

*Output, history, frequency=0

*End Step

C.3. Example Material Strength Calculation

The following excel logic is used to calculate material strength and whether or not a material yields at a particular node.

z	Radius (m)	Temp (K)	VonMises	S11 (neg)	S22 (neg)	S12 (neg)	S11 (Pa)	S22 (Pa)	S12 (Pa)	Strength (Fib-	Strength (Tr	Strength (St	Yield?
0.00E+00	1.00E-02	6.01E+02	1.99E+08	-1.93E+08	-3.92E+06	3.46E+06	1.93E+08	3.92E+06	3.46E+06	3.27E+08	6.74E+07	4.69E+07	0

Z, Radius (m), Temp (K), VonMises: readouts from Abaqus for the specific node in question

S11(neg): S11 value at this particular node, pulled from Abaqus output: is positive if in tension, negative in compression

S22(neg): S22 value at this particular node, pulled from Abaqus output: is positive if in tension, negative in compression

S12(neg): S12 value at this particular node, pulled from Abaqus output: is positive if in tension, negative in compression

S11 (Pa): takes the absolute value of S11 to compare back to strength to determine yielding
=IF("S11(neg)"<0,-1*"S11(neg)", "S11(neg)",) - ensures S11 (Pa) is a positive value

S22 (Pa): takes the absolute value of S22 to compare back to strength to determine yielding
=IF("S22(neg)"<0,-1*"S22(neg)", "S22(neg)",) - ensures S22 (Pa) is a positive value

S12 (Pa): takes the absolute value of S12 to compare back to strength to determine yielding
=IF("S12(neg)"<0,-1*"S12(neg)", "S12(neg)",) - ensures S12 (Pa) is a positive value

Strength (Fib-Direction): calculates fiber-direction strength, to be compared with the S11 value of stress. Function of temperature Temp (K). Has to use one function for tension, and one function for compression, which is determined by the sign of S11.

=IF("Temp (K)"<943,IF("S11(neg)">=0,1.08*10^9*(-1.538266*10^-3*"Temp (K)" +1.450712),6.2*10^8*(-1.538266*10^-3*"Temp (K)" +1.450712)),0) – If temp is below 943 K (temperatures higher than this result in zero material strength), then perform the calculation: IF

the stress is tensile, calculate with tensile strength equation (function of temp), and IF stress is compressive, calculate with a compression strength equation (function of temp).

Strength (Transv-Dir): calculates transverse-direction strength, to be compared with the S22 value of stress. Function of temperature Temp (K). Has to use one function for tension, and one function for compression, which is determined by the sign of S22.

=IF("Temp (K)"<943,IF("S22(neg)">=0,1.08*10^9*(-1.538266*10^-3*"Temp (K)" +1.450712),6.2*10^8*(-1.538266*10^-3*"Temp (K)" +1.450712)),0) – If temp is below 943 K (temperatures higher than this result in zero material strength), then perform the calculation: IF the stress is tensile, calculate with tensile strength equation (function of temp), and IF stress is compressive, calculate with a compression strength equation (function of temp).

Strength (Shear): calculates shear strength, to be compared with the S12 value of stress. Function of temperature Temp (K). Has to use one function for tension, and one function for compression, which is determined by the sign of S12.

=IF("Temp (K)"<943,IF("S12(neg)">=0,1.08*10^9*(-1.538266*10^-3*"Temp (K)" +1.450712),6.2*10^8*(-1.538266*10^-3*"Temp (K)" +1.450712)),0) – If temp is below 943 K (temperatures higher than this result in zero material strength), then perform the calculation: IF the stress is tensile, calculate with tensile strength equation (function of temp), and IF stress is compressive, calculate with a compression strength equation (function of temp).

Yield?: does the material at this node yield, 1 for yes, 0 for no.

If calculating fiber-direction strength, is "S11 (Pa)" > "Strength (Fib-Direction)"

If calculating transverse-direction strength, is "S22 (Pa)" > "Strength (Transv-Dir)"

All nodes resulting in 1 plastically yield, all those with 0 do not.

Appendix D: Wind Turbine Blade FEA Design and Modal Analysis

D.1. Airfoil Node Calculations

The following shows the calculations for determining the chord length and angle of attack for each blade radius of interest (providing the equations for interpolation points).

Radius	Chord Length	Source	Angle of Attack
4.75	3.92	root	9.0
6	3.57	interpolation	8.7
7.13	3.25	provided	8.4
11.5	2.57	interpolation	7.2
16.63	1.77	provided	5.8
18.5	1.64	interpolation	5.3
21.38	1.43	provided	4.5
23.75	1.32	interpolation	3.9
26.13	1.20	provided	3.2
28.5	1.12	interpolation	2.6
30.88	1.04	provided	1.9
33.25	0.98	interpolation	1.3
35.63	0.91	provided	0.6
36.75	0.88	interpolation	0.3
38	0.85	tip	0.0
Sample interpolation equation for chord length (E3):			
$(E4-E2)/(D4-D2)*(D3-D2)+E2$			
Sample interpolation equation for angle of attack (G3):			
$(G4-G2)/(D4-D2)*(D3-D2)+G2$			

The x-y points for a NACA 64(3)-618 airfoil profile are provided [45].

NACA 64(3)-618					
Chord (x)	Height (y)				
1.00000	0.00000	0.06895	0.06312		
0.95056	0.01344	0.04417	0.05093		
0.90115	0.02646	0.01982	0.03518		
0.85161	0.03963	0.00805	0.02452		
0.80191	0.05270	0.00359	0.01885		
0.75203	0.06544	0.00150	0.01534		
0.70196	0.07754	0.00000	0.00000		
0.65171	0.08870	0.00850	-0.01234		
0.60129	0.09870	0.01141	-0.01465		
0.55071	0.10730	0.01695	-0.01810		
0.50000	0.11423	0.03018	-0.02402	0.50000	-0.04805
0.44917	0.11915	0.05583	-0.03197	0.54929	-0.04160
0.39827	0.12163	0.08105	-0.03769	0.59871	-0.03444
0.34735	0.12065	0.10605	-0.04220	0.64829	-0.02690
0.29645	0.11698	0.15573	-0.04899	0.69804	-0.01922
0.24560	0.11065	0.20514	-0.05377	0.74797	-0.01174
0.19486	0.10153	0.25440	-0.05695	0.79809	-0.00494
0.14427	0.08937	0.30355	-0.05866	0.84839	0.00075
0.09395	0.07322	0.35265	-0.05885	0.89885	0.00456
		0.40173	-0.05737	0.94944	0.00552
		0.45083	-0.05345	1.00000	0.00000

The following is an example calculation for determining the x-y points for airfoil nodes at a radius of 4.75 m in Excel.

radius:	4.75	angle of attack:	9	chord:	3.92	37.5% chord:	1.47
		from chord/angle of attack table					0.375*chord

Chord Calculation:							
(NACA x location)*(chord at this radius)-(37.5% chord length)							
(1)*(3.92)-(1.47)=2.45							
Heigh Calculation:							
(NACA y location)*(chord at this radius)							
(0)*(3.92)=0							
Abaqus x Location:							
(chord calculation)*COS(angle of attack at this radius*PI()/180)							
(2.45)*COS(9*pi/180)=2.42							
Abaqus y Location:							
(chord calculation)*SIN(angle of attack at this radius*PI()/180)+(height calculation)							
(2.45)*SIN(9*pi/180)+0=.383							

Chord	Height	x	y
2.45	0	2.419836434	0.383264
2.256195	0.052685	2.228417693	0.405631
2.062508	0.103723	2.037115104	0.426371
1.868311	0.15535	1.845309189	0.447618
1.673487	0.206584	1.652883796	0.468375
1.477958	0.256525	1.459761489	0.487728
1.281683	0.303957	1.265903553	0.504456
1.084703	0.347704	1.071348704	0.517389
0.887057	0.386904	0.876135659	0.52567
0.688783	0.420616	0.680303136	0.528365
0.49	0.447782	0.483967287	0.524434
0.290746	0.467068	0.287166829	0.512551
0.091218	0.47679	0.09009535	0.491059
-0.10839	0.472948	-0.107053564	0.455992
-0.30792	0.458562	-0.304125043	0.410393
-0.50725	0.433748	-0.501002935	0.354397
-0.70615	0.397998	-0.697454936	0.287532
-0.90446	0.35033	-0.893326177	0.208841
-1.10172	0.287022	-1.088152048	0.114676
-1.19972	0.24743	-1.184945505	0.059753
-1.29685	0.199646	-1.28088718	-0.00323
-1.39231	0.137906	-1.375164008	-0.0799

-1.43844	0.096118	-1.420734367	-0.1289
-1.45593	0.073892	-1.43800232	-0.15387
-1.46412	0.060133	-1.446094253	-0.16891
-1.47	0	-1.451901861	-0.22996
-1.43668	-0.04837	-1.418992085	-0.27312
-1.42527	-0.05743	-1.407725327	-0.28039
-1.40356	-0.07095	-1.386275897	-0.29052
-1.35169	-0.09416	-1.335052799	-0.30561
-1.25115	-0.12532	-1.235742712	-0.32104
-1.15228	-0.14774	-1.138097472	-0.328
-1.05428	-0.16542	-1.041304014	-0.33035
-0.85954	-0.19204	-0.848956056	-0.3265
-0.66585	-0.21078	-0.657653467	-0.31494
-0.47275	-0.22324	-0.466931638	-0.2972
-0.28008	-0.22995	-0.276635701	-0.27376
-0.08761	-0.23069	-0.086533351	-0.2444
0.104782	-0.22489	0.103491565	-0.2085
0.297254	-0.20952	0.293593915	-0.16302
0.49	-0.18836	0.483967287	-0.1117
0.683217	-0.16307	0.674805267	-0.05619
0.876943	-0.135	0.866146574	0.002179
1.071297	-0.10545	1.058107359	0.06214
1.266317	-0.07534	1.250726339	0.122753
1.462042	-0.04602	1.444042232	0.182693
1.658513	-0.01936	1.638093755	0.240084
1.855689	0.00294	1.832842192	0.293234
2.053492	0.017875	2.028210106	0.339112
2.251805	0.021638	2.224081346	0.373898
2.45	0	2.419836434	0.383264

D.2. Abaqus Input Template for Airoil Nodes

The following Abaqus template code is used to input node points to follow the NACA 64(3)-618 profile. The following points were updated (using the Excel calculations for a NACA 64(3)-618 airfoil profile previously shown) for each z-value. Each z-value represents a different blade radius value, with the blade hub at $r=0$ meters, the widest blade chord at $r=4.75$ meters, and a gradual decrease in chord length as the blade extends to the tip, at $r=38$ meters. The following code is an example of airfoil nodes at a blade radius of 4.75 meters.

```
# Do not delete the following import lines
from abaqus import *
from abaqusConstants import *
def Nodes():
    import section
    import regionToolset
    import displayGroupMdbToolset as dgm
```

```

import part
import material
import assembly
import step
import interaction
import load
import mesh
import job
import sketch
import visualization
import xyPlot
import displayGroupOdbToolset as dgo
import connectorBehavior

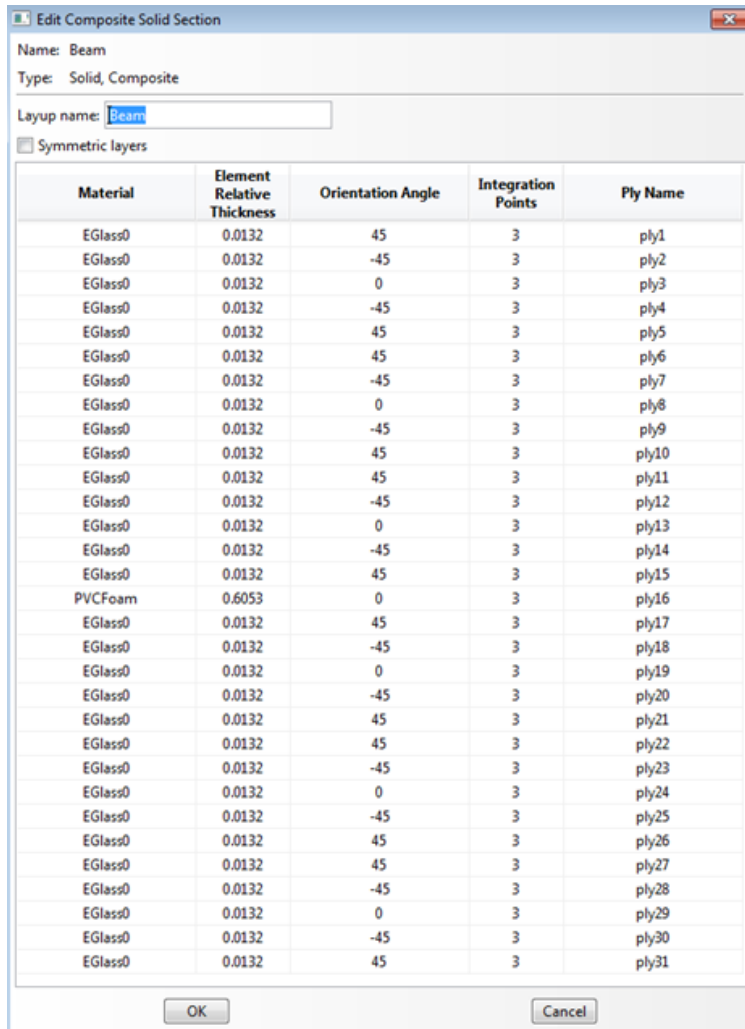
p = mdb.models['Model-1'].parts['Part-1']
p.DatumPlaneByPrincipalPlane(principalPlane=XYPLANE, offset=-4.75)
p.DatumPointByCoordinate(coords=(0.0, 0.0, -4.75))
p.DatumPointByCoordinate(coords=(-1.0, 1.0, -4.75))
p.DatumPointByCoordinate(coords=(-1.0, -1.0, -4.75))
p.DatumPointByCoordinate(coords=(2.41983643445809, 0.383264439348566, -4.75))
p.DatumPointByCoordinate(coords=(2.22841769314671, 0.405631489138337, -4.75))
p.DatumPointByCoordinate(coords=(2.0371151039842, 0.426370535621197, -4.75))
p.DatumPointByCoordinate(coords=(1.84530918884331, 0.447617863100672, -4.75))
p.DatumPointByCoordinate(coords=(1.6528837955752, 0.468375074883674, -4.75))
p.DatumPointByCoordinate(coords=(1.45976148941397, 0.487728306508144, -4.75))
p.DatumPointByCoordinate(coords=(1.26590355297667, 0.504456225743051, -4.75))
p.DatumPointByCoordinate(coords=(1.07134870364624, 0.517388964819427, -4.75))
p.DatumPointByCoordinate(coords=(0.876135658805633, 0.525670255968299, -4.75))
p.DatumPointByCoordinate(coords=(0.680303135837809, 0.528365431420698, -4.75))
p.DatumPointByCoordinate(coords=(0.483967286891617, 0.524434487869713, -4.75))
p.DatumPointByCoordinate(coords=(0.28716682935001, 0.512550757546373, -4.75))
p.DatumPointByCoordinate(coords=(0.0900953501277435, 0.491059301605826, -4.75))
p.DatumPointByCoordinate(coords=(-0.107053563860426, 0.455992381203219, -4.75))
p.DatumPointByCoordinate(coords=(-0.304125043082693, 0.410392925262672, -4.75))
p.DatumPointByCoordinate(coords=(-0.501002935390202, 0.354396930477273, -4.75))
p.DatumPointByCoordinate(coords=(-0.697454936485248, 0.287531590233199, -4.75))
p.DatumPointByCoordinate(coords=(-0.893326176836023, 0.208841433454569, -4.75))
p.DatumPointByCoordinate(coords=(-1.08815204784711, 0.114676046913737, -4.75))
p.DatumPointByCoordinate(coords=(-1.18494550522544, 0.0597534693397944, -4.75))
p.DatumPointByCoordinate(coords=(-1.28088718017883, -0.00322699915149754, -4.75))
p.DatumPointByCoordinate(coords=(-1.37516400766532, -0.0798989817085176, -4.75))
p.DatumPointByCoordinate(coords=(-1.42073436739903, -0.12890381763033, -4.75))
p.DatumPointByCoordinate(coords=(-1.43800232019533, -0.153865192669521, -4.75))
p.DatumPointByCoordinate(coords=(-1.44609425323215, -0.168906028954703, -4.75))

```

p.DatumPointByCoordinate(coords=(-1.45190186067485, -0.229958663609139, -4.75))
p.DatumPointByCoordinate(coords=(-1.41899208516622, -0.273119067233999, -4.75))
p.DatumPointByCoordinate(coords=(-1.40772532672739, -0.280389788004392, -4.75))
p.DatumPointByCoordinate(coords=(-1.38627589657235, -0.290516532014006, -4.75))
p.DatumPointByCoordinate(coords=(-1.33505279892774, -0.305609990361876, -4.75))
p.DatumPointByCoordinate(coords=(-1.23574271165758, -0.321044817771011, -4.75))
p.DatumPointByCoordinate(coords=(-1.13809747185433, -0.328001731114417, -4.75))
p.DatumPointByCoordinate(coords=(-1.041304014476, -0.330350353540475, -4.75))
p.DatumPointByCoordinate(coords=(-0.8489560559738, -0.326502229785536, -4.75))
p.DatumPointByCoordinate(coords=(-0.657653466811281, -0.314940476268396, -4.75))
p.DatumPointByCoordinate(coords=(-0.466931638393033, -0.297198706216699, -4.75))
p.DatumPointByCoordinate(coords=(-0.276635701187249, -0.273761990706328, -4.75))
p.DatumPointByCoordinate(coords=(-0.0865333508962212, -0.244397536351105, -4.75))
p.DatumPointByCoordinate(coords=(0.103491564628903, -0.208498946457941, -4.75))
p.DatumPointByCoordinate(coords=(0.293593914919931, -0.163023292102717, -4.75))
p.DatumPointByCoordinate(coords=(0.483967286891617, -0.111703112130287, -4.75))
p.DatumPointByCoordinate(coords=(0.67480526745872, -0.0561933453855017, -4.75))
p.DatumPointByCoordinate(coords=(0.86614657400419, 0.00217934036266815, -4.75))
p.DatumPointByCoordinate(coords=(1.05810735867688, 0.0621397418073112, -4.75))
p.DatumPointByCoordinate(coords=(1.25072633885974, 0.122753191179457, -4.75))
p.DatumPointByCoordinate(coords=(1.44404223193573, 0.182693020710135, -4.75))
p.DatumPointByCoordinate(coords=(1.6380937552878, 0.240083762630375, -4.75))
p.DatumPointByCoordinate(coords=(1.83284219153298, 0.293233684709148, -4.75))
p.DatumPointByCoordinate(coords=(2.02821010590539, 0.339112122484394, -4.75))
p.DatumPointByCoordinate(coords=(2.22408134625617, 0.373898279263024, -4.75))
p.DatumPointByCoordinate(coords=(2.41983643445809, 0.383264439348566, -4.75))

D.3. Abaqus Composite Layup Definitions

The following Abaqus layup definition represents a solid shear web. The 76 mm thick shear web is comprised of 30 1-mm E-glass plies and a 46 mm foam core.



The following Excel table shows the number of E-glass plies in each segment of the tapered blade root. From the root to 3 m blade length, the blade is 80 plies thick, etc. At 4.75 m (the widest airfoil chord of the blade, the materials become 10 plies of biaxial E-glass composite sandwiching a 38 mm foam core.

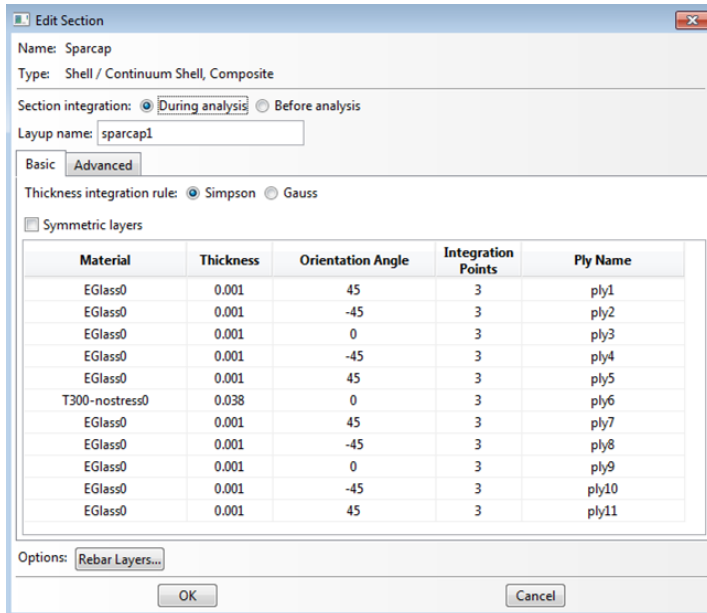
Taper in thickness from root to widest chord (4.75 m)	
Blade length [m]	Number of E-glass plies (1 mm/ply)
0	80
3	75
3.5	70
4	65
4.25	60
4.5	50
4.75	48 (10 E-glass, 38 mm foam core)

The following Excel table shows the amount of intermediate material required to “gradually taper” the blade, starting at 1/3 the blade’s length (~13 m). From the widest chord (4.75 m) until

1/3 the blade length (13 m), the intermediate thickness is 38 mm. After 13 m, the intermediate thickness decreases according to the following table.

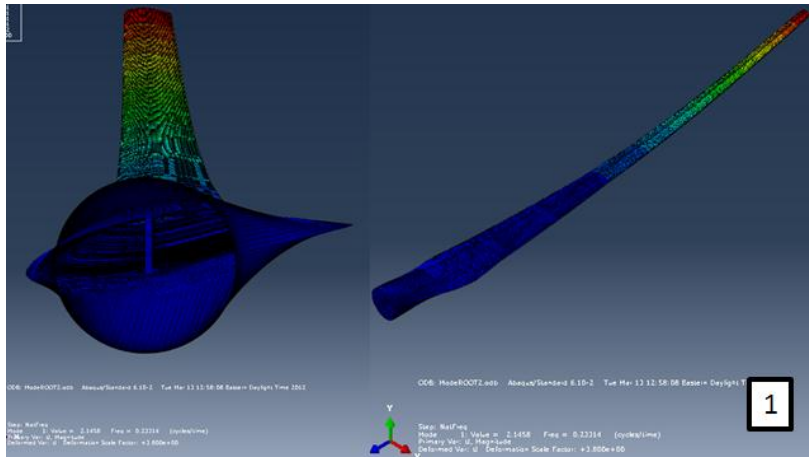
Taper in thickness from 1/3 blade length to tip			
12.66666667 Start taper from this length			
Blade length [m]	Thickness of intermediate material [mm]		
13	36		
16	32		
19	28		
22	24		
25	20		
28	16		
31	11		
34	6		
36	2		
36.75	0		

The following Abaqus layup definition represents the spar cap of the constant thickness segment of the turbine blade. The 48 mm thick spar cap is comprised of 2 5-ply ($\pm 45,0$) layups of E-glass composite material sandwiching 38 mm T300 carbon composite core. For the regular blade shell (the non-spar cap portion), the carbon composite core is replaced by an equally thick PVC foam core.

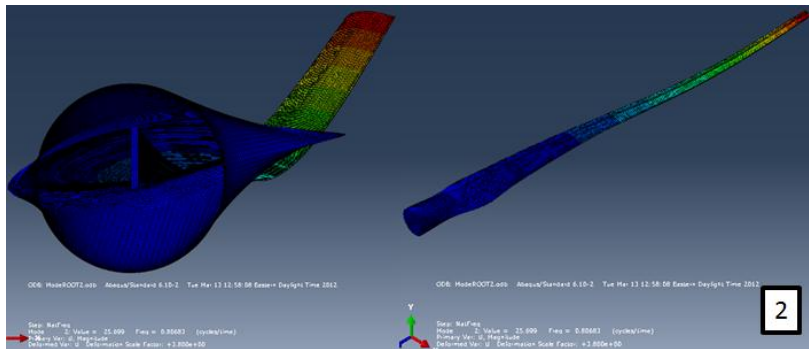


D.4. Mode Shape Images

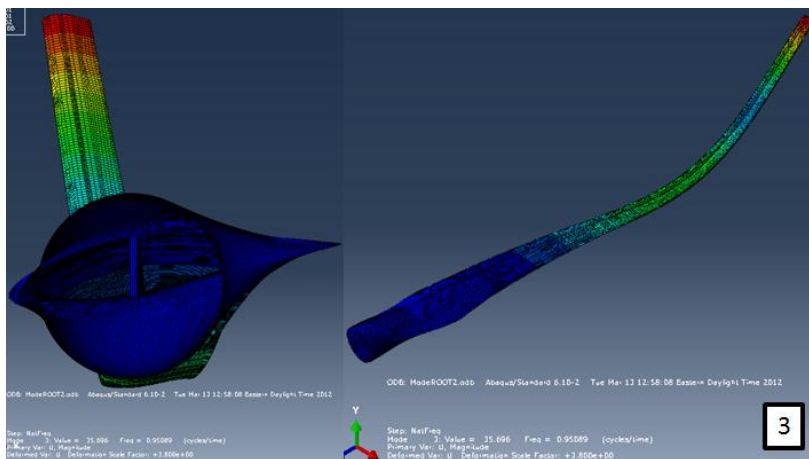
Abaqus mode shapes 1 – 10 of the turbine blade are shown below.



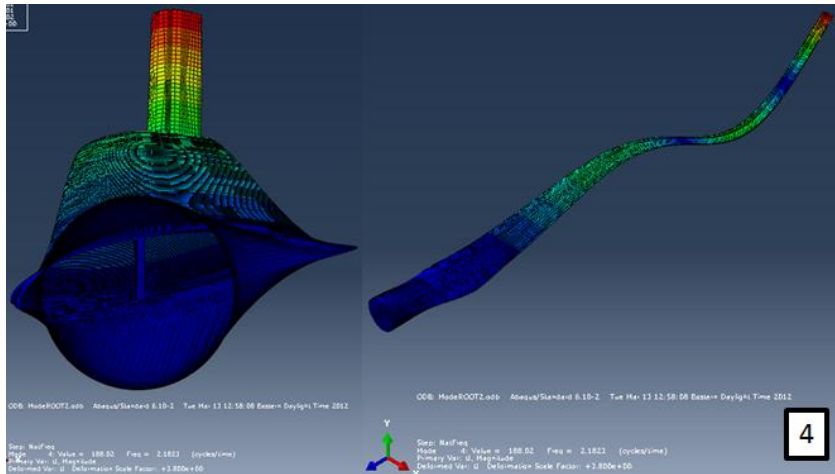
Flap-1



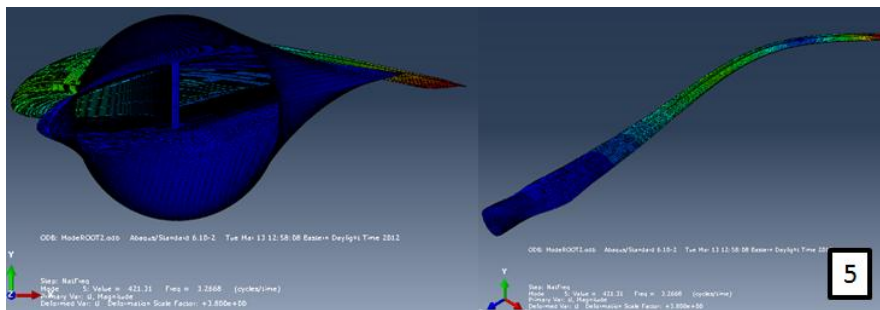
Edge-1



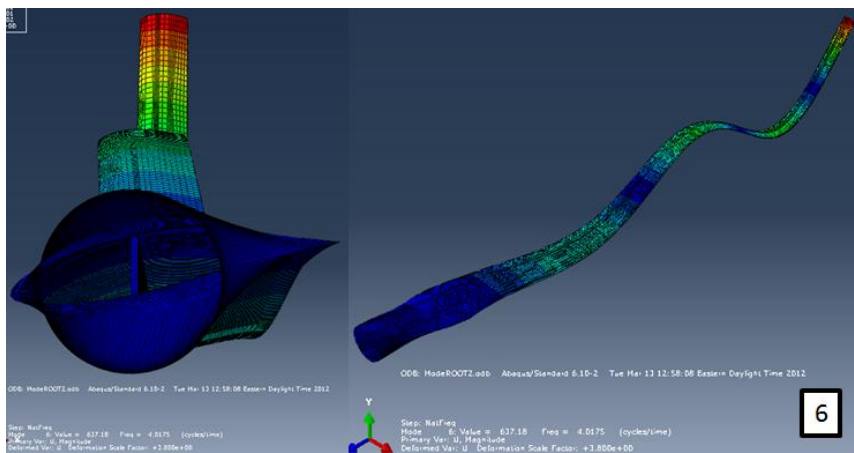
Edge-2



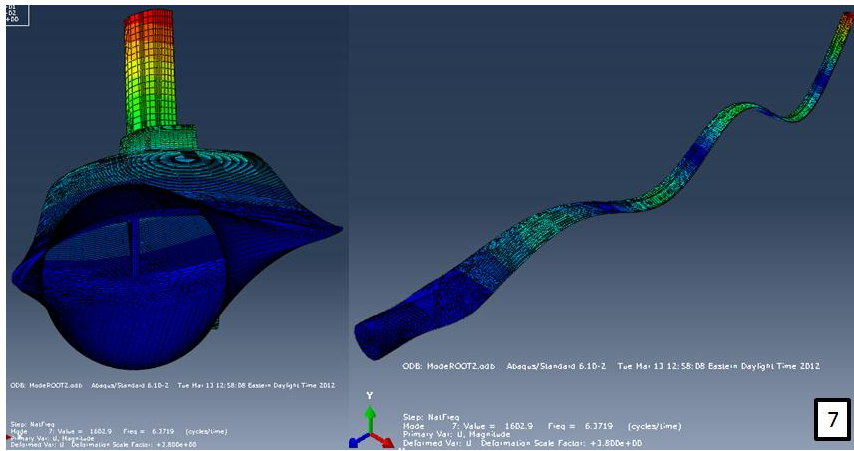
Flap-2



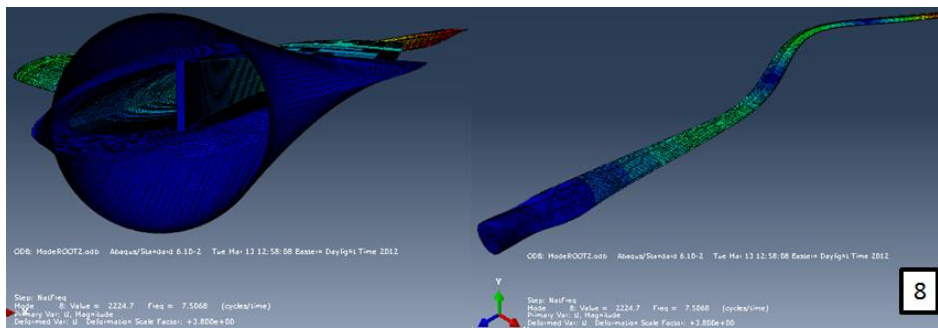
Edge-3



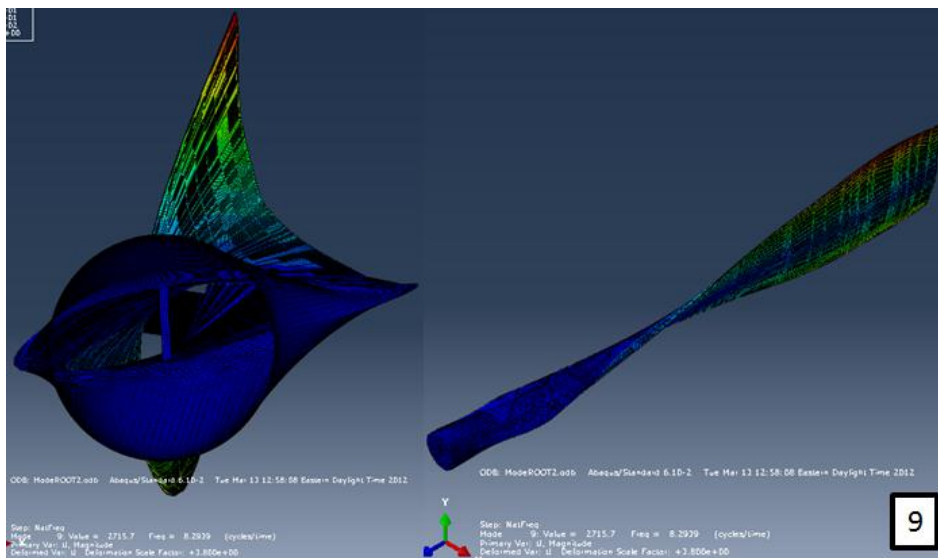
Flap-3



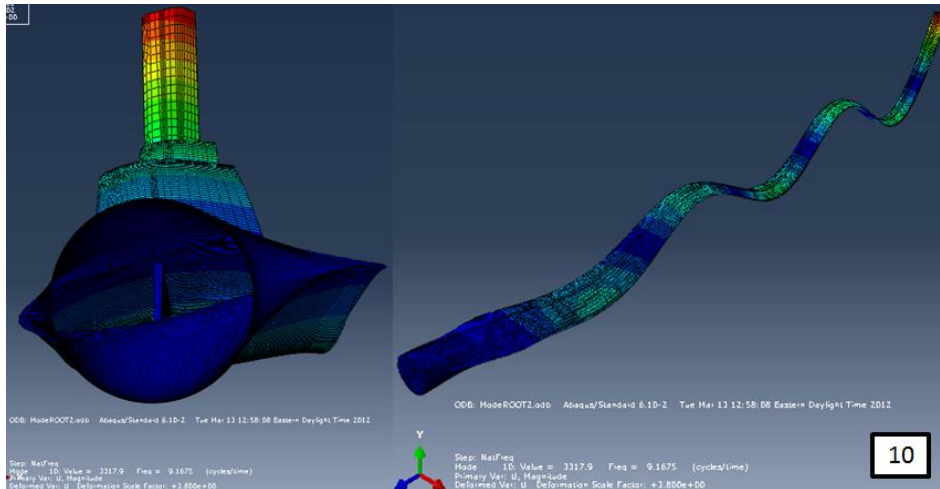
Flap-4



Edge-4



Torsion-1



Flap-5

D.5. Blade Frequency Abaqus Input File Example

The following code is the Abaqus input code to a natural frequency analysis of the turbine blade model. The node definitions are abridged to save room.

```

*Heading
** Job name: ModeRoot1 Model name: Model-1
** Generated by: Abaqus/CAE 6.10-2
*Preprint, echo=NO, model=NO, history=NO, contact=NO
** PARTS
*Part, name=Part-1
*End Part
** ASSEMBLY
*Assembly, name=Assembly
*Instance, name=Part-1-1, part=Part-1
*Node
    1, -0.0369464569, -0.0521909297,   -36.75
    2, -0.0369464569,  0.105468117,   -36.75
Nodes and picked sets are abridged to save room
*Orientation, name=Ori-3
1., 0., 0., 0., 1., 0.
2, 90.
** Section: Beam
*Solid Section, elset=_PickedSet1360, composite, orientation=Ori-3, layup=Beam
0.0132, 3, EGlass0, 45., ply1
0.0132, 3, EGlass0, -45., ply2
0.0132, 3, EGlass0, 0., ply3

```

0.0132, 3, EGlass0, -45., ply4
 0.0132, 3, EGlass0, 45., ply5
 0.0132, 3, EGlass0, 45., ply6
 0.0132, 3, EGlass0, -45., ply7
 0.0132, 3, EGlass0, 0., ply8
 0.0132, 3, EGlass0, -45., ply9
 0.0132, 3, EGlass0, 45., ply10
 0.0132, 3, EGlass0, 45., ply11
 0.0132, 3, EGlass0, -45., ply12
 0.0132, 3, EGlass0, 0., ply13
 0.0132, 3, EGlass0, -45., ply14
 0.0132, 3, EGlass0, 45., ply15
 0.6053, 3, PVCFoam, 0., ply16
 0.0132, 3, EGlass0, 45., ply17
 0.0132, 3, EGlass0, -45., ply18
 0.0132, 3, EGlass0, 0., ply19
 0.0132, 3, EGlass0, -45., ply20
 0.0132, 3, EGlass0, 45., ply21
 0.0132, 3, EGlass0, 45., ply22
 0.0132, 3, EGlass0, -45., ply23
 0.0132, 3, EGlass0, 0., ply24
 0.0132, 3, EGlass0, -45., ply25
 0.0132, 3, EGlass0, 45., ply26
 0.0132, 3, EGlass0, 45., ply27
 0.0132, 3, EGlass0, -45., ply28
 0.0132, 3, EGlass0, 0., ply29
 0.0132, 3, EGlass0, -45., ply30
 0.0132, 3, EGlass0, 45., ply31
 ** Region: (Shell:Picked), (Material Orientation:Picked)
 *Elset, elset=_I2, internal
 3853, 3854, 3855, 3856, 3857, 3858, 3859, 3860, 3861, 3862, 3863,
Material Orientations and Set Definitions are abridged to save room
 *End Assembly
 ** MATERIALS
 *Material, name=EGlass0
 *Conductivity, type=ORTHO
 3.46, 0.35, 0.35
 *Density
 2100.,
 *Elastic, type=ORTHOTROPIC
 4.404e+10, 4e+09, 1.079e+10, 4e+09, 3.492e+09, 1.079e+10, 3.51e+09, 3.51e+09
 3.65e+09,
 *Expansion, type=ORTHO

```

7e-06, 2.1e-05, 7e-06
*Specific Heat
850.,
*Material, name=PVCFoam
*Conductivity
0.032,
*Density
150.,
*Elastic
1.28e+08, 0.32
*Expansion
3.5e-05,
*Specific Heat
1500.,
*Material, name=T300-nostress0
*Conductivity, type=ORTHO
80.5, 7.09, 7.09
*Density
1500.,
*Elastic, type=ORTHOTROPIC
1.502e+11, 5.328e+09, 1.269e+10, 5.328e+09, 5.189e+09, 1.269e+10, 3.687e+10, 3.687e+10
3.75e+09, 300.
1.577e+11, 3.916e+09, 1.367e+10, 3.916e+09, 5.526e+09, 1.367e+10, 5.887e+10, 5.887e+10
4.071e+09, 400.
*Expansion, type=ORTHO, zero=300.
-8e-07, 0.000108, 0.000108, 0.
8.4e-06, 0.00277, 0.000277, 100.
*Specific Heat
1500.,
** PHYSICAL CONSTANTS
*Physical Constants, absolute zero=-300., stefan boltzmann=5.67e-08
** BOUNDARY CONDITIONS
** Name: BC-1 Type: Symmetry/Antisymmetry/Encastre
*Boundary
_PickedSet20, ENCASTRE
** -----
** STEP: NatFreq
*Step, name=NatFreq, perturbation
*Frequency, eigensolver=Lanczos, acoustic coupling=on, normalization=displacement
10, , , ,
** OUTPUT REQUESTS
*Restart, write, frequency=0
** FIELD OUTPUT: F-Output-1

```

*Output, field, variable=PRESELECT

*End Step

D.6. Blade Frequency Excel Results

The following Excel readings output from Abaqus show the analysis used to put the data into tables and plots.

Trailing Edge - Blade Tip				
Length of Seam	Mode	Eigenfreq	Eigenval	
Baseline				
0	1	0.275	2.986	
z=	2	0.938	34.727	
-38	3	1.045	43.141	
	4	2.257	201.073	
	5	3.563	501.123	
	6	4.118	669.373	
	7	6.514	1670	
	8	7.962	2500	
	9	9.161	3310	
	10	9.366	3460	
(1-inch)				
				Difference from Baseline %
0.0254	1	0.275	2.986	0.00000 %
z=	2	0.938	34.727	0.00000 %
-37.9746	3	1.045	43.141	0.00000 %
	4	2.257	201.073	0.00000 %
	5	3.563	501.123	0.00000 %
	6	4.118	669.371	0.00000 %
	7	6.514	1670	0.00031 %
	8	7.962	2500	0.00000 %
	9	9.161	3310	0.00000 %
	10	9.366	3460	0.00075 %
0.665	1	0.275	2.986	0.00000 %
z=	2	0.938	34.726	0.00000 %
-37.335	3	1.045	43.140	0.00096 %
	4	2.257	201.026	0.01152 %
	5	3.563	501.110	0.00140 %
	6	4.116	668.822	0.04104 %
	7	6.506	1670	0.10870 %
	8	7.962	2500	0.00716 %
	9	9.156	3310	0.05763 %
	10	9.342	3450	0.25645 %
1.33	1	0.275	2.986	0.00000 %
z=	2	0.938	34.723	0.00000 %
-36.67	3	1.045	43.135	0.00765 %
	4	2.255	200.793	0.06957 %
	5	3.563	501.045	0.00786 %
	6	4.108	666.115	0.24358 %
	7	6.469	1650	0.67935 %
	8	7.959	2500	0.03931 %
	9	9.081	3260	0.87313 %
	10	9.226	3360	1.49694 %

	1.995	1	0.275	2.986		0.00000	%
z=		2	0.938	34.719		0.00000	%
	-36.005	3	1.045	43.131		0.01244	%
		4	2.254	200.600		0.11786	%
		5	3.562	501.016		0.01067	%
		6	4.101	664.052		0.39804	%
		7	6.443	1640		1.07606	%
		8	7.957	2500		0.06355	%
		9	8.965	3170		2.13823	%
		10	9.200	3340		1.77228	%
	2.66	1	0.275	2.986		0.00000	%
z=		2	0.938	34.718		0.00000	%
	-35.34	3	1.045	43.129		0.01435	%
		4	2.254	200.518		0.13780	%
		5	3.562	501.009		0.01151	%
		6	4.099	663.315		0.45341	%
		7	6.436	1640		1.18921	%
		8	7.957	2500		0.06870	%
		9	8.941	3160		2.40293	%
		10	9.195	3340		1.83058	%
(10% length largest to smallest chord)							
	3.325	1	0.275	2.986		0.00000	%
z=		2	0.938	34.716		0.00000	%
	-34.675	3	1.045	43.127		0.01626	%
		4	2.253	200.461		0.15243	%
		5	3.562	501.007		0.01179	%
		6	4.098	662.886		0.48571	%
		7	6.433	1630		1.24417	%
		8	7.957	2500		0.07008	%
		9	8.929	3150		2.53588	%
		10	9.188	3330		1.90553	%
(20% length largest to smallest chord)							
	6.65	1	0.275	2.986		0.00000	%
z=		2	0.938	34.708		0.00000	%
	-31.35	3	1.045	43.118		0.02679	%
		4	2.252	200.268		0.20028	%
		5	3.562	500.995		0.01291	%
		6	4.095	662.109		0.54399	%
		7	6.426	1630		1.33982	%
		8	7.956	2500		0.07397	%
		9	8.864	3100		3.24975	%
		10	9.097	3270		2.87441	%

Shear Web/Spar Cap Seam - Near Blade Tip					
Length of Seam	Mode	Eigenfreq	Eigenval		
Baseline					
0	1	0.276	3.018		0.00000
z=	2	0.941	34.921		0.00000
-36.75	3	1.049	43.445		0.00000
	4	2.269	203.328		0.00000
	5	3.567	502.403		0.00000
	6	4.140	676.626		0.00000
	7	6.549	1690		0.00000
	8	7.972	2510		0.00000
	9	9.173	3320		0.00000
	10	9.415	3500		0.00000
(1-inch)					
					Difference from Baseline %
0.0254	1	0.276	3.018		0.00000 %
z=	2	0.941	34.922		0.00000 %
-36.7246	3	1.049	43.446		-0.00095 %
	4	2.269	203.324		0.00088 %
	5	3.567	502.406		0.00000 %
	6	4.140	676.629		-0.00024 %
	7	6.549	1690		-0.00031 %
	8	7.972	2510		0.00013 %
	9	9.173	3320		-0.00044 %
	10	9.415	3500		0.00127 %
0.665	1	0.276	3.018		0.00000 %
z=	2	0.941	34.921		0.00000 %
-36.085	3	1.049	43.446		0.00000 %
	4	2.269	203.307		0.00529 %
	5	3.567	502.405		0.00000 %
	6	4.139	676.459		0.01232 %
	7	6.547	1690		0.02535 %
	8	7.972	2510		0.00125 %
	9	9.172	3320		0.00545 %
	10	9.411	3500		0.04493 %
1.33	1	0.276	3.018		0.00000 %
z=	2	0.941	34.921		0.00000 %
-35.42	3	1.049	43.445		0.00095 %
	4	2.269	203.274		0.01322 %
	5	3.567	502.402		0.00028 %
	6	4.139	676.187		0.03237 %
	7	6.545	1690		0.05788 %
	8	7.972	2510		0.00276 %
	9	9.172	3320		0.01308 %
	10	9.407	3490		0.08592 %

	1.995	1	0.276	3.018		0.00000	%
z=		2	0.940	34.920		0.10627	%
	-34.755	3	1.049	43.443		0.00286	%
		4	2.269	203.224		0.02556	%
		5	3.567	502.399		0.00056	%
		6	4.138	675.854		0.05701	%
		7	6.543	1690		0.08658	%
		8	7.972	2510		0.00389	%
		9	9.171	3320		0.02028	%
		10	9.406	3490		0.10557	%
	2.66	1	0.276	3.018		0.00000	%
z=		2	0.940	34.918		0.10627	%
	-34.09	3	1.049	43.441		0.00477	%
		4	2.269	203.160		0.04142	%
		5	3.567	502.396		0.00084	%
		6	4.137	675.522		0.08164	%
		7	6.542	1690		0.10476	%
		8	7.972	2510		0.00439	%
		9	9.170	3320		0.02813	%
		10	9.405	3490		0.11003	%
(10% length largest to smallest chord)							
	3.325	1	0.276	3.018		0.00000	%
z=		2	0.940	34.915		0.10627	%
	-33.425	3	1.049	43.438		0.00953	%
		4	2.268	203.066		0.06433	%
		5	3.567	502.391		0.00140	%
		6	4.135	675.136		0.11015	%
		7	6.541	1690		0.11819	%
		8	7.972	2510		0.00464	%
		9	9.169	3320		0.03903	%
		10	9.404	3490		0.11704	%
(20% length largest to smallest chord)							
	6.65	1	0.276	3.017		0.00000	%
z=		2	0.940	34.899		0.10627	%
	-30.1	3	1.049	43.418		0.03146	%
		4	2.267	202.871		0.11236	%
		5	3.567	502.383		0.00224	%
		6	4.133	674.493		0.15773	%
		7	6.523	1680		0.38436	%
		8	7.972	2510		0.00615	%
		9	9.159	3310		0.15426	%
		10	9.359	3460		0.59647	%

Trailing Edge - Mid-Blade (Between Largest Chord and Tip)					
Length of Seam	Mode	Eigenfreq	Eigenval		
Baseline					
0	1	0.275	2.986		0.00000
z=	2	0.938	34.727		0.00000
-21.375	3	1.045	43.141		0.00000
	4	2.257	201.073		0.00000
	5	3.563	501.123		0.00000
	6	4.118	669.373		0.00000
	7	6.514	1670		0.00000
	8	7.962	2500		0.00000
	9	9.161	3310		0.00000
	10	9.366	3460		0.00000
(1-inch)					
				Difference from Base %	
0.0254	1	0.275	2.986		0.00000 %
z=	2	0.938	34.723		0.00000 %
-21.375	3	1.045	43.129		0.01435 %
-21.4004	4	2.256	200.920		0.03811 %
	5	3.562	501.009		0.01151 %
	6	4.114	668.111		0.09423 %
	7	6.501	1670		0.18546 %
	8	7.962	2500		0.00615 %
	9	9.125	3290		0.39416 %
	10	9.348	3450		0.20210 %
0.665	1	0.275	2.986		0.00000 %
z=	2	0.938	34.719		0.00000 %
-21.0425	3	1.045	43.136		0.00574 %
-21.7075	4	2.256	200.942		0.03279 %
	5	3.562	500.956		0.01684 %
	6	4.114	668.197		0.08767 %
	7	6.502	1670		0.18070 %
	8	7.961	2500		0.01382 %
	9	9.092	3260		0.76190 %
	10	9.348	3450		0.19271 %
1.33	1	0.275	2.986		0.00000 %
z=	2	0.938	34.717		0.00000 %
-20.71	3	1.045	43.134		0.00765 %
-22.04	4	2.256	200.917		0.03899 %
	5	3.562	500.944		0.01796 %
	6	4.113	667.959		0.10564 %
	7	6.501	1670		0.19482 %
	8	7.961	2500		0.01432 %
	9	9.007	3200		1.68436 %
	10	9.348	3450		0.19388 %

	1.995	1	0.275	2.986		0.00000	%
z=		2	0.938	34.716		0.00000	%
	-20.3775	3	1.045	43.132		0.01052	%
	-22.3725	4	2.256	200.883		0.04741	%
		5	3.562	500.935		0.01881	%
		6	4.112	667.636		0.12968	%
		7	6.499	1670		0.21632	%
		8	7.961	2500		0.01482	%
		9	8.895	3120		2.90886	%
		10	9.348	3450		0.19645	%
	2.66	1	0.275	2.986		0.00000	%
z=		2	0.938	34.714		0.00000	%
	-20.045	3	1.045	43.130		0.01339	%
	-22.705	4	2.256	200.844		0.05672	%
		5	3.562	500.930		0.01937	%
		6	4.111	667.266		0.15737	%
		7	6.498	1670		0.24272	%
		8	7.961	2500		0.01507	%
		9	8.769	3040		4.27810	%
		10	9.348	3450		0.20157	%
(10% length largest to smallest chord)							
	3.325	1	0.275	2.985		0.00000	%
z=		2	0.938	34.712		0.00000	%
	-19.7125	3	1.045	43.128		0.01531	%
	-23.0375	4	2.255	200.802		0.06735	%
		5	3.562	500.924		0.01993	%
		6	4.110	666.886		0.18578	%
		7	6.496	1670		0.27435	%
		8	7.961	2500		0.01532	%
		9	8.642	2950		5.67222	%
		10	9.347	3450		0.21075	%
(20% length largest to smallest chord)							
	6.65	1	0.275	2.985		0.00000	%
z=		2	0.938	34.701		0.00000	%
	-18.05	3	1.045	43.115		0.03061	%
	-24.7	4	2.254	200.578		0.12318	%
		5	3.562	500.890		0.02330	%
		6	4.105	665.139		0.31668	%
		7	6.481	1660		0.49988	%
		8	7.960	2500		0.02625	%
		9	8.080	2580		11.80136	%
		10	9.332	3440		0.36727	%

Shear Web/Spar Cap Seam Mid-Blade (Between Largest Chord and Tip)

Length of Seam	Mode	Eigenfreq	Eigenval			
Baseline						
0	1	0.276	3.018		0.00000	
z=	2	0.941	34.921		0.00000	
-21.375	3	1.049	43.445		0.00000	
	4	2.269	203.328		0.00000	
	5	3.567	502.403		0.00000	
	6	4.140	676.626		0.00000	
	7	6.549	1690		0.00000	
	8	7.972	2510		0.00000	
	9	9.173	3320		0.00000	
	10	9.415	3500		0.00000	
(1-inch)						
					Difference from Base %	
0.0254	1	0.276	3.017		0.00000	%
z=	2	0.940	34.919		0.10627	%
-21.375	3	1.049	43.442		0.00381	%
-21.4004	4	2.269	203.303		0.00617	%
	5	3.567	502.393		0.00112	%
	6	4.140	676.554		0.00531	%
	7	6.548	1690		0.00305	%
	8	7.972	2510		0.00351	%
	9	9.172	3320		0.00632	%
	10	9.415	3500		0.00680	%
0.665	1	0.276	3.018		0.00000	%
z=	2	0.941	34.921		0.00000	%
-21.0425	3	1.049	43.444		0.00191	%
-21.7075	4	2.269	203.311		0.00397	%
	5	3.567	502.403		0.00000	%
	6	4.139	676.441		0.01353	%
	7	6.548	1690		0.00519	%
	8	7.972	2510		0.00025	%
	9	9.172	3320		0.01112	%
	10	9.412	3500		0.03218	%
1.33	1	0.276	3.018		0.00000	%
z=	2	0.940	34.919		0.10627	%
-20.71	3	1.049	43.439		0.00667	%
-22.04	4	2.269	203.241		0.02115	%
	5	3.567	502.401		0.00028	%
	6	4.138	675.866		0.05604	%
	7	6.547	1690		0.02795	%
	8	7.972	2510		0.00125	%
	9	9.168	3320		0.05058	%
	10	9.403	3490		0.13329	%

	1.995	1	0.276	3.018		0.00000	%
z=		2	0.940	34.914		0.10627	%
	-20.3775	3	1.049	43.431		0.01621	%
	-22.3725	4	2.268	203.149		0.04406	%
		5	3.567	502.394		0.00112	%
		6	4.135	675.047		0.11667	%
		7	6.545	1690		0.06047	%
		8	7.972	2510		0.00263	%
		9	9.163	3310		0.11218	%
		10	9.391	3480		0.26244	%
	2.66	1	0.276	3.017		0.00000	%
z=		2	0.940	34.910		0.10627	%
	-20.045	3	1.049	43.423		0.02574	%
	-22.705	4	2.268	203.045		0.06962	%
		5	3.567	502.388		0.00168	%
		6	4.132	674.165		0.18189	%
		7	6.542	1690		0.10063	%
		8	7.972	2510		0.00426	%
		9	9.156	3310		0.18740	%
		10	9.379	3470		0.38373	%
(10% length largest to smallest chord)							
	3.325	1	0.276	3.017		0.00000	%
z=		2	0.940	34.906		0.10627	%
	-19.7125	3	1.049	43.415		0.03527	%
	-23.0375	4	2.267	202.947		0.09386	%
		5	3.567	502.377		0.00280	%
		6	4.130	673.311		0.24517	%
		7	6.539	1690		0.14736	%
		8	7.972	2510		0.00577	%
		9	9.148	3300		0.26720	%
		10	9.370	3470		0.47889	%
(20% length largest to smallest chord)							
	6.65	1	0.276	3.016		0.00000	%
z=		2	0.940	34.884		0.10627	%
	-18.05	3	1.048	43.374		0.08198	%
	-24.7	4	2.264	202.412		0.22561	%
		5	3.567	502.325		0.00785	%
		6	4.119	669.768		0.50798	%
		7	6.511	1670		0.56700	%
		8	7.971	2510		0.01179	%
		9	9.119	3280		0.58771	%
		10	9.352	3450		0.67368	%

Trailing Edge - at Widest Chord				
Length of Seam	Mode	Eigenfreq	Eigenval	
Baseline				
0	1	0.275	2.986	0.00000
z=	2	0.938	34.727	0.00000
-4.75	3	1.045	43.141	0.00000
	4	2.257	201.073	0.00000
	5	3.563	501.123	0.00000
	6	4.118	669.373	0.00000
	7	6.514	1670	0.00000
	8	7.962	2500	0.00000
	9	9.161	3310	0.00000
	10	9.366	3460	0.00000
(1-inch) Difference from Base %				
0.0254	1	0.275	2.986	0.00000 %
z=	2	0.938	34.727	0.00000 %
-4.7754	3	1.045	43.141	0.00000 %
	4	2.257	201.074	-0.00044 %
	5	3.563	501.125	0.00000 %
	6	4.118	669.376	-0.00024 %
	7	6.514	1670	-0.00031 %
	8	7.962	2500	-0.00013 %
	9	9.161	3310	0.00000 %
	10	9.366	3460	-0.00021 %
0.665	1	0.275	2.986	0.00000 %
z=	2	0.938	34.725	0.00000 %
-5.415	3	1.045	43.140	0.00096 %
	4	2.257	201.070	0.00089 %
	5	3.563	501.079	0.00449 %
	6	4.118	669.344	0.00194 %
	7	6.513	1670	0.00537 %
	8	7.962	2500	0.00414 %
	9	9.160	3310	0.01288 %
	10	9.366	3460	0.00907 %
1.33	1	0.275	2.986	0.00000 %
z=	2	0.938	34.725	0.00000 %
-6.08	3	1.045	43.138	0.00287 %
	4	2.257	201.057	0.00399 %
	5	3.563	501.038	0.00842 %
	6	4.117	669.171	0.01481 %
	7	6.511	1670	0.03593 %
	8	7.961	2500	0.00879 %
	9	9.154	3310	0.07750 %
	10	9.362	3460	0.05242 %

Shear Web/Spar Cap Seam - at Widest Chord					
Length of Seam	Mode	Eigenfreq	Eigenval		
Baseline					
0	1	0.276	3.018		0.00000
z=	2	0.941	34.921		0.00000
-4.75	3	1.049	43.445		0.00000
	4	2.269	203.328		0.00000
	5	3.567	502.403		0.00000
	6	4.140	676.626		0.00000
	7	6.549	1690		0.00000
	8	7.972	2510		0.00000
	9	9.173	3320		0.00000
	10	9.415	3500		0.00000
(1-inch)					
				Difference from Base %	
0.0254	1	0.276	3.018		0.00000 %
z=	2	0.941	34.921		0.00000 %
-4.7754	3	1.049	43.445		0.00000 %
	4	2.269	203.311		0.00441 %
	5	3.567	502.404		0.00000 %
	6	4.140	676.567		0.00435 %
	7	6.548	1690		0.00611 %
	8	7.972	2510		0.00013 %
	9	9.173	3320		-0.00022 %
	10	9.415	3500		0.00924 %
0.665	1	0.276	3.012		0.00000 %
z=	2	0.939	34.837		0.21254 %
-5.415	3	1.049	43.401		0.05148 %
	4	2.266	202.629		0.17229 %
	5	3.567	502.251		0.01542 %
	6	4.134	674.684		0.14348 %
	7	6.538	1690		0.16034 %
	8	7.971	2510		0.01417 %
	9	9.171	3320		0.01941 %
	10	9.398	3490		0.18958 %
1.33	1	0.276	3.006		0.00000 %
z=	2	0.938	34.728		0.31881 %
-6.08	3	1.048	43.355		0.10486 %
	4	2.261	201.729		0.39393 %
	5	3.566	501.993		0.04093 %
	6	4.126	671.990		0.34300 %
	7	6.523	1680		0.38696 %
	8	7.969	2510		0.03449 %
	9	9.170	3320		0.03630 %
	10	9.375	3470		0.42929 %

